The Dissertation Committee for Punchet Thammarak
certifies that this is the approved version of the following dissertation:

Dynamic Response of Laterally-Loaded Piles

Committee:

John L. Tassoulas, Supervisor

Mark E. Mear

Sharon L. Wood

Lance Manuel

Fulvio Tonon

Dynamic Response of Laterally-Loaded Piles

by

Punchet Thammarak, B.E.

DISSERTATION

Presented to the Faculty of the Graduate School of
The University of Texas at Austin
in Partial Fulfillment
of the Requirements
for the Degree of

DOCTOR OF PHILOSOPHY

THE UNIVERSITY OF TEXAS AT AUSTIN
May 2009

Dedicated to my father and mother.

Acknowledgments

During the time spent on my doctoral research, confrontation with types of problems had become part of my daily routines. It was a very demanding journey, and without the supports, advices, encouragements, and assistance from the surrounding people, it would have been much more difficult for me to achieve my goal. Therefore, I am very pleased to take this opportunity to acknowledge the following people for their continuous helps that fulfilled and made possible this dissertation.

First, I would like to thank Dr. Tassoulas sincerely and gratefully for his knowledgeable advices, patience, and understanding. I am so glad that I had been educated and supervised by him. His dedication to the research, as well as his thoughtful, initiative, and intuitive guidance is greatly appreciated. I am also pleased to thank Dr. Guddati specially for helps and suggestions on the implementation of Continued-Fraction Absorbing Boundary Conditions.

I would like to further my gratitude toward the dissertation committees for all of the dissertation writing suggestions and editorial works.

I wish to specially thank my colleagues who always give me the hands and shared the good time in the Ph.D. student office.

Finally, I would like to thank my father and my mother as the first teachers in my life. Their encouragement and my girlfriend are the most important moral support that has brought me to this level of success.

Dynamic Response of Laterally-Loaded Piles

Publication No. __________________

Punchet Thammarak, Ph.D.
The University of Texas at Austin, 2009

Supervisor: John L. Tassoulas

The laterally-loaded pile has long been a topic of research interest. Several models of the soil surrounding a pile have been developed for simulation of lateral pile behavior, ranging from simple spring and dashpot models to sophisticated three-dimensional finite-element models. However, results from the available pile-soil models are not accurate due to inherent approximations or constraints. For the springs and dashpots representation, the real and imaginary stiffness are calculated by idealizing the soil domain as a series of plane-strain slices leading to unrealistic pile behavior at low frequencies while the three-dimensional finite-element analysis is very computationally demanding.

Therefore, this dissertation research seeks to contribute toward procedures that are computationally cost-effective while accuracy of the computed response is maintained identical or close to that of the three-dimensional finite-element solution. Based on the fact that purely-elastic soil displacement variations in azimuthal direction are known, the surrounding soil can be formulated in terms of an equivalent one-dimensional model leading to a significant reduction of computational cost. The pile with conventional soil-slice model will be explored first. Next, models with shear stresses between soil slices, including and neglecting the soil vertical displacement, are investigated. Excellent agreement of results from the proposed models with three-dimensional finite-element solutions can be achieved with only small additional computational cost.

Table of Contents

List of Tables

List of Figures

Chapter 1

Introduction

Piles have long been used as foundations of structures subjected primarily to axial loads. However, in many situations, horizontal forces and moments from the superstructures also contribute to the pile behavior, requiring horizontal resistance from the surrounding soil to equilibrate the pile-soil system. In the majority of cases, especially, structures exposed to machine vibrations, seismic wave motion, sea waves, and currents, pile foundations must play a significant role in resisting lateral loads. Since the consequences of failure can be catastrophic, it is imperative that the response of piles to lateral loads be understood and appropriate analytical capabilities be developed.

1.1 Early Studies of Lateral Pile Behavior

The simplest analysis approach toward lateral pile behavior was first suggested by Hetenyi (1946). The static solution for a Winkler beam on elastic foundation in Figure 1.1 was employed to model laterally loaded piles. A closed-form solution of the governing differential equation of the beam was obtained with lateral elastic spring resistance as a function of pile lateral displacement. The solution is useful but requires information about the elastic

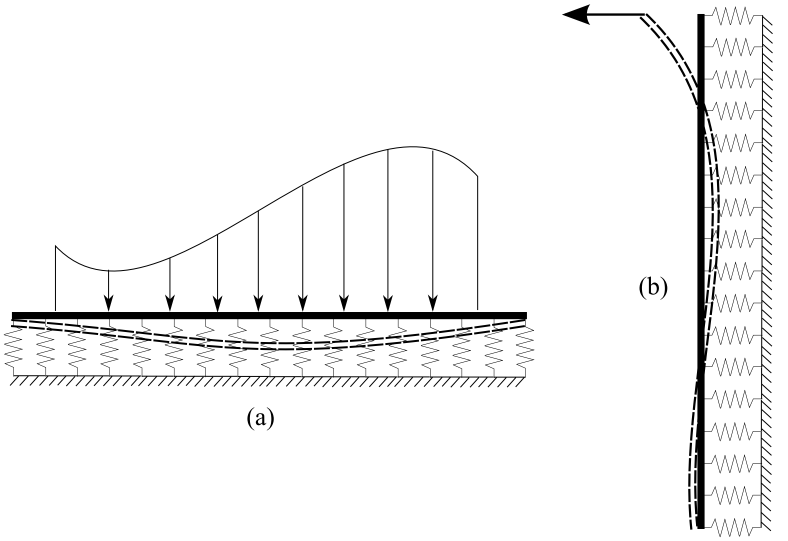

Figure 1.1: (a)Winkler beam on elastic spring foundation; (b) Laterally loaded pile model

foundation stiffness that may not be readily available. Nevertheless, a standard framework for analysis of laterally loaded piles was established on the basis of the Winkler model and remains in wide use.

In the 1950's, the construction of platforms for offshore gas exploration and production triggered extensive investigations of lateral pile behavior, especially, with respect to lateral pile capacity, since the offshore structures are always subjected to significant levels of lateral forces due to currents, waves, and wind that may lead to foundation failure. Thus, the research during this period of time was concentrated on outlining design provisions for laterally loaded piles.

1.1.1 Experimental Studies of Lateral Pile Response

Accurate estimation of lateral pile capacity was initially developed on the basis of the bending-moment distribution along the pile by Matlock & Ripperger (1956,1958). The data from full-scale tests of instrumented piles along with laboratory model tests were recorded and converted by Matlock (1970) to equivalent relationships between distributed lateral load (p) and soil displacement (y). These so-called $p-y$ relationships incorporated the effects of nonlinear clayey soil behavior and even the influence of soil confining pressure. The degradation in soil resistance due to cyclic loading was also brought into the mathematical representation. A systematic method to construct $p-y$ response was suggested and employed with the beam on a nonlinear-spring foundation model to determine the lateral pile capacity under both static and cyclic loads. This representation later appeared in "The recommended practice of planning, designing and constructing fixed offshore platforms" by the American Petroleum Institute. At this time, the nonlinear Winkler model with the p-y relationships was in wide use in estimating lateral pile capacity.

Reese et al. (1974) suggested procedures for constructing p-y relationships for cohesionless soil. The linear elastic portion or initial slope of the p-y curve can be determined from the value suggested for a particular type of soil. Nonlinearity was taken into account properly and soil degradation due to cyclic loading was also included in the mathematical representation.

1.1.2 Continuum-based Study of Lateral Pile Response

The earliest continuum-based effort involving laterally-loaded pile behavior was by Douglas and Davis (1964). This particular study focused on the lateral response of rigid foundations, rotated by the effects of a horizontal force and a moment. Their procedure assumes that the foundation is a thin strip subjected to a rigid-body rotation. Next, a thin plate is discretized by grid lines and the relationship between a unit point force (representing a uniformly distributed pressure over a discretized area) and the displacement at the center of each discretized area is estimated by Mindlin's solution (1936). As a result, if the displacement of the foundation is known, the stress distribution along the depth can be determined leading to a horizontal force or a moment corresponding to a given displacement.

Later, Poulos (1971) extended the procedure by Douglas and Davis (1964), limited to an undeformable foundation, to laterally-loaded deformable piles. The pile was idealized as a thin strip, deforming under Euler beam theory, and discretized solely along the length. The relationship between soil displacement at each nodal point and a point force was established in the same manner as in Douglas and Davis (1964). Next, this piecewise solution for a rectangle was combined with the equation of flexure and applied by means of finite differences. The influence factors, varied with pile-soil relative stiffness ratio so-called "the pile flexibility factor", were presented for the calculation of pile-head displacement and rotation. The pile-head stiffness obtained by this approach was found to be in agreement with the prediction based on the linear Winkler model based on the so-called subgrade reaction theory with spring coefficients determined from an expression in terms of a constant factor, the soil elastic modulus, and the pile diameter.

1.2 Study of Dynamic Behavior of Laterally Loaded Single Piles

Dating back to the period of thriving research on dynamic soil-structure interaction in the 1970's and 1980's, significant attention had been focused on the behavior of the machine foundations. The researchers' interest was then extended to the dynamics of laterally loaded piles.

1.2.1 Continuum Approach

In the 1960's, a powerful idea was introduced in order to simplify lateral pile analysis by idealizing a three dimensional soil domain as a stack of independent infinitesimal thin soil slices. Each particular soil slice behaves under plane-strain conditions and the soil material is assumed homogenous, isotropic, and viscoelastic. The expression of soil resistance on a thin portion of the pile (idealized as a rigid massless disk) due to in-plane, horizontal, harmonic motion was first derived by Baranov (1967). Novak, Nogami, and Aboul-Ella (1978), extended the solution to rocking and vertical (out-of-plane) motion. Hysteretic damping was included in this solution to take care of the effect of soil inelasticity. In view of the lack of interaction between soil slices, the stiffness of the disk can be represented as a discrete spring over a small

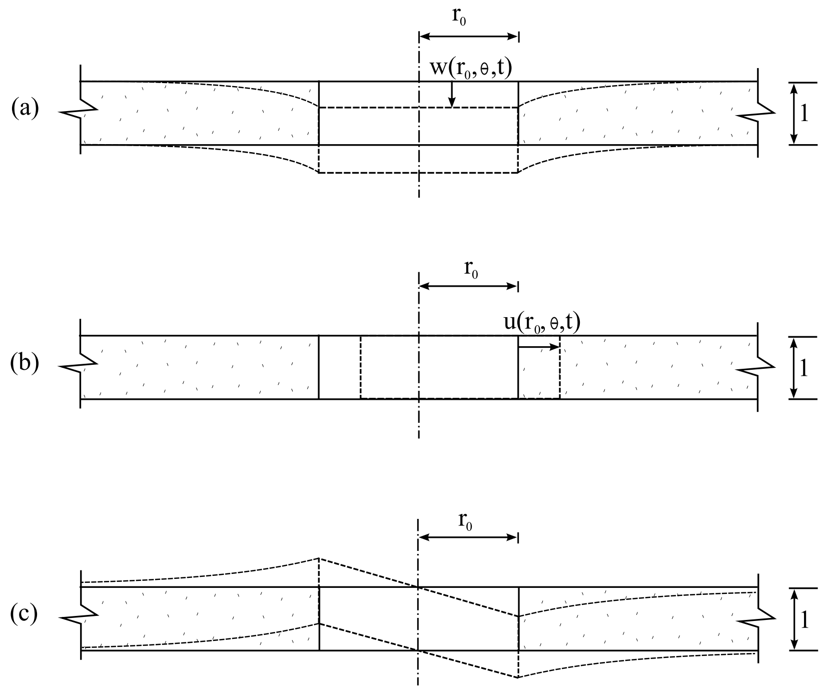

Figure 1.2: Rigid disk embedded in infinite plane domain under (a) Vertical ; (b) Horizontal; (c) Rotational excitation (Novak et al. 1978)

portion of pile. Thus, the soil-pile system can be represented by the Winkler beam model.

Working as outlined above, Beredugo & Novak (1972) obtained an approximate solution for coupled horizontal and rocking vibrations of rigid, cylindrical embedded footings. The soil resistance on the small slice of the pile can be determined by Baranov's solution. This approach was verified to work considerably well for vertically and torsionally excited rigid embedded cylindrical foundations Beredugo (1971) and Novak & Sachs (1973). The relationship between the horizontal force and the displacement and rotation at the pile head was established and compared with experimental results. However, the approximate numerical solution did not produce a sufficiently accurate prediction of the peak displacement in the response spectrum. The dissimilarity in shape of the displacement response spectra was also significant.

The idea of independent soil slices was first implemented for laterally loaded piles by Novak (1974). The pile was idealized as a Winkler beam on a foundation composed of distributed independent-discrete elastic springs and viscous dashpots as illustrated in Figure 1.3. The spring and dashpot coefficient per unit thickness of slice can be computed as discussed above. The closed-form complex dynamic stiffness at the pile head was established for single piles, single pile with pile cap embedded in the ground, and two-pile group foundations on the basis of the beam governing partial differential equation. The approximate pile head stiffness based on soil slice and the complex stiffness from a rigorous elastic solution are comparable at high dimensionless frequencies ($a_0 = \omega \cdot r_0/c_s$ where ω is the angular frequency: r_0 is the radius of the pile: c_s is the shear-wave velocity). However, at low dimensionless frequencies, the lateral pile stiffness, determined under the plane-strain soil-slice assumption, vanishes as the dimensionless frequency approaches zero. This unrealistic result is a consequence of neglecting the shear interaction between soil slices.

Regarding the issue above, Novak and Grigg (1976) performed a field experiment on single piles in a homogeneous soil layer with underlying bed rock. The piles were excited through a range of frequencies of interest and the displacement-excitation frequency relationship was obtained. The theo-

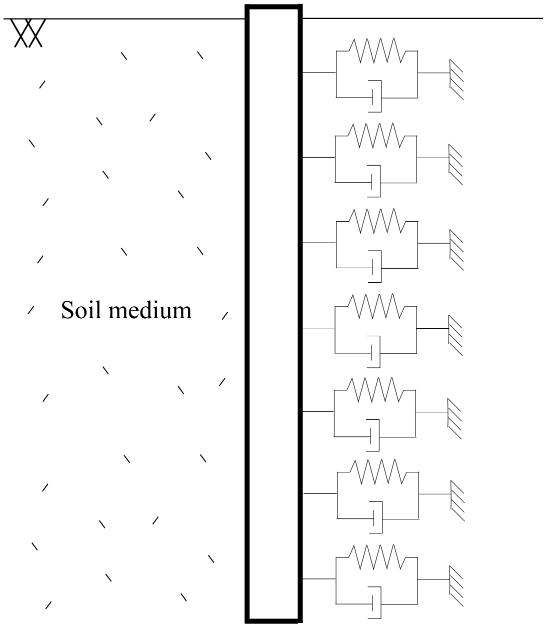

Figure 1.3: Winkler beam on spring and dashpot foundation for laterally loaded dynamic pile

retical response spectrum, determined by the above approach, was compared to that from experiments and, again, the mismatch of the lowest fundamental frequency persisted. The resolution of the discrepancy, as suggested by Novak and Grigg (1976), is to use the soil shear modulus that is back-calculated from static pile response by manipulating the theoretical static solution by Poulos (1971). The resulting shear modulus will be smaller than that obtained from wave propagation experiments because of the lack of confining pressure at the surface, soil-pile separation, and gapping. The displacement spectrum predicted by this adjustment leads to the accurate frequency corresponding to the peak displacement. However, accurate shape and peak amplitude are not always obtained.

Nogami and Novak (1977) developed an estimate of pile-head stiffness based on the theory of elasticity. The circular cross-section pile and surrounding soil were modeled in a cylindrical coordinate system. The vertical motion of the soil (z-direction) was assumed to be insignificant and neglected in the formulation, resulting in zero shear stresses in the z direction (τ_{rz} and $\tau_{\theta z}$). The soil domain is homogeneous with traction-free soil surface and base fixed as described in Figure 1.4. Both pile and soil are linear elastic. Hysteretic frequency independent damping is included in the formulation to represent (to some extent) dissipation due to soil inelasticity. In cases of slender piles, the stiffness obtained in this manner compares reasonably well with fully three-dimensional finite element analysis. However, for stubby short piles, it was found later in this research that the vertical motion of the soil should be properly taken into account.

Roesset et al. (1982) have suggested an approximate procedure for estimation of the real and imaginary coefficients of the horizontal spring. The parametric study of three-dimensional finite-element models of a laterally-loaded pile was conducted and compared with a Winkler beam on spring-and-dashpot foundation, hence, all coefficients in the expression for spring and dashpot can be obtained. The subgrade reaction theory was employed to represent spring coefficient, in terms of a constant factor and the soil Young's modulus, and the dashpot coefficient was expressed by Biggs-Roesset equation. However, this stiffness estimation does not take into account the soil Poisson's

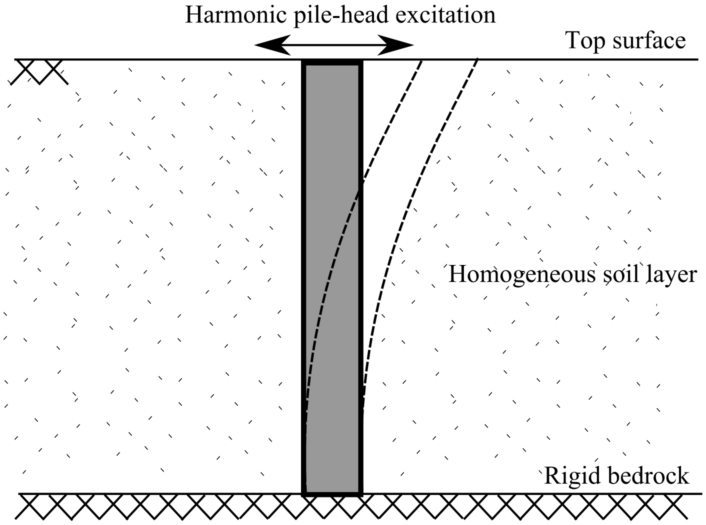

Figure 1.4: Theoretical pile model embedded in isotropic homogeneous soil medium

ratio, in contrast with the closed-form solution by Novak et al. (1978). It is limited to harmonic vibrations and the accuracy of pile response may be reduced because of simplification of complex stiffness vs. frequency relationship.

A treatment of the lack of pile stiffness at low frequencies was presented by Novak and Sheta (1982). The observation had been made from the result in Novak (1974) that the real stiffness, S_{u1}, of the disk is more or less constant below the dimensionless frequency ($a_0 = \omega \cdot r_0/c_s$ where ω is excitation frequency: r_0 is the pile radius: c_s is the shear-wave velocity) of 0.3. Thus, over the range of a_0 = 0.0 - 0.3, the real part of stiffness was taken as the value corresponding to $a_0 = 0.3$. A similar modification was made in the imaginary stiffness, S_{u2}, by setting the value below the layer resonance frequency, $f_H = \frac{c_s}{4H}$, equal to $S_{u1} \cdot D$ where D is the material damping, c_s is shear wave velocity of the soil, and H is the layer thickness.

Novak and Sheta (1980) attempted to include the effects of soil nonlinearity and slippage at the pile-soil interface. The direct approach to model such phenomena is very costly with respect to computation effort because of the three-dimensional finite element analysis that appears to be required. Novak and Sheta (1980) retained the simplicity of analysis by proposing a treatment with a Winkler beam on elastic foundation. The methodology, first proposed by Baguelin et al. (1977), is to separate the soil domain into two regions, inner and outer zones as shown in Figure 1.5. The outer zone contains the soil properties from site investigation while the shear modulus and material damping ratio in the inner zone is set to account for soil nonlinearity and slippage. However, there is no systematic framework of the soil properties in the inner zone. The inner region is the ring of soil with inner radius equal to the disk radius and outer radius consistent with the extent of soil nonlinearity. The equation of motion of the horizontally moving rigid massless disk was written and the zero displacement boundary condition was enforced at the outer radius. The spring and dashpot stiffness for two zones were combined to represent the new reduced disk stiffness.

Nogami & Chen (1987) and Nogami et al. (1992) developed a composite-soil medium idealization initialized by Novak & Sheta (1980). The stiffness of the outer region was left unchanged and attention was focused on a technique for introducing the influence of inelastic behavior of soil on lateral pile behavior. Additionally, the inner region was modified in order to account for soil-pile

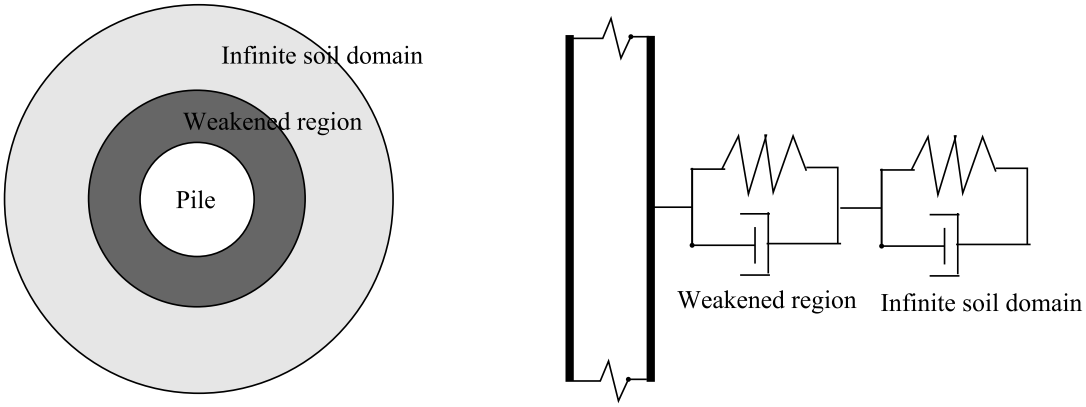

Figure 1.5: Soil weakened region around the pile circumference

gap opening. The parameters that describe the mathematical model for the inner zone can be obtained from the force-displacement relationship recorded during a cyclic pile test. Once the hysteretic loop is constructed, the real stiffness of the disk can be approximated by dividing the maximum force by the maximum displacement. The imaginary stiffness can be back-calculated from the relationship between the dissipated energy, the area enclosed by hysteretic loop, and the pile displacement. Gap formation can be triggered when the soil dynamic tension on the pile surface exceeds the soil horizontal confining pressure computed by the coefficient of lateral earth pressure, K_0.

The idea that the soil around the pile is weakened by the installation process and imperfect bond at soil-pile interface was described in Novak & Sheta (1980) and Dotson & Veletsos (1990). The soil shear modulus in the weak boundary zone is reduced and material damping increases. The soil in the weakened zone gradually becomes less weak as the depth increases with increasing confining pressure and decreasing slippage at the soil-pile interface.

However, the specific procedure for the calculation of weakened zone properties was not suggested.

In 1992, an experimental study of a laterally loaded concrete pile was carried out by El-Marsafawi et al. (1992) to validate the existing theoretical pile model. The pile was subjected to horizontal, harmonic excitation through a frequency range of interest. The dimensionless displacement versus excitation frequency plot was then available for comparison. The theoretical model employed the Winkler beam model on spring and dashpot foundation. Spring and dashpot coefficients were determined under the plane-strain assumption (independent soil slices) and the soil slice medium was considered composite. The weak soil properties in the inner region were used to calculate the inner zone complex stiffness following the expression in Novak & Sheta (1980). The treatment of the lack of stiffness at low frequencies, explained in Novak & Sheta (1982), was implemented in this study. The theoretical displacement response with the frequency matched favorably with experimental work.

An improvement in the treatment of inelastic behavior was proposed in El-Naggar & Novak (1995). The modified shear modulus of the inner zone was calculated using the mobilization ratio, η, introducing the nonlinearity in the soil slice model as depicted in Figure 1.6. The mobilization ratio, η, is the ratio of current spring force to the ultimate spring resistance, computed from expressions suggested in Matlock (1970) for cohesive soil and Reese et al. (1974) for cohesionless soil. The more sophisticated approach by El Naggar and Bentley (2000) was later presented to improve the behavior of the model

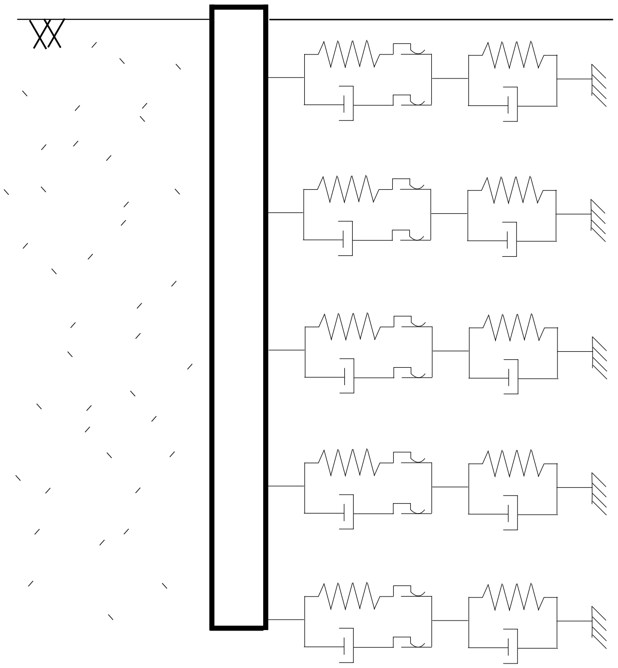

Figure 1.6: Laterally loaded pile model with nonlinear springs and dashpots for the inner region

of El-Naggar & Novak (1995).

In summary, there remain two important issues that impede accurate estimation of lateral pile response. The shear interaction between soil slices that was originally neglected actually plays a key role in low-frequency behavior (computation of first resonance frequency and the peak displacement amplitude). Additionally, the effect of pile-head condition is not included in the treatment suggested in Novak and Sheta (1982). Also, frequency dependence can be problematic, if the model is to be used in transient analysis.

1.2.2 Backbone-curve-based Study of Lateral Pile Response

This approach toward analysis of lateral pile behavior also employs the Winkler beam on spring and dashpot foundation for computational simplicity. There are several different approaches toward determination of the complex $p-y$ springs and dashpots.

Kagawa and Kraft (1980 a,b & 1981) suggested that the $p-y$ spring stiffness can be written in terms of Young's modulus of soil and a dimensionless coefficient, δ. Such a coefficient is assumed to be constant along the pile and can be determined by equating the work done in the exact system with that from the Winkler pile on spring foundation. The range of δ is from 1 to 4 depending on material properties and pile configuration parameters, e.g. loading condition (pile head or seismic excitation), pile-head fixity, and pile flexibility factor. An effort to introduce soil hysteresis was made by a simple expression. The radiation damping was easily approximated by assuming that the longitudinal and shear waves radiate through strips the width of which is equal to the pile diameter (Figure 1.7 (a)). There are four soil strips, two in the direction of pile movement and the others in the orthogonal direction.

Gazetas and Dobry (1984) presented a systematic framework for the construction of a dynamic $p-y$ relationship. First, methodologies for determination of the real stiffness from various studies, including a weighted-average method by Kagawa and Kraft (1980) (equating the work done along the pile from 3-dimensional finite-element analysis to the work in the pile and system of horizontal springs in order to determine the spring coefficient in terms of

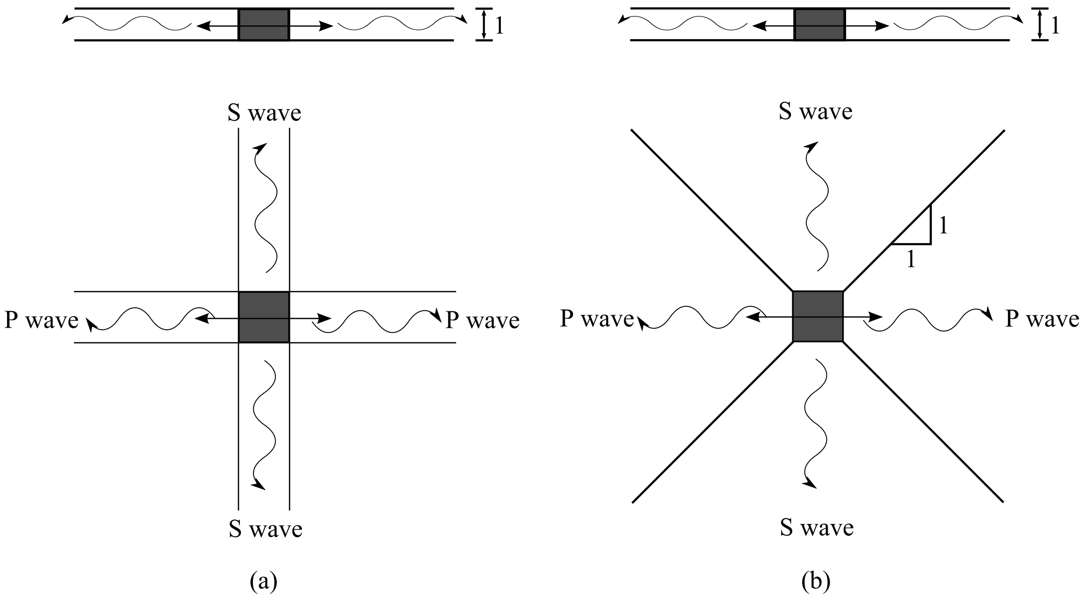

Figure 1.7: Simplified plane model for radiation damping (a) Kagawa & Kraft; (b) Gazetas & Dobry

a constant factor and E_s), three-dimensional finite element calculations by Nogami & Novak (1977) and Kuhlemeyer (1979), were summarized and the initial spring stiffness was written as $\delta \cdot E_s$. where E_s is Young's modulus of the soil and δ ranges from 1.0 - 1.2 for a fixed-head condition and from 1.5 - 2.5 for free-head condition. The recommended spring stiffness can be combined with the Winkler beam model and the pile head static stiffness can be determined. Next, the ratio of pile head stiffness to that of the static case, K/K_s, is available in a plot versus dimensionless frequency.

The radiation damping of the soil slice was examined in Gazetas & Dobry (1984). The soil slice is separated into four quarters and there is no interaction between quarters (Figure 1.7 (b)). Two quarters in the direction of pile movement will take care of longitudinal wave propagation. The remaining quarters radiate the energy from shear wave. The overall dashpot at the pile head can be determined by integrating the damping coefficient times the square of normalized static deflection profile of pile. A slight modification was made at low frequencies (lower than the layer resonance frequency) by introducing hysteretic damping.

The Bouc-Wen nonlinear backbone curve was first used in pile analysis by Trochanis et al (1991). This model is capable of describing soil nonlinearity, soil-pile separation, and interface slippage. A systematic process for constructing the backbone curve was established by Badoni and Makris (1996). The hysteretic dimensionless quantity, ζ, was taken as a variable that describes the spring nonlinearity. The initial spring stiffness was selected to be $1.2E_s$ as suggested in Makris & Gazetas (1992). The yielding soil resistance (p_u) and displacement (y_0) were calculated following the approach in Matlock (1970) for cohesive and Reese et al. (1974) for cohesionless soil. The nonlinearity of the elastic portion and the smoothness of transition at yielding can be controlled by tuning parameters to match the static load-displacement response. The damping coefficient was given by Wolf et al (1992) by manipulating the cone model embedded in half space. This approximation of the dashpot agrees with the imaginary stiffness derived by Novak et al. (1978).

Further development of the nonlinear mathematical model of the soil spring Bodani & Makris (1996) was furnished by Gazetas and Gerolymos (2007). The effect of nonlinearity was modelled more realistically by including

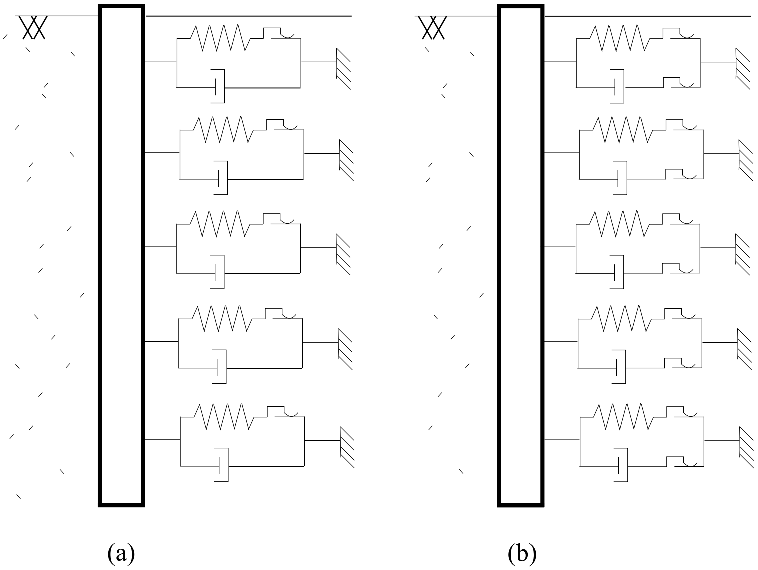

Figure 1.8: Dynamic-nonlinear laterally loaded pile model (a) Badoni & Makris; (b) Gazetas & Gerolymos

the hysteretic dimensionless quantity in both spring and dashpot coefficients. The pinching factor was introduced to the spring stiffness to model gap formation.

In conclusion, the Bouc-Wen type spring model has undergone significant improvement to capture all types of nonlinearities. To date, the nonlinearity is taken into account in springs as well as dashpots but the stiffness coefficients are no longer frequency-dependent as presented in Gazetas and Dobry (1984) in order to simplify the nonlinear expressions. As a result, some dynamic characteristics of the pile-soil system, e.g. resonant frequency, may not be simulated accurately.

1.3 Research contribution

The dynamic analysis of a laterally-loaded pile by means of a Winkler beam on springs and dashpots representing the surrounding soil entails dramatic savings in computational effort. However, although the three-dimensional soil-pile system is treated more efficiently by the one-dimensional Winkler model, the accuracy of the analysis is compromised. In general, spring-and-dashpot models are frequency-dependent. Thus, in transient analysis, the best approach in selecting appropriate spring and dashpot coefficients is on the basis of the dominant frequency of the excitation of interest.

With regard to inelastic material behavior, the Bouc-Wen hysteresis model (Trochanis 1991, Makris & Badoni 1996, and Gazetas & Gerolymos 2007) can be used. However, the coefficients describing such a nonlinear force-displacement relationship must be back-calculated from static lateral load tests.

Since radiation damping and material inelasticity are the two major mechanisms of energy dissipation in the pile-soil system, their interplay greatly affects the accuracy of solutions. Recently, nonlinear dashpots were presented by Gazetas & Gerolymos (2007) to account for the coupling between the two mechanisms. However, no methodology was described for parameter identification. Apparently, fine-tuning with experimental results may be required.

Accordingly, this dissertation research is aimed at contributing new finite elements for efficient analysis of laterally-loaded piles. Because of the high computational effort involved the basis of a description of the soil as a continuum in three-dimensional finite-element analysis, the new elements are intended as efficient yet accurate alternative modeling tools. As in earlier studies of laterally-loaded piles, the direction of this research is to reduce the dimension of analysis. However, in the interest of maintaining accuracy, two-dimensional finite-element models are considered in addition to one-dimensional such models that resemble Winkler models with springs and dashpots. The two-dimensional models provide wider latitude in terms of accuracy while outerperforming three-dimensional ones with regard to efficiency.

Furthermore, by the continuum description of the soil, the one-dimensional and two-dimensional finite elements to be described in this dissertation can accommodate all available constitutive models. Thus, the interaction between inelasticity and wave propagation (material and radiation damping) will be taken into account appropriately without any need of parameter fine-tuning.

1.4 Dissertation outline

The developments of representations of the soil surrounding laterally-loaded piles are reported in three chapters as follows;

1.4.1 Plane Idealization

As in previous studies based on a series of soil slices as a representation of the three-dimensional soil domain, the development of a simple finite-element model is presented in Chapter 3. A two-dimensional plane-strain FE model of the disk embedded in a homogeneous soil domain extending to infinity is constructed as a reference solution for the validation of new finite-element models. The absorbing boundary conditions are required for the representation of the unbounded soil domain and detailed explanations of the implementation of Continued Fraction Absorbing Boundary Conditions (CFABCs) are included in the chapter. Finally, the result from 2-D finite element model is verified with the exact solution for a vibrating disk.

1.4.2 One-Dimensional Finite Element Model

The development of a simple one-dimensional model for the representation of 2-D soil plane domain is presented in Chapter 3. Model validations for cases of purely-elastic and inelastic material behavior are carried out. A discussion of the performance of soil-slice model is also included.

1.4.3 Ring Element with Shear Interactions between Soil-Slices

Since the independent soil-slice idealization neglects shear stresses between soil slices, the lateral pile stiffness approaches zero at low frequencies, not a realistic result. Therefore, in Chapter 4, the shear stress components are introduced to the soil element, then, numerical models become two-dimensional with two degrees of freedom at each node (2D-2DOF ring element). The vertical soil displacement, assumed to be negligible in lateral pile vibrations, is kept equal to zero.

The assumption that the soil vertical displacement can be neglected is next explored by comparing the analysis results with the complete three-dimensional finite-element analysis. A ring element including the vertical soil displacement, 2D-3DOF ring element, is formulated and the validation is carried out by comparing model results with the other 3-dimensional finite-element solution calculations. Finally, results obtained for piles with two soil models are shown for cases of different pile slenderness ratio in order to assess the magnitude of discrepancies resulting from the assumption of zero vertical soil displacement.

1.4.4 Summary and Conclusions

The summary and conclusion of the study and contribution from each chapter and suggestion for further research will be described in the last chapter.

Chapter 2

Plane-Strain Idealization

During sixty years of studies on lateral pile behavior, the most engaging model has been based on the idea of a beam on a Winkler foundation consisting of springs and dashpots, a simple, yet practical and effective representation of the pile-soil system. The most challenging part of the Winkler model development of the estimation of spring and dashpot characteristics. As shown in Figure 2.1, the three-dimensional continuum soil domain must be divided into a finite number of discrete and independent slices. Interactions between soil slices, for example, due to shear at interfaces, are neglected.

The research described herein was initially focused on the development of characteristics of springs and dashpots on the basis of conventional independent soil slices. Thus, a continuum plane-strain finite-element model of a rigid cylinder surrounded by an infinite soil domain was constructed to produce reference solutions, especially when considering transient dynamics and inelastic behavior, for comparison with the one-dimensional Winkler model to be discussed later. This chapter provides details on the 2-D plane-strain model and summarizes its performance by comparison with available exact solutions for purely-elastic soil slices.

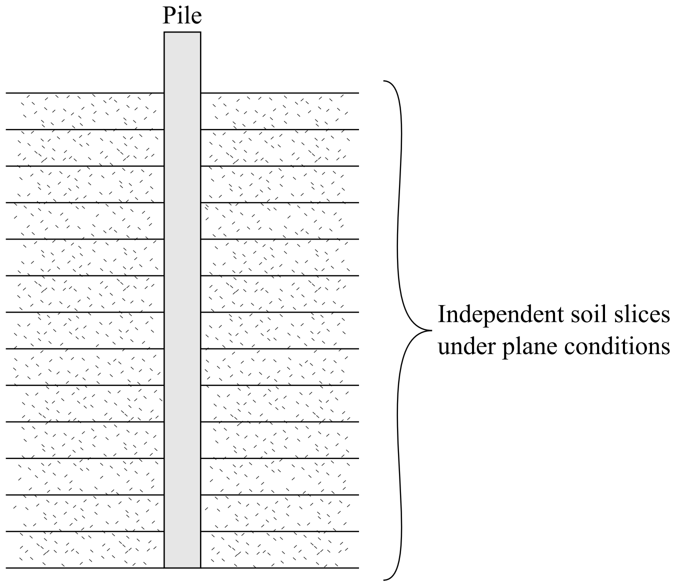

Figure 2.1: Approximation of three dimensional soil domain for laterally loaded pile model

2.1 2-D rigid disk embedded in infinite soil domain model

The two dimensional plane strain finite element model of the rigid disk in the soil slice is constructed using 4-node quadrilateral elements with linear displacement interpolation. Time integration is performed using the Newmark scheme (constant-average acceleration method). The soil inelasticity is represented by a Von Mises plasticity model. All the features contained in the model can be found in standard finite element resources but the implementation of the Continued Fraction Absorbing Boundary Condition (CFABC) for simulation of wave propagation in an unbounded medium presented by Guddati and Lim (2004) will be given next in this chapter.

2.1.1 Formulation of Continued Fraction Absorbing Boundary Conditions

The CFABCs are constructed in the same manner as standard finite elements but, for the purpose of stress-wave absorption, imaginary lengths are introduced in the directions in which the soil domain extends to infinity. As a result, the stress in an absorbing element can be calculated by scaling the element size consistently with the imaginary stretching. Since the stress and strain components are coupled through the conventional rigidity matrix as shown in Equation 2.1, the stretching in one direction will also affect the behavior in the other direction. In the formulation of CFABCs, the constitutive relation for the plane-strain conditions will be rewritten in the equivalent form given by Equation 2.2 in order to disengage the behavior in one direction from the behavior in the other.

$$\begin{bmatrix} \sigma_{xx} \\ \sigma_{yy} \\ \tau_{xy} \end{bmatrix} = \begin{bmatrix} \lambda + 2G & \lambda & 0 \\ \lambda & \lambda + 2G & 0 \\ 0 & 0 & G \end{bmatrix} \begin{bmatrix} \varepsilon_{xx} \\ \varepsilon_{yy} \\ \gamma_{xy} \end{bmatrix} \tag{2.1}$$

(λ: Lame' modulus; G: shear modulus)

$$\begin{bmatrix} \sigma_{xx} \\ \tau_{xy} \\ \tau_{yx} \\ \sigma_{yy} \end{bmatrix} = \underbrace{\begin{bmatrix} \lambda + 2G & 0 & 0 & \lambda \\ 0 & G & G & 0 \\ 0 & G & G & 0 \\ \lambda & 0 & 0 & \lambda + 2G \end{bmatrix}}_{\mathbf{D}^*} \begin{bmatrix} \varepsilon_{xx} \\ \varepsilon_{xy} \\ \varepsilon_{yx} \\ \varepsilon_{yy} \end{bmatrix} \tag{2.2}$$

The strain approximation for a quadrilateral 4-node element can be written as

$$
\begin{aligned}
\underset{\sim}{\varepsilon} &= \begin{bmatrix}
\frac{\partial N_1}{\partial x} & 0 & \frac{\partial N_2}{\partial x} & 0 & \frac{\partial N_3}{\partial x} & 0 & \frac{\partial N_4}{\partial x} & 0 \\
\frac{\partial N_1}{\partial y} & 0 & \frac{\partial N_2}{\partial y} & 0 & \frac{\partial N_3}{\partial y} & 0 & \frac{\partial N_4}{\partial y} & 0 \\
0 & \frac{\partial N_1}{\partial x} & 0 & \frac{\partial N_2}{\partial x} & 0 & \frac{\partial N_3}{\partial x} & 0 & \frac{\partial N_4}{\partial x} \\
0 & \frac{\partial N_1}{\partial y} & 0 & \frac{\partial N_2}{\partial y} & 0 & \frac{\partial N_3}{\partial y} & 0 & \frac{\partial N_4}{\partial y}
\end{bmatrix}
\begin{bmatrix} u_1 \\ v_1 \\ u_2 \\ v_2 \\ u_3 \\ v_3 \\ u_4 \\ v_4 \end{bmatrix} \\
&= \begin{bmatrix}
\sum_{i=1}^{4} \frac{\partial N_i}{\partial x} u_i \\
\sum_{i=1}^{4} \frac{\partial N_i}{\partial y} u_i \\
\sum_{i=1}^{4} \frac{\partial N_i}{\partial x} v_i \\
\sum_{i=1}^{4} \frac{\partial N_i}{\partial y} v_i
\end{bmatrix}
= \begin{bmatrix}
\sum_{i=1}^{4} (\frac{\partial N_i}{\partial r} \frac{\partial r}{\partial x} + \frac{\partial N_i}{\partial s} \frac{\partial s}{\partial x}) u_i \\
\sum_{i=1}^{4} (\frac{\partial N_i}{\partial r} \frac{\partial r}{\partial y} + \frac{\partial N_i}{\partial s} \frac{\partial s}{\partial y}) u_i \\
\sum_{i=1}^{4} (\frac{\partial N_i}{\partial r} \frac{\partial r}{\partial x} + \frac{\partial N_i}{\partial s} \frac{\partial s}{\partial x}) v_i \\
\sum_{i=1}^{4} (\frac{\partial N_i}{\partial r} \frac{\partial r}{\partial y} + \frac{\partial N_i}{\partial s} \frac{\partial s}{\partial y}) v_i
\end{bmatrix}
\end{aligned}
\tag{2.3}
$$

where r and s are the local coordinates for CFABC elements as shown in Figure 2.2; x and y are the global coordinate system of the model; N_i is the linear shape function for node i; u_i and v_i are the displacement along x and y axis;

Next Equation 2.3 can be rewritten as

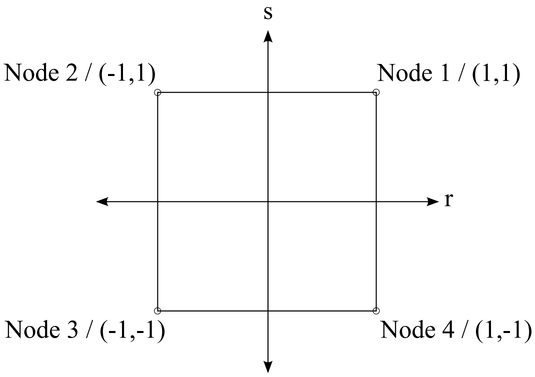

Figure 2.2: Quadrilateral 4-node element

$$\begin{bmatrix} \varepsilon_{11} \\ \varepsilon_{12} \\ \varepsilon_{21} \\ \varepsilon_{22} \end{bmatrix} = \begin{bmatrix} \frac{\partial r}{\partial x} & \frac{\partial s}{\partial x} & 0 & 0 \\ \frac{\partial r}{\partial y} & \frac{\partial s}{\partial y} & 0 & 0 \\ 0 & 0 & \frac{\partial r}{\partial x} & \frac{\partial s}{\partial x} \\ 0 & 0 & \frac{\partial r}{\partial y} & \frac{\partial s}{\partial y} \end{bmatrix} \begin{bmatrix} \sum_{i=1}^{4} \frac{\partial N_i}{\partial r} u_i \\ \sum_{i=1}^{4} \frac{\partial N_i}{\partial s} u_i \\ \sum_{i=1}^{4} \frac{\partial N_i}{\partial r} v_i \\ \sum_{i=1}^{4} \frac{\partial N_i}{\partial s} v_i \end{bmatrix} \tag{2.4}$$

Now, consider the following equations

$$\begin{bmatrix} \frac{\partial N_i}{\partial x} \\ \frac{\partial N_i}{\partial y} \end{bmatrix} = \begin{bmatrix} \frac{\partial r}{\partial x} & \frac{\partial s}{\partial x} \\ \frac{\partial r}{\partial y} & \frac{\partial s}{\partial y} \end{bmatrix} \begin{bmatrix} \frac{\partial N_i}{\partial r} \\ \frac{\partial N_i}{\partial s} \end{bmatrix} \tag{2.5}$$

$$\begin{bmatrix} \frac{\partial N_i}{\partial r} \\ \frac{\partial N_i}{\partial s} \end{bmatrix} = \begin{bmatrix} \frac{\partial x}{\partial r} & \frac{\partial y}{\partial r} \\ \frac{\partial x}{\partial s} & \frac{\partial y}{\partial s} \end{bmatrix} \begin{bmatrix} \frac{\partial N_i}{\partial x} \\ \frac{\partial N_i}{\partial y} \end{bmatrix} \tag{2.6}$$

With the notation:

$$\begin{bmatrix} \dfrac{\partial r}{\partial x} & \dfrac{\partial s}{\partial x} \\ \\ \dfrac{\partial r}{\partial y} & \dfrac{\partial s}{\partial y} \end{bmatrix} = \begin{bmatrix} \dfrac{\partial x}{\partial r} & \dfrac{\partial y}{\partial r} \\ \\ \dfrac{\partial x}{\partial s} & \dfrac{\partial y}{\partial s} \end{bmatrix}^{-1} = \mathbf{J}^{-1} \tag{2.7}$$

Equation 2.4 can be written in the following form:

$$\underset{\sim}{\varepsilon} = \underbrace{\begin{bmatrix} \mathbf{J}^{-1} & \mathbf{0} \\ \mathbf{0} & \mathbf{J}^{-1} \end{bmatrix}}_{\Theta} \underbrace{\begin{bmatrix} \frac{\partial N_1}{\partial r} & 0 & \frac{\partial N_2}{\partial r} & 0 & \frac{\partial N_3}{\partial r} & 0 & \frac{\partial N_4}{\partial r} & 0 \\ \\ \frac{\partial N_r}{\partial s} & 0 & \frac{\partial N_2}{\partial s} & 0 & \frac{\partial N_3}{\partial s} & 0 & \frac{\partial N_4}{\partial s} & 0 \\ \\ 0 & \frac{\partial N_1}{\partial r} & 0 & \frac{\partial N_2}{\partial r} & 0 & \frac{\partial N_3}{\partial r} & 0 & \frac{\partial N_4}{\partial r} \\ \\ 0 & \frac{\partial N_1}{\partial s} & 0 & \frac{\partial N_2}{\partial s} & 0 & \frac{\partial N_3}{\partial s} & 0 & \frac{\partial N_4}{\partial s} \end{bmatrix}}_{\mathbf{B}} \begin{bmatrix} u_1 \\ v_1 \\ u_2 \\ v_2 \\ u_3 \\ v_3 \\ u_4 \\ v_4 \end{bmatrix} \tag{2.8}$$

The vector of internal forces, P, can be expressed as

$$\begin{aligned} P &= \int_{-1}^{1}\int_{-1}^{1} [\Theta\mathbf{B}]^T\,\mathbf{D}^*\,[\Theta\mathbf{B}]\det(\mathbf{J})\,\mathrm{d}r\mathrm{d}s\,\mathbf{U} \\ &= \int_{-1}^{1}\int_{-1}^{1} [\mathbf{B}]^T\,[\Theta]^T\,\mathbf{D}^*\,[\Theta]\,[\mathbf{B}]\det(\mathbf{J})\,\mathrm{d}r\mathrm{d}s\,\mathbf{U} \\ &= \int_{-1}^{1}\int_{-1}^{1} [\mathbf{B}]^T\,\overline{\mathbf{D}}\,[\mathbf{B}]\;\mathrm{d}r\mathrm{d}s\,\mathbf{U} \end{aligned} \tag{2.9}$$

where:

$$\overline{\mathbf{D}} = \begin{bmatrix} \mathbf{J}^{-1} & \mathbf{0} \\ \mathbf{0} & \mathbf{J}^{-1} \end{bmatrix} \mathbf{D}^* \begin{bmatrix} \mathbf{J}^{-1} & \mathbf{0} \\ \mathbf{0} & \mathbf{J}^{-1} \end{bmatrix} \det(\mathbf{J}) \tag{2.10}$$

A 2-D finite element model is constructed to simulate the vibration of a rigid circular disk in the full-space soil domain. By setting the disk motion to be in the direction of the y-axis, the symmetry can be exploited and half of the domain can be truncated as shown in Figure 2.3 (a). Now, the infinite physical domain can be represented by CFABC elements, denoted by squares with a letter inside. The CFABCs are placed around the standard finite element mesh except on the symmetry surface. The letters N, E, and S denote the location to the North, East, and South of the standard FE domain, respectively. The orientation of the local coordinate system is specific for each element. In the case of an edge absorber, the r-axis points to infinity while both the r-axis and the s-axis must do so in the case of a corner absorber, as shown in Figure 2.3 (b). To simplify the calculation, the absorbers are of equal x and y sizes, $h \times h$.

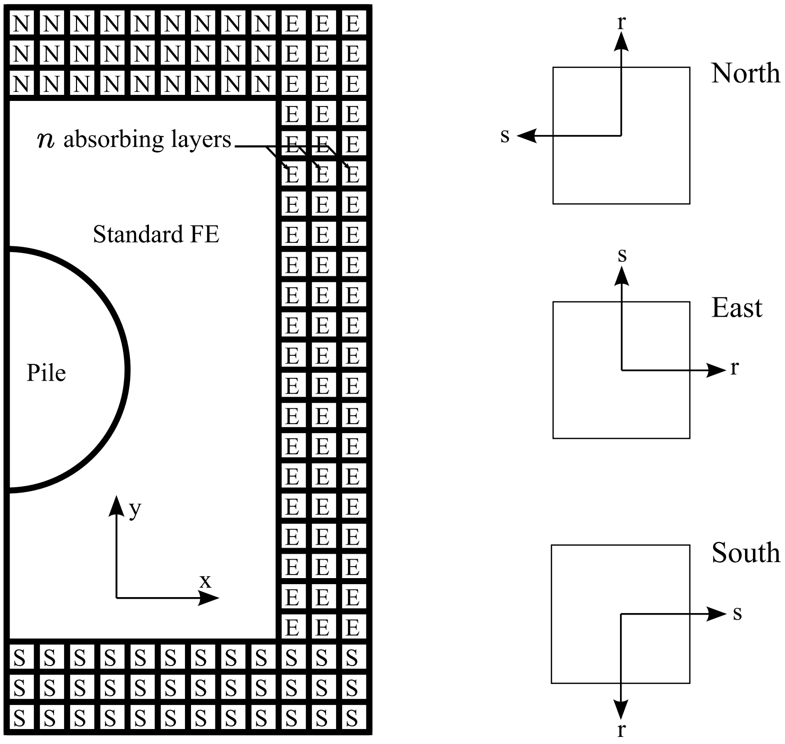

(a) (b)

Figure 2.3: (a) A finite element model of the rigid vibrating disk; (b) The orientations of local coordinates systems in CFABCs for three different locations

For the element orientations in Figure 2.3 (a), it can be seen that

$$\begin{aligned}
\mathbf{J}_{\mathbf{North}} &= \frac{h}{2}\begin{bmatrix} 0 & 1 \\ -1 & 0 \end{bmatrix} \\
\mathbf{J}_{\mathbf{East}} &= \frac{h}{2}\begin{bmatrix} 1 & 0 \\ 0 & 1 \end{bmatrix} \\
\mathbf{J}_{\mathbf{South}} &= \frac{h}{2}\begin{bmatrix} 0 & -1 \\ 1 & 0 \end{bmatrix} \qquad (2.11)
\end{aligned}$$

The determinants of the three Jacobian matrices are all equal to $h^2/4$. Next, the inverse of the Jacobian matrices, $\mathbf{J}$, can be expressed as follows;

$$\mathbf{J}_{\mathbf{North}}{}^{-1} = \frac{2}{h}\begin{bmatrix} 0 & -1 \\ 1 & 0 \end{bmatrix} = \frac{2}{h}\overline{\mathbf{J}}^{-1}_{North} \qquad (2.12)$$

$$\mathbf{J}_{\mathbf{East}}{}^{-1} = \frac{2}{h}\begin{bmatrix} 1 & 0 \\ 0 & 1 \end{bmatrix} = \frac{2}{h}\overline{\mathbf{J}}^{-1}_{East} \qquad (2.13)$$

$$\mathbf{J}_{\mathbf{South}}{}^{-1} = \frac{2}{h}\begin{bmatrix} 0 & 1 \\ -1 & 0 \end{bmatrix} = \frac{2}{h}\overline{\mathbf{J}}^{-1}_{South} \qquad (2.14)$$

Now, $\overline{\mathbf{D}}$ can be rewritten as

$$\begin{aligned}
\overline{\mathbf{D}} &= \frac{2}{h}\begin{bmatrix} \overline{\mathbf{J}}^{-1} & \mathbf{0} \\ \mathbf{0} & \overline{\mathbf{J}}^{-1} \end{bmatrix} \mathbf{D}^* \frac{2}{h}\begin{bmatrix} \overline{\mathbf{J}}^{-1} & \mathbf{0} \\ \mathbf{0} & \overline{\mathbf{J}}^{-1} \end{bmatrix} \left(\frac{h^2}{4}\right) \\
&= \begin{bmatrix} \overline{\mathbf{J}}^{-1} & \mathbf{0} \\ \mathbf{0} & \overline{\mathbf{J}}^{-1} \end{bmatrix} \mathbf{D}^* \begin{bmatrix} \overline{\mathbf{J}}^{-1} & \mathbf{0} \\ \mathbf{0} & \overline{\mathbf{J}}^{-1} \end{bmatrix} \qquad (2.15) \\
&= \begin{bmatrix} \overline{D}_{11} & \overline{D}_{12} & \overline{D}_{13} & \overline{D}_{14} \\ \overline{D}_{21} & \overline{D}_{22} & \overline{D}_{23} & \overline{D}_{24} \\ \overline{D}_{31} & \overline{D}_{32} & \overline{D}_{33} & \overline{D}_{34} \\ \overline{D}_{41} & \overline{D}_{42} & \overline{D}_{43} & \overline{D}_{44} \end{bmatrix} \qquad (2.16)
\end{aligned}$$

and, therefore, $\overline{\mathbf{D}}$ can be expressed as the summation of three matrices as follows:

$$\overline{\mathbf{D}} = \overline{\mathbf{D}}_r + \overline{\mathbf{D}}_s + \overline{\mathbf{D}}_{rs} \qquad (2.17)$$

where

$$\overline{\mathbf{D}}_r = \begin{bmatrix} \overline{D}_{11} & 0 & \overline{D}_{13} & 0 \\ 0 & 0 & 0 & 0 \\ \overline{D}_{31} & 0 & \overline{D}_{33} & 0 \\ 0 & 0 & 0 & 0 \end{bmatrix} \tag{2.18}$$

$$\overline{\mathbf{D}}_s = \begin{bmatrix} 0 & 0 & 0 & 0 \\ 0 & \overline{D}_{22} & 0 & \overline{D}_{24} \\ 0 & 0 & 0 & 0 \\ 0 & \overline{D}_{42} & 0 & \overline{D}_{44} \end{bmatrix} \tag{2.19}$$

$$\overline{\mathbf{D}}_{rs} = \begin{bmatrix} 0 & \overline{D}_{12} & 0 & \overline{D}_{14} \\ \overline{D}_{21} & 0 & \overline{D}_{23} & 0 \\ 0 & \overline{D}_{32} & 0 & \overline{D}_{34} \\ \overline{D}_{41} & 0 & \overline{D}_{43} & 0 \end{bmatrix} \tag{2.20}$$

Since the edge absorbers represent the unbounded domain in just the positive r direction while the corner absorbers need both r and s directions to simulate infinity, the imaginary stretching will be applied differently. Then, the derivations of the components for the equation of motion will be described separately for edge and corner absorbers.

2.1.1.1 Edge Absorber

The stretching will be performed in the r-direction as shown in Figure 2.4. The stretching factor, λ_j^r and λ_k^s, is determined as follows;

$$L_j^r = \frac{2c_j}{i\omega} = \left(\frac{2c_j}{i\omega h}\right) h = \lambda_j^r h \tag{2.21}$$

$$L_k^s = h = \lambda_k^s h \tag{2.22}$$

where

$$c_j = \frac{c_P}{\cos(\theta_j)}, \text{with } 0 \le \theta_j \le \frac{\pi}{2}$$

$$\theta_j = \frac{(j-1)\pi}{2n}$$

n Number of absorbing layers

c_P Pressure-wave velocity

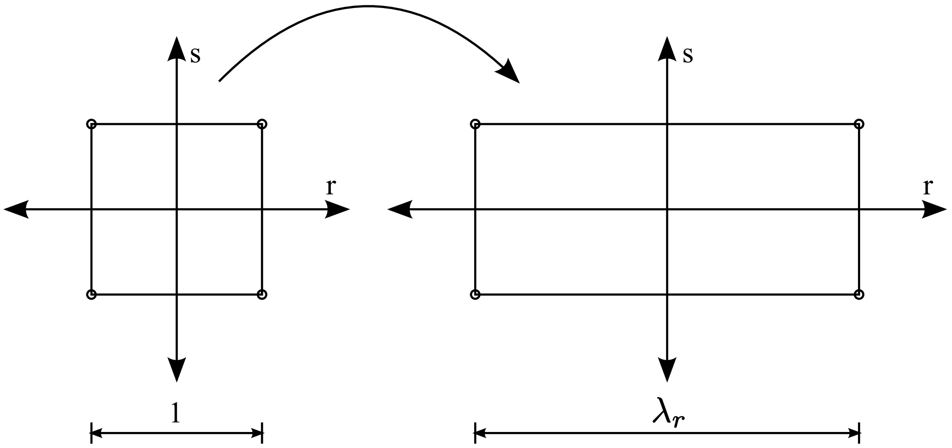

Figure 2.4: (a) Quadrilateral 4-node element before stretching; (b) Quadrilateral 4-node with imaginary stretching in one direction

The stress component influenced by stretch in the r direction, $\overline{\sigma}_r$, can be determined as follows:

$$\begin{aligned}\overline{\sigma}_r &= \frac{\lambda_j^s}{\lambda_k^r}\overline{\mathbf{D}}_r\overline{\varepsilon} \\ &= \frac{i\omega h}{2c_j}\overline{\mathbf{D}}_r\overline{\varepsilon} \qquad (2.23)\end{aligned}$$

Applying the inverse Fourier transform to both sides of Equation 2.23, one finds:

$$\overline{\sigma}_r = \frac{h}{2c_j}\overline{\mathbf{D}}_r\frac{\partial\overline{\varepsilon}}{\partial t} \qquad (2.24)$$

Similarly, the stress component affected by stretching in the s direction, $\overline{\sigma}_s$, is given as

$$\begin{aligned}\overline{\sigma}_s &= \frac{\lambda_j^r}{\lambda_k^s}\overline{\mathbf{D}}_s\overline{\varepsilon} \\ &= \frac{2c_j}{i\omega h}\overline{\mathbf{D}}_s\overline{\varepsilon} \qquad (2.25)\end{aligned}$$

and, by inverse Fourier transform action:

$$\overline{\sigma}_s = \left(\frac{2c_j}{h}\right)\overline{\mathbf{D}}_s\mathbf{B}\int_0^t u\,d\tau \qquad (2.26)$$

Finally, the stress components that will not be affected by stretch in any direction, $\overline{\sigma}_{rs}$ and $\overline{\sigma}_{sr}$, can be calculated by the following expression:

$$\overline{\sigma}_{rs} = \overline{\sigma}_{sr} = \overline{\mathbf{D}}_{rs}\overline{\varepsilon} \tag{2.27}$$

Now, the internal forces can be expressed as

$$\begin{aligned}
\mathbf{P} &= \int_{-1}^{1}\int_{-1}^{1} \mathbf{B}^T\left(\overline{\sigma}_r + \overline{\sigma}_s + \overline{\sigma}_{rs}\right) dr\, ds \\
&= \underbrace{\frac{h}{2c_j}\int_{-1}^{1}\int_{-1}^{1} \mathbf{B}^T\overline{\mathbf{D}}_r\mathbf{B}\, \mathrm{d}r\mathrm{d}s}_{\mathbb{C}^1}\ \dot{\mathbf{U}} \\
&\quad + \underbrace{\frac{2c_j}{h}\int_{-1}^{1}\int_{-1}^{1} \mathbf{B}^T\overline{\mathbf{D}}_s\mathbf{B}\, \mathrm{d}r\mathrm{d}s}_{\mathbb{R}}\ \int_0^t \mathbf{U}d\tau \\
&\quad + \underbrace{\int_{-1}^{1}\int_{-1}^{1} \mathbf{B}^T\overline{\mathbf{D}}_{rs}\mathbf{B}\, \mathrm{d}r\mathrm{d}s}_{\mathbb{K}}\ \mathbf{U}
\end{aligned} \tag{2.28}$$

Next, the inertia forces can be written as follows:

$$\begin{aligned}
I &= \int_{-1}^{1}\int_{-1}^{1} \rho\mathbf{N}^T\mathbf{N}\lambda_r \det(\mathbf{J})\, \mathrm{d}r\mathrm{d}s\, (i\omega)^2\hat{\mathbf{U}} \\
&= \frac{\rho h c_j}{2}\int_{-1}^{1}\int_{-1}^{1} \mathbf{N}^T\mathbf{N}\, \mathrm{d}r\mathrm{d}s\, (i\omega)\hat{\mathbf{U}}
\end{aligned} \tag{2.29}$$

Taking the inverse Fourier transform of the above equation, the expression in the time domain becomes:

$$I = \underbrace{\frac{\rho h c_j}{2}\int_{-1}^{1}\int_{-1}^{1} \mathbf{N}^T\mathbf{N}\, \mathrm{d}r\mathrm{d}s}_{\mathbb{C}^2}\ \dot{\mathbf{U}} \tag{2.30}$$

At time t_{n+1}, the equation of motion can be established as follows;

$$(\mathbb{C}^1 + \mathbb{C}^2)\dot{\mathbf{U}}^{n+1} + \mathbb{K}\mathbf{U}^{n+1} + \mathbb{R}\int_0^{t_{n+1}} \mathbf{U}\mathrm{d}\tau = 0 \tag{2.31}$$

Integrating by the Newmark constant acceleration scheme, one finds the following relationships between information at time t_n and time $t_{n+1} = t_n + \Delta t$:

$$\begin{aligned}
\dot{\mathbf{U}}^{n+1} &= \frac{2}{\Delta t}\Delta\mathbf{U} - \dot{\mathbf{U}}^{n} && (2.32)\\
\mathbf{U}^{n+1} &= \mathbf{U}^{n} + \Delta\mathbf{U} && (2.33)\\
\int_0^{t_{n+1}} \mathbf{U}\mathrm{d}\tau &= \mathbf{W}^{n+1} \\
&= \mathbf{W}^{n} + \frac{(\mathbf{U}^{n} + \mathbf{U}^{n+1})}{2}\Delta t \\
&= \mathbf{W}^{n} + \mathbf{U}^{n}\Delta t + \frac{\Delta\mathbf{U}\Delta t}{2} && (2.34)
\end{aligned}$$

Substituting the expression of $\dot{\mathbf{U}}^{n+1}$, $\mathbf{U}^{n+1}$, and $\mathbf{W}^{n+1}$ into Equation 2.31, the expression can be rewritten as

$$(\mathbb{C}^1+\mathbb{C}^2)(\frac{2}{\Delta t}\Delta\mathbf{U}-\dot{\mathbf{U}}^n)+\mathbb{K}(\mathbf{U}^n+\Delta\mathbf{U})+\mathbb{R}(\mathbf{W}^n+\mathbf{U}^n\Delta t+\frac{\Delta\mathbf{U}\Delta t}{2}) = 0 \quad (2.35)$$

Thus, the matrix of each of the edge-absorber finite elements is given by

$$(\mathbb{C}^1 + \mathbb{C}^2)\left(\frac{2}{\Delta t}\right) + \mathbb{K} + \mathbb{R}\left(\frac{\Delta t}{2}\right) \quad (2.36)$$

while the corresponding right-hand side is

$$(\mathbb{C}^1 + \mathbb{C}^2)\dot{\mathbf{U}}^n - \mathbb{K}\mathbf{U}^n - \mathbb{R}(\mathbf{W}^n + \mathbf{U}^n\Delta t) \quad (2.37)$$

Ideally, infinite discretization is required in the CFABC layers. Since this is not feasible, the wave reflection coefficient will be nonzero. However, reflections can be eliminated using midpoint integration, proposed by Guddati (2006), in evaluating the integrals in Equations 2.28 and 2.30. For the edge absorber, this reduced integration is exclusively performed along the r direction. Two Gauss points are employed for integration with respect to s. Figure 2.5 illustrates the integration rules for the edge absorber.

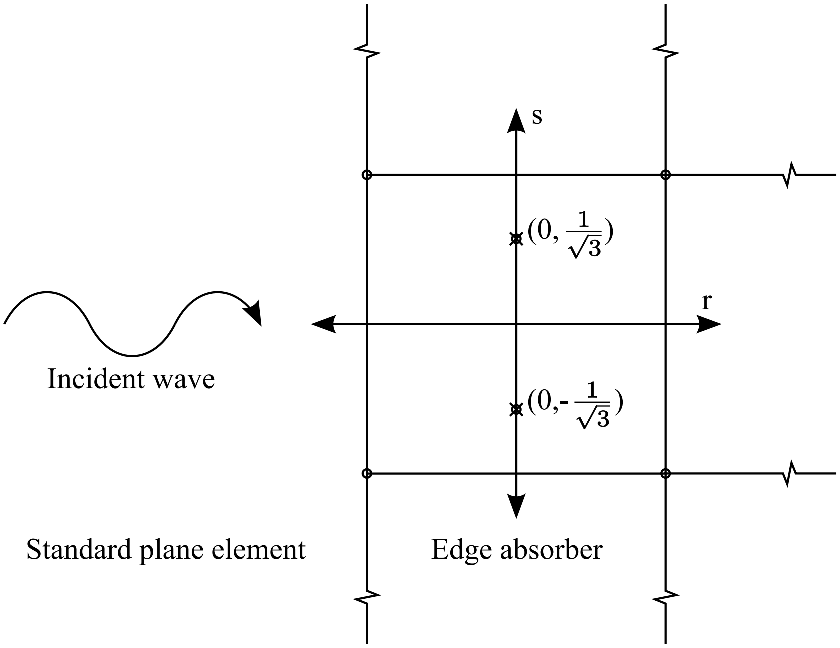

Figure 2.5: Midpoint integration rule applied in the r direction for edge absorbers

2.1.1.2 Corner Absorber

Corner absorbers will be stretched in both the r and the s directions, as shown in Figure 2.6, leading to a different derivation from edge absorbers. The imaginary lengths of the stretched element are given by:

$$\begin{aligned} L_j^r &= \frac{2c_j^r}{i\omega} = \left(\frac{2c_j^r}{i\omega h}\right) h \\ L_k^s &= \frac{2c_k^s}{i\omega} = \left(\frac{2c_k^s}{i\omega h}\right) h \end{aligned} \tag{2.38}$$

Thus, the stretching coefficients are:

$$\begin{aligned} \lambda_j^r &= \frac{2c_j^r}{i\omega h} \\ \lambda_k^s &= \frac{2c_k^s}{i\omega h} \end{aligned} \tag{2.39}$$

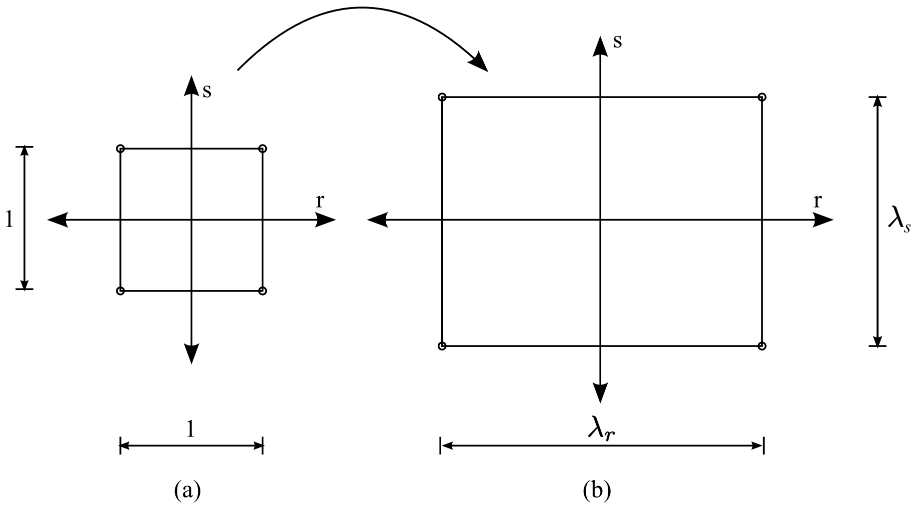

Figure 2.6: (a) Quadrilateral 4-node element before stretching; (b) Quadrilateral 4-node with imaginary stretching in two directions

Now, the stress component affected by the stretch in the r-direction can be expressed as

$$\begin{aligned} \overline{\sigma}_r &= \frac{\lambda_k^s}{\lambda_j^r}\overline{\mathbf{D}}_r\overline{\varepsilon} \\ &= \frac{c_k^s}{c_j^r}\overline{\mathbf{D}}_s\overline{\varepsilon} \end{aligned} \tag{2.40}$$

Next, consider the effect from the stretch in the s-direction:

$$\begin{aligned} \overline{\sigma}_s &= \frac{\lambda_j^r}{\lambda_k^s}\overline{\mathbf{D}}_s\overline{\varepsilon} \\ &= \frac{c_j^r}{c_k^s}\overline{\mathbf{D}}_s\overline{\varepsilon} \end{aligned} \tag{2.41}$$

Finally, the stress components, not affected by any stretch, can be written as

$$\overline{\sigma}_{rs} = \overline{\sigma}_{sr} = \overline{\mathbf{D}}_{rs}\overline{\varepsilon} \tag{2.42}$$

Now, the internal forces can be expressed in terms of the above stress components as follows:

$$\begin{aligned}\mathbf{P} &= \int_{-1}^{1}\int_{-1}^{1} \mathbf{B}^T \left(\overline{\sigma}_r + \overline{\sigma}_s + \overline{\sigma}_{rs}\right)\, \mathrm{d}r\mathrm{d}s \\ &= \underbrace{\int_{-1}^{1}\int_{-1}^{1} \mathbf{B}^T \left(\frac{c_k^s}{c_j^r}\overline{\mathbf{D}}_r + \frac{c_j^r}{c_k^s}\overline{\mathbf{D}}_s + \overline{\mathbf{D}}_{rs}\right)\mathbf{B}\,\mathrm{d}r\mathrm{d}s}_{\mathbb{K}^1}\,\mathbf{U} \qquad (2.43)\end{aligned}$$

Additionally, inertia forces can be computed from the following expression;

$$\mathbf{I} = \int_{-1}^{1}\int_{-1}^{1} \rho\mathbf{N}^T\mathbf{N}\left(\frac{2c_j^r}{(i\omega)h}\right)\left(\frac{2c_k^s}{(i\omega)h}\right)\det(\mathbf{J})\,\mathrm{d}r\mathrm{d}s(i\omega)^2\hat{\mathbf{U}} \qquad (2.44)$$

Applying the inverse Fourier transform action, Equation 2.44 can be rewritten as in the following form:

$$\mathbf{I} = \underbrace{(c_j^r c_k^s \rho)\int_{-1}^{1}\int_{-1}^{1} \mathbf{N}^T\mathbf{N}\,\mathrm{d}r\mathrm{d}s}_{\mathbb{K}^2}\,\mathbf{U} \qquad (2.45)$$

and, the equation of motion at time t_{n+1} for corner absorbers becomes:

$$\begin{gathered}(\mathbb{K}^1 + \mathbb{K}^2)\mathbf{U}^{n+1} = \mathbf{0} \\ (\mathbb{K}^1 + \mathbb{K}^2)(\mathbf{U}^n + \Delta\mathbf{U}) = \mathbf{0}\end{gathered}$$

Thus, the matrix for corner-absorber elements is:

$$\mathbb{K}^1 + \mathbb{K}^2 \qquad (2.46)$$

and the right-hand side:

$$-(\mathbb{K}^1 + \mathbb{K}^2)\mathbf{U}^n \qquad (2.47)$$

For corner absorber, the physical domain is truncated in both r and s directions. As a result, one integration point is used at the center of the element, as shown in Figure 2.7.

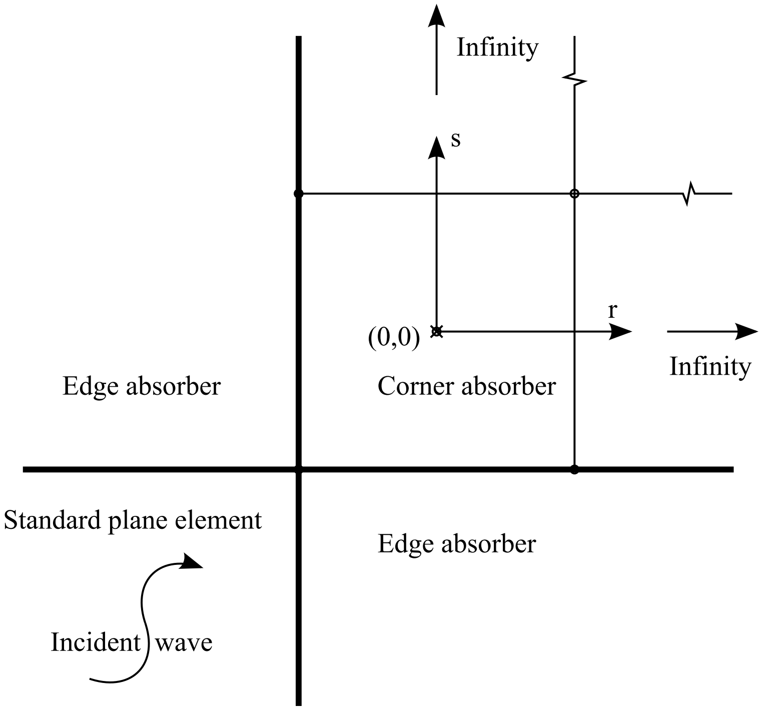

Figure 2.7: Midpoint integration rule applied in the r and s direction for corner absorbers

2.1.2 The Validation of CFABCs Implementation by Semi-infinite Soil Model under Gaussian Explosion

Next, the performance of the CFABCs will be examined by the half-space plane-strain model under Gaussian explosion in space and time exhibited in Figure 2.8. Figures 2.9 to 2.17 illustrate the stress wave propagating through the standard finite element domain and perfectly absorbed by CFABCs. No reflection can be deciphered. Additionally, the nodal displacements at the center of the explosion and on the absorbing boundary at the upper left corner are monitored. After the passage of the stress wave, the nodes are asymptotically displaced back to zero as shown in Figures 2.18 (a) and (b). This is a test of the CFABC formulation ad implementation. Results for this test have been reported by Guddati and Lim (2006).

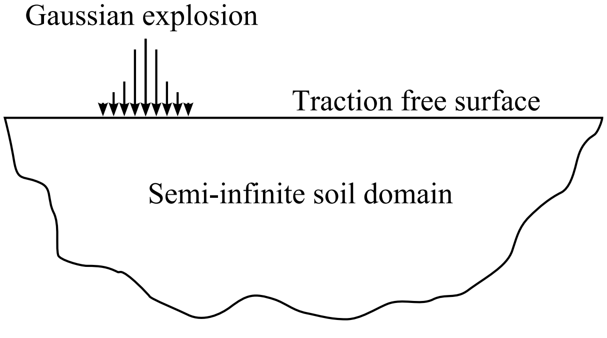

(a)

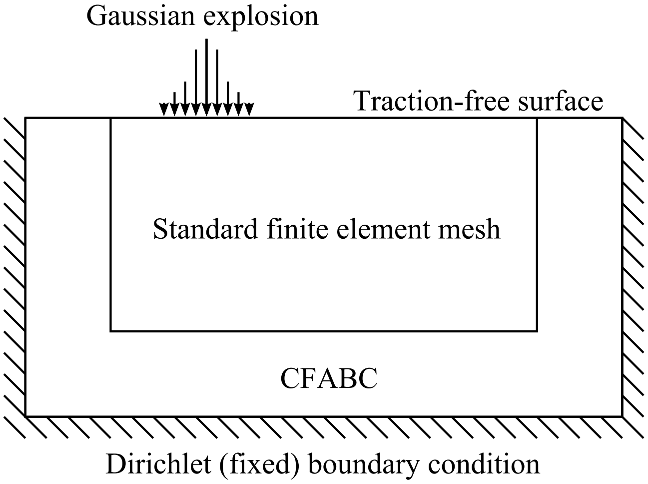

(b)

Figure 2.8: (a) The semi-infinite plane-strain soil domain under Gaussian explosion: (b) The plane-strain finite element model surrounded by CFABCs for the representation of unbounded domain under Gaussian explosion

Figure 2.9: σ_y distribution at 0.0020 second

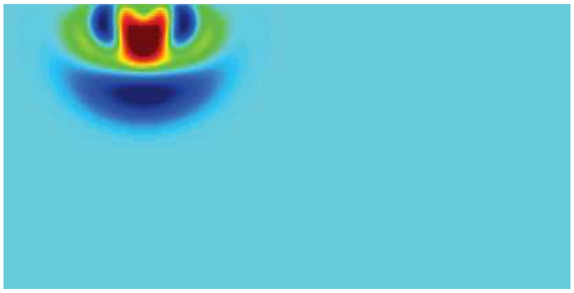

Figure 2.10: σ_y distribution at 0.0025 second

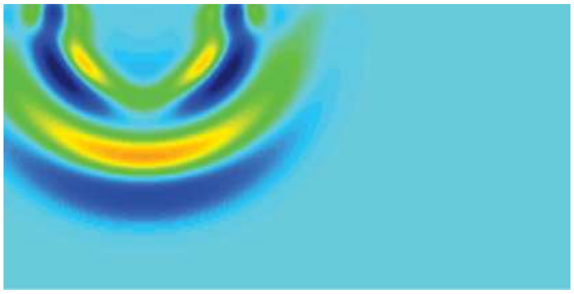

Figure 2.11: σ_y distribution at 0.0040 second

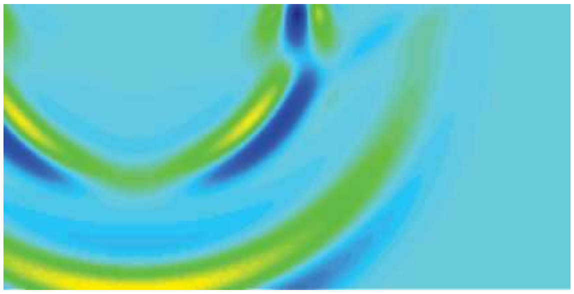

Figure 2.12: σ_y distribution at 0.0060 second

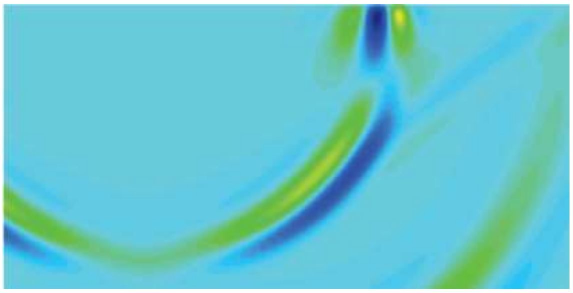

Figure 2.13: σ_y distribution at 0.0080 second

Figure 2.14: σ_y distribution at 0.0110 second

Figure 2.15: σ_y distribution at 0.0150 second

Figure 2.16: σ_y distribution at 0.0170 second

Figure 2.17: σ_y distribution at 0.0200 second

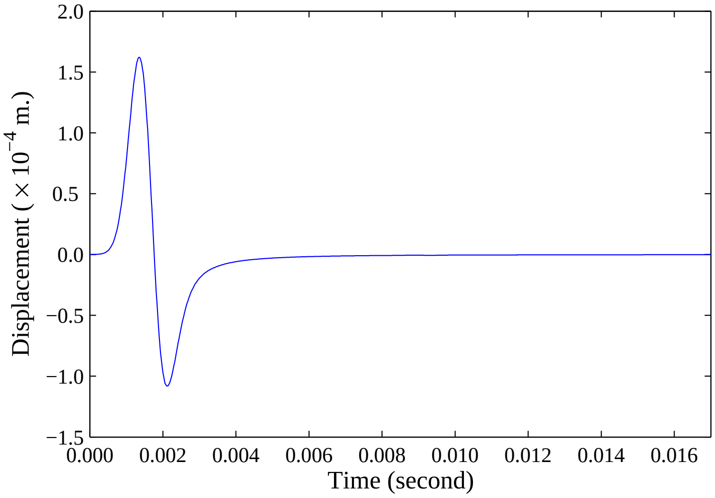

(a)

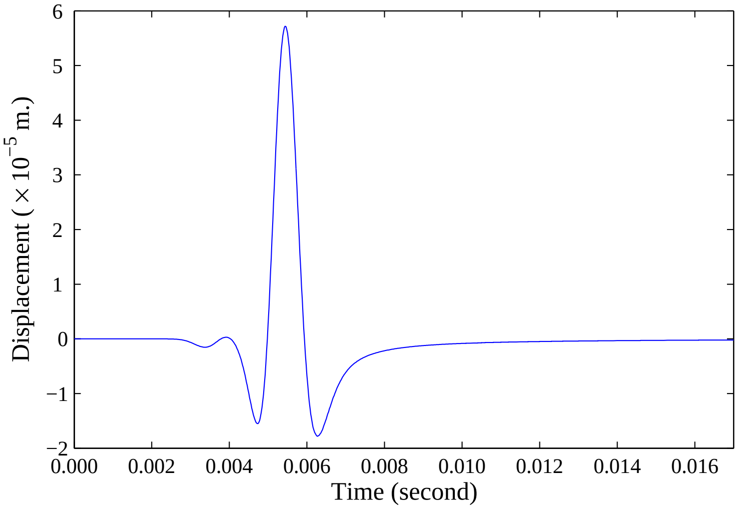

(b)

Figure 2.18: (a) Nodal x-displacement at the center of explosion versus time: (b) Nodal x-displacement at the upper-left corner of the standard finite element domain

2.1.3 Closed-Form Solution of the Disk Stiffness

The exact solution for the moving disk in unbounded plane-strain domain was presented by Baranov (1967) and Novak et al (1978). Due to the assumed plane-strain conditions, the variations with respect to the z direction are taken as zero. The disk is assumed to be rigid and massless, and the motion is exclusively in-plane and harmonic. Then, the governing viscoelastic equation in cylindrical coordinate system can be expressed as:

$$\begin{aligned}(\lambda+2G)\frac{\partial\Delta}{\partial r}-\frac{2G}{r}\frac{\partial\omega_z}{\partial\theta}+2G\frac{\partial\omega_\theta}{\partial z} &= \rho\frac{\partial^2 u}{\partial t^2}\\ (\lambda+2G)\frac{\partial\Delta}{r\partial\theta}-2G\frac{\partial\omega_r}{\partial z}+2G\frac{\partial\omega_z}{\partial r} &= \rho\frac{\partial^2 v}{\partial t^2}\end{aligned} \tag{2.48}$$

where

$$\begin{aligned}\Delta &= \frac{1}{r}\frac{\partial}{\partial r}(ru)+\frac{1}{r}\frac{\partial v}{\partial\theta}+\frac{\partial w}{\partial z}\\ \omega_r &= \frac{1}{2}\Big(\frac{1}{r}\frac{\partial w}{\partial\theta}-\frac{\partial v}{\partial z}\Big)\\ \omega_\theta &= \frac{1}{2}\Big(\frac{\partial u}{\partial z}-\frac{\partial w}{\partial r}\Big)\\ \omega_z &= \frac{1}{2}\Big(\frac{1}{r}\frac{\partial(rv)}{\partial r}-\frac{1}{r}\frac{\partial u}{\partial\theta}\Big)\end{aligned} \tag{2.49}$$

As the derivatives with respect to z are assumed to be zero, the above governing equations can be rearranged into a simpler form as follows:

$$\begin{aligned}(\lambda+2G)\frac{\partial\Delta}{\partial r}-\frac{2G}{r}\frac{\partial\omega_z}{\partial\theta} &= \rho\frac{\partial^2 u}{\partial t^2}\\ (\lambda+2G)\frac{\partial\Delta}{r\partial\theta}+2G\frac{\partial\omega_z}{\partial r} &= \rho\frac{\partial^2 v}{\partial t^2}\end{aligned} \tag{2.50}$$

where

$$\begin{aligned}\Delta &= \frac{1}{r}\frac{\partial}{\partial r}(ru)+\frac{1}{r}\frac{\partial v}{\partial\theta}\\ \omega_z &= \frac{1}{2}\Big(\frac{1}{r}\frac{\partial}{\partial r}(rv)-\frac{1}{r}\frac{\partial u}{\partial\theta}\Big)\end{aligned} \tag{2.51}$$

A closed-form relationship between the dynamic disk stiffness and the dimensionless frequency, a_0, is established as follows;

$$k_u = \pi G a_0^2 T \tag{2.52}$$

where

$$\begin{aligned}
T &= -\frac{4K_1(b_0^*)K_1(a_0^*) + a_0^*K_1(b_0^*)K_0(a_0^*) + b_0^*K_0(b_0^*)K_1(a_0^*)}{b_0^*K_0(b_0^*)K_1(a_0^*) + a_0^*K_1(b_0^*)K_0(a_0^*) + b_0^*a_0^*K_0(b_0^*)K_0(a_0^*)} \\
a_0^* &= \frac{r_0\omega}{c_s}i \\
b_0^* &= \frac{a_0^*}{\eta} \\
\eta &= \sqrt{\frac{2(1-\nu)}{1-2\nu}} \\
i &= \sqrt{-1}
\end{aligned} \tag{2.53}$$

Plots of $Re[k_u]$ and $Im[k_u]$ vs. the dimensionless frequency, a_0, for different values of Poisson's ratio are provided in Figure 2.19.

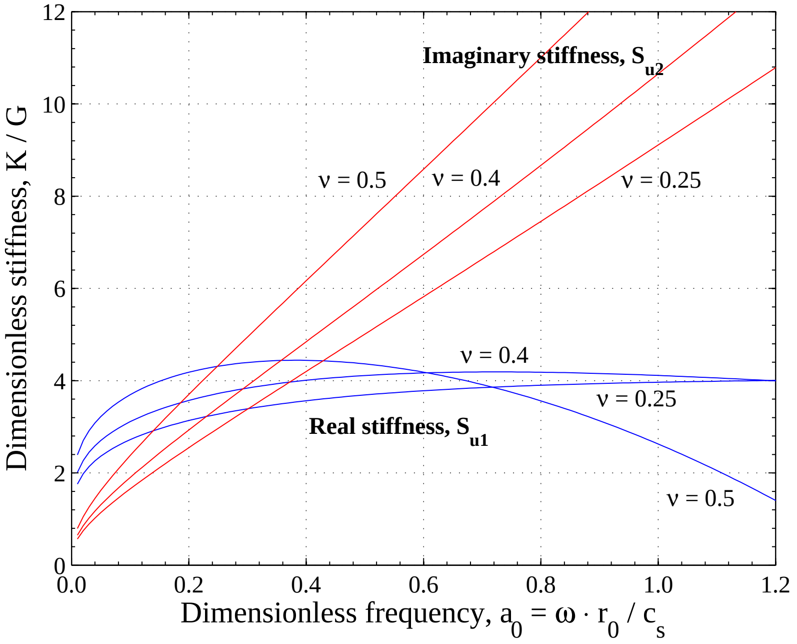

Figure 2.19: Real and imaginary parts of the dimensionless stiffness of the horizontally vibrating disk for Poisson's ratios = 0.25, 0.4, and 0.5

2.1.4 Verification of 2-D Disk Model Stiffness

Next, the disk model in the unbounded soil domain, shown in Figure 2.3 will be examined through a range of the dimensionless frequency. Both the amplitude of the soil dimensionless resistance, F, and the phase lag between F and the dimensionless disk displacement, U, will be monitored and compared with the exact solution.

The plots in Figure 2.20 (a,b), 2.21 (a,b), 2.22 (a,b), and 2.23 (a,b) are the soil dimensionless resisting forces (thick line) and dimensionless displacement (thin line) plotted vs. time for different dimensionless frequencies, equal to 0.50 to 1.30. The harmonic motions of the disk is prescribed with amplitude of 0.5 unit. Figure 2.24 shows the comparison over a range of frequencies, and, clearly, the force response is in excellent agreement with the exact solution.

Also, the phase difference between the displacement and soil resistance can be calculated from the expression of harmonic force, $F(t)$, and harmonic displacement, $U(t)$:

$$\begin{aligned} F(t) &= \mathbb{F}\sin(\omega t + \phi) \\ \phi &= \omega \cdot \Delta t \\ U(t) &= \mathbb{U}\sin(\omega t) \end{aligned} \tag{2.54}$$

The time difference, Δt, between F and U can be extracted from the finite element solution as demonstrated in Figure 2.25.

The phase difference, ϕ, can also be calculated from the exact solution as follows;

$$\phi = \arctan\left(\frac{S_{u2}}{S_{u1}}\right) \tag{2.55}$$

where S_{u1} and S_{u2} are the real and imaginary disk stiffnesses. In all cases analyzed, the difference between the computed and exact values of ϕ is negligible.

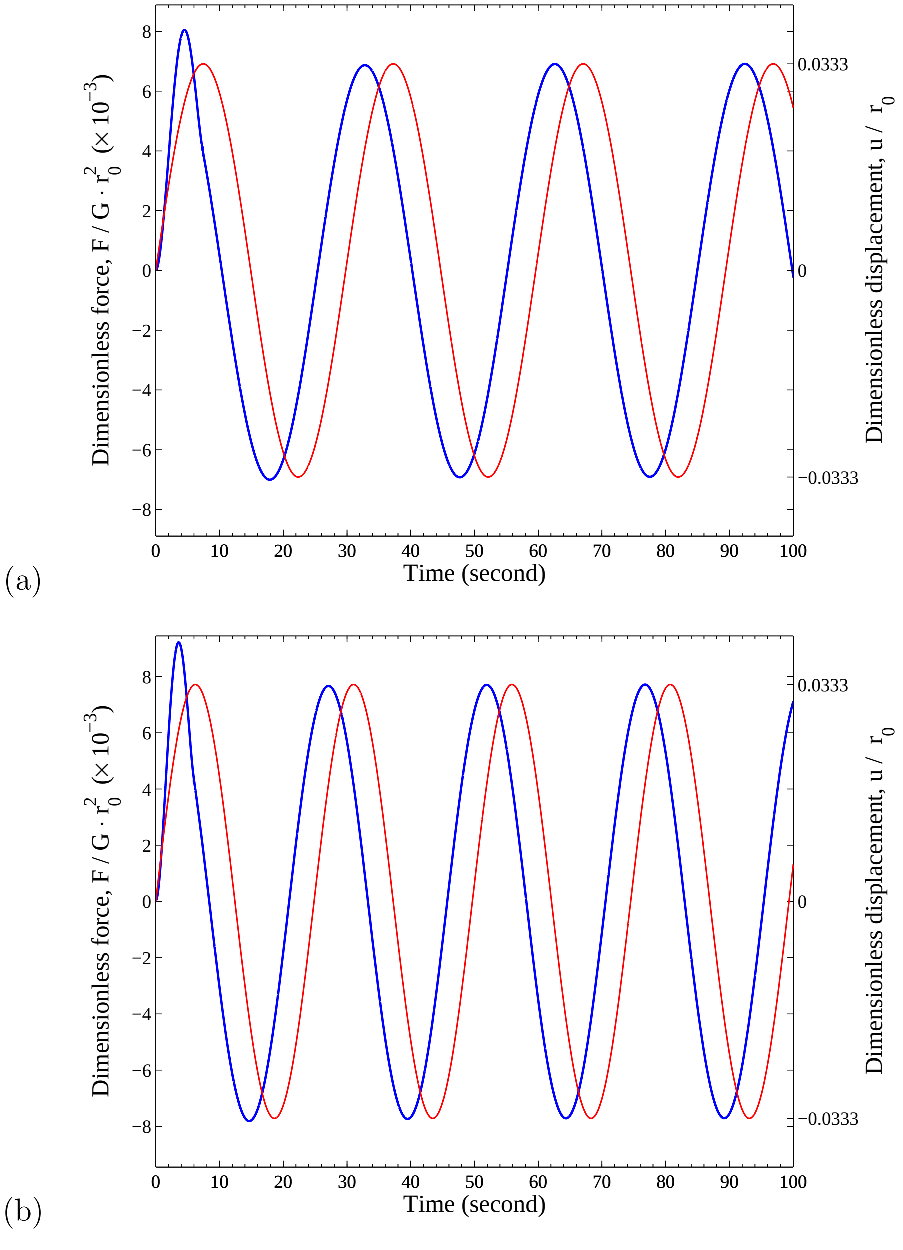

Figure 2.20: (a) Dimensionless force and dimensionless displacement plot vs. time for $a_0 = 0.50$: (b) Dimensionless force and dimensionless displacement plot with vs. for $a_0 = 0.60$ ($a_0 = \omega \cdot r_0/c_s$)

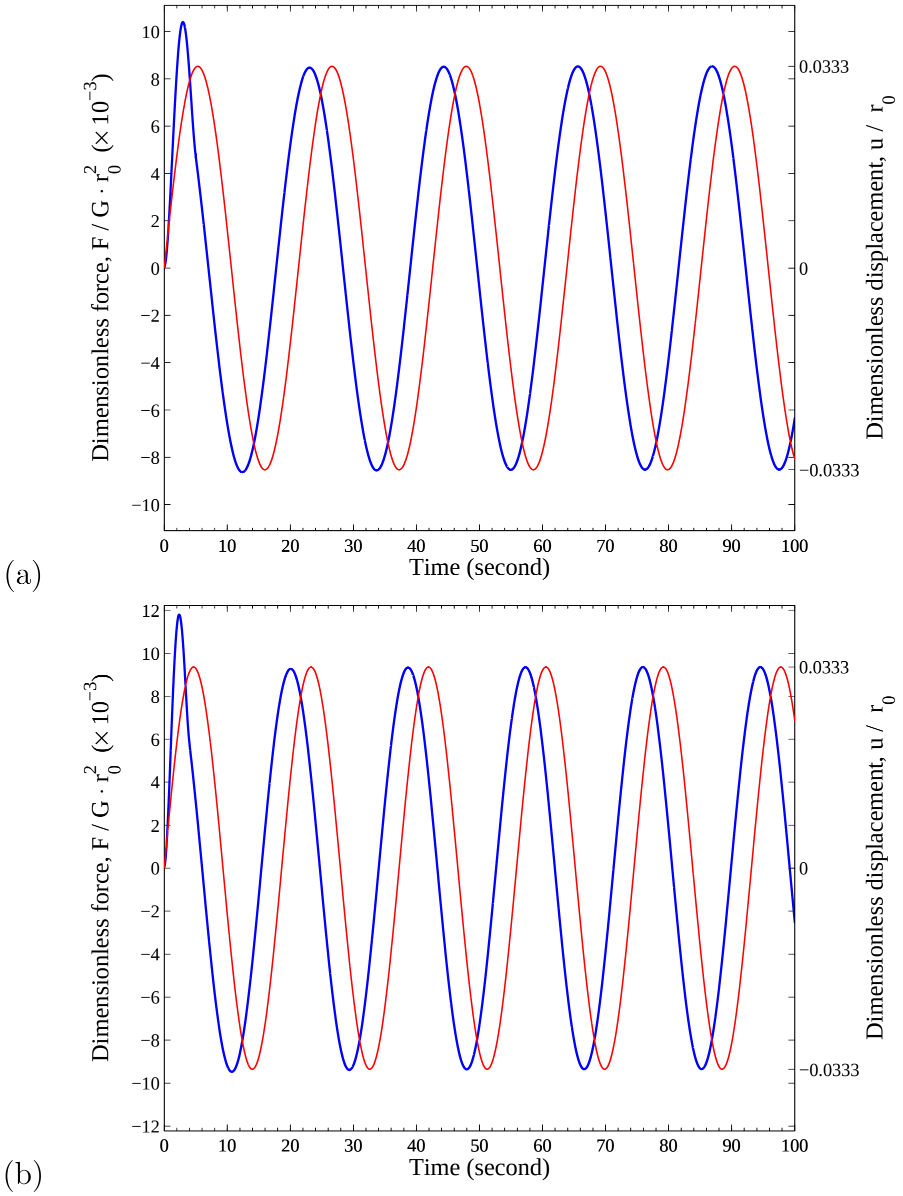

Figure 2.21: (a) Dimensionless force and dimensionless displacement plot vs. time for $a_0 = 0.70$: (b) Dimensionless force and dimensionless displacement plot vs. time for $a_0 = 0.80$ ($a_0 = \omega \cdot r_0/c_s$)

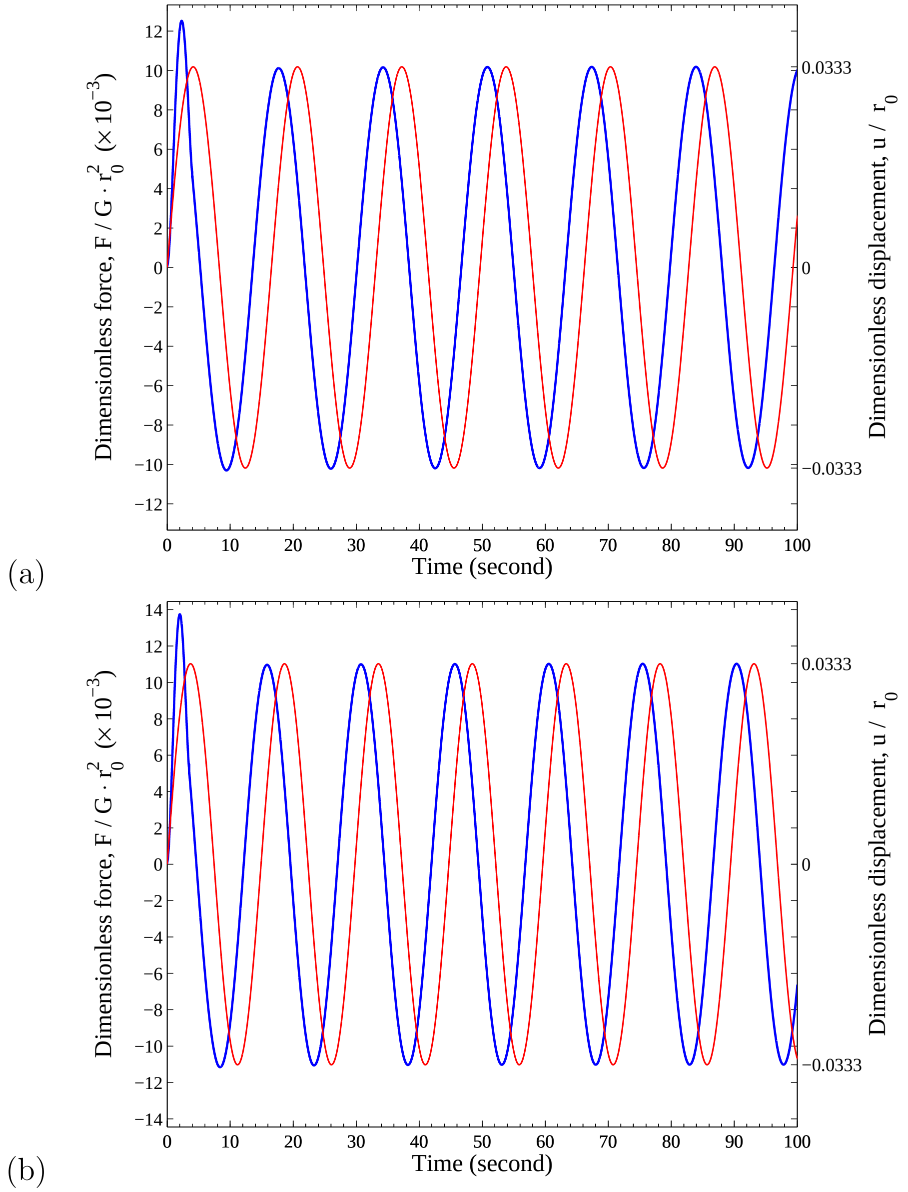

Figure 2.22: (a) Dimensionless force and dimensionless displacement plot vs. time for $a_0 = 0.90$: (b) Dimensionless force and dimensionless displacement plot vs. time for $a_0 = 1.00$ ($a_0 = \omega \cdot r_0 / c_s$)

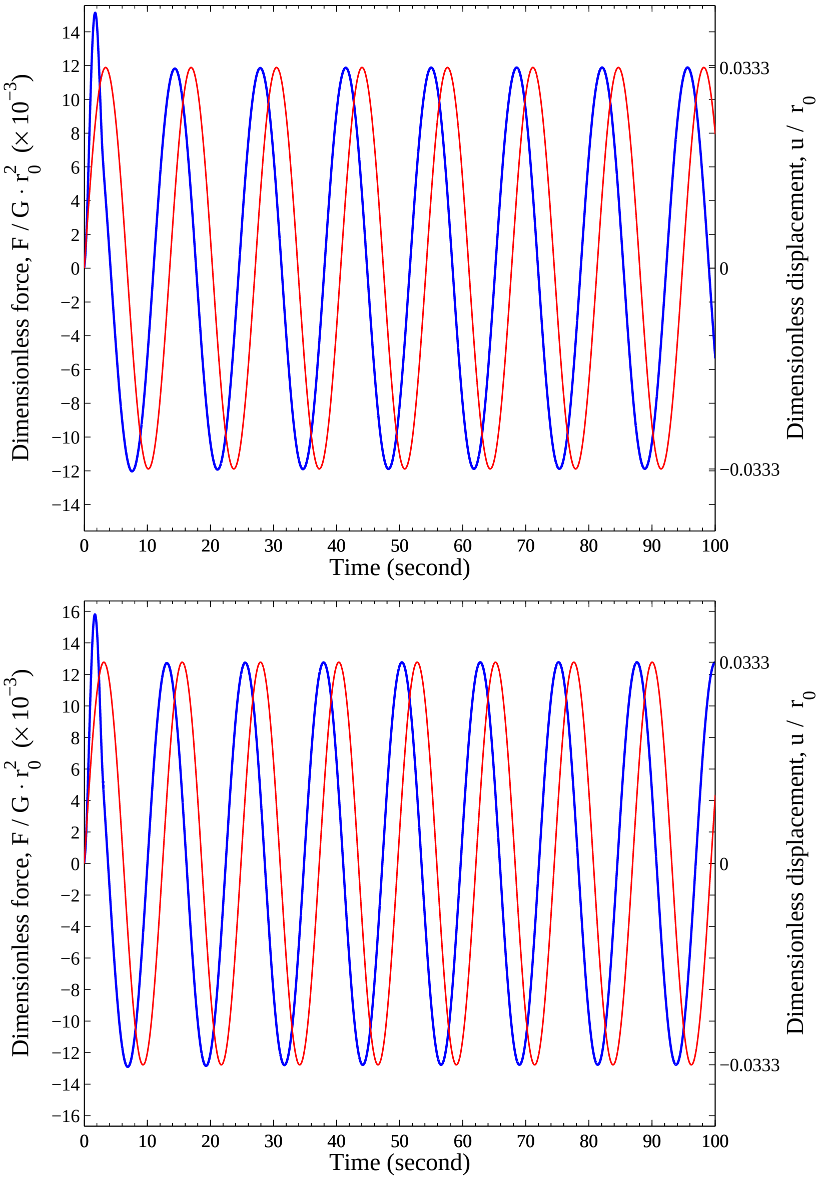

(a)

(b)

Figure 2.23: (a) Dimensionless force and dimensionless displacement plot vs. time for $a_0 = 1.10$: (b) Dimensionless force and dimensionless displacement plot vs. time for $a_0 = 1.20$ ($a_0 = \omega \cdot r_0/c_s$)

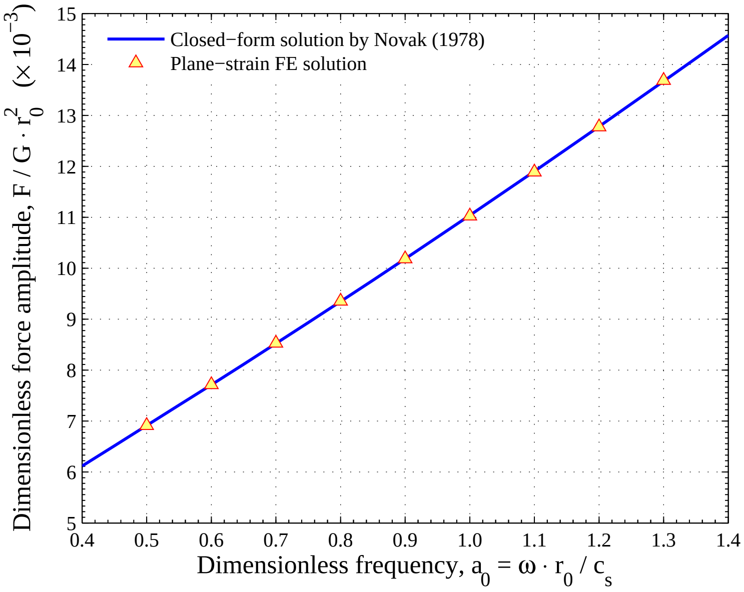

Figure 2.24: Dimensionless force amplitude plotted vs. dimensionless frequency from the exact and finite-element solutions.

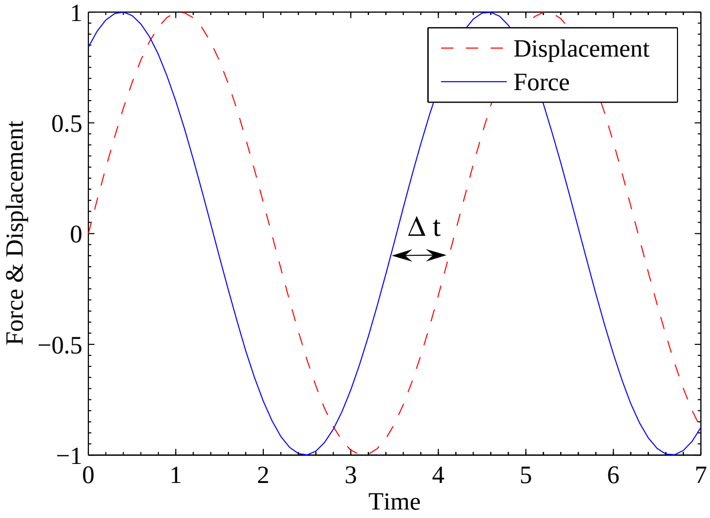

Figure 2.25: Time difference between harmonic force and harmonic displacement

Chapter 3

Vibrations of a Rigid Disk in Unbounded Soil: One-Dimensional Finite-Element Model

Since the Dynamic Winkler Foundation Model has been widely accepted and implemented in the analysis of laterally loaded piles, the initial objective of this research was to develop a simple model representing the characteristics of a vibrating disk in an infinite soil slice. The new vibrating-disk model was to overcome some shortcomings in the existing dynamic spring and dashpot representation, e.g. the frequency dependence and difficulties in performing inelastic analysis. The new one-dimensional element, computationally inexpensive, is developed to realistically simulate the behavior of the vibrating disk under general conditions, including transient dynamic analysis and the occurrence of inelasticity.

This chapter will first provide the formulation of the one-dimensional element, followed by performance validation. The comparison between results from 1-D plane model and the available exact solution as well as the solution from full 2-D plane model will be made for both purely-elastic and inelastic soil behavior. Finally, the 1-D model will be combined with pile elements to examine the efficiency of the independent soil-slice idealization.

3.1 One-Dimensional Element Formulation

A cylindrical coordinate system is selected for the 1-D element formulation (Figure 3.1). The problem of vibrating disk is symmetric about the direction of the disk motion in the x-axis, but antisymmetric about the orthogonal axis. If the assumption of purely-elastic behavior holds, the soil displacements can be written as follows:

$$\begin{aligned} u(r,\theta,t) &= U(r,t)\cdot\cos(\theta) && (3.1)\\ v(r,\theta,t) &= -V(r,t)\cdot\sin(\theta) && (3.2) \end{aligned}$$

Next, the strain components can be calculated from the displacements in Equations 3.1 and 3.2 as expressed in the following:

$$\begin{aligned} \varepsilon_r &= \frac{\partial u}{\partial r} \\ &= \frac{\partial U}{\partial r}\cdot\cos(\theta) && (3.3)\\ \varepsilon_\theta &= \frac{u}{r}+\frac{1}{r}\frac{\partial v}{\partial\theta} \\ &= \frac{U}{r}\cdot\cos(\theta)-\frac{V}{r}\cdot\cos(\theta) \\ &= \frac{U-V}{r}\cdot\cos(\theta) && (3.4)\\ \varepsilon_z &= 0 && (3.5) \end{aligned}$$

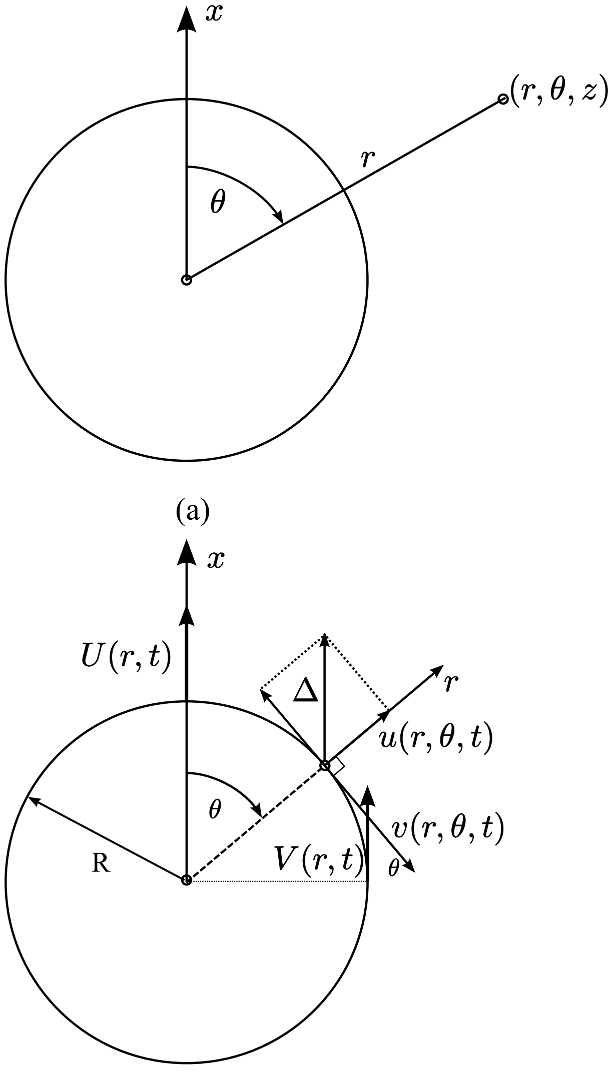

(a)

(b)

Figure 3.1: (a) Disk in a cylindrical coordinate system, (b) radial and tangential displacements produced by the disk displacement, Δ

$$
\begin{aligned}
\gamma_{r\theta} &= \frac{\partial v}{\partial r} - \frac{v}{r} + \frac{1}{r}\frac{\partial u}{\partial \theta} \\
&= -\frac{\partial V}{\partial r} \cdot \sin(\theta) + \frac{V}{r} \cdot \sin(\theta) - \frac{U}{r} \cdot \sin(\theta) \\
&= -\left(\frac{\partial V}{\partial r} + \frac{U - V}{r}\right) \cdot \sin(\theta) \qquad (3.6)
\end{aligned}
$$

$$\gamma_{\theta z} = 0 \qquad (3.7)$$

$$\gamma_{zr} = 0 \qquad (3.8)$$

Now, the soil domain is discretized using 4-node linear ring elements (1D-2DOF) as shown in Figure 3.2. The nodal locations and the directions of nodal displacements, U_1, U_2, V_1, and V_2 are also shown. By performing the finite-element discretization, the soil displacements U and V can be approximated using linear shape functions:

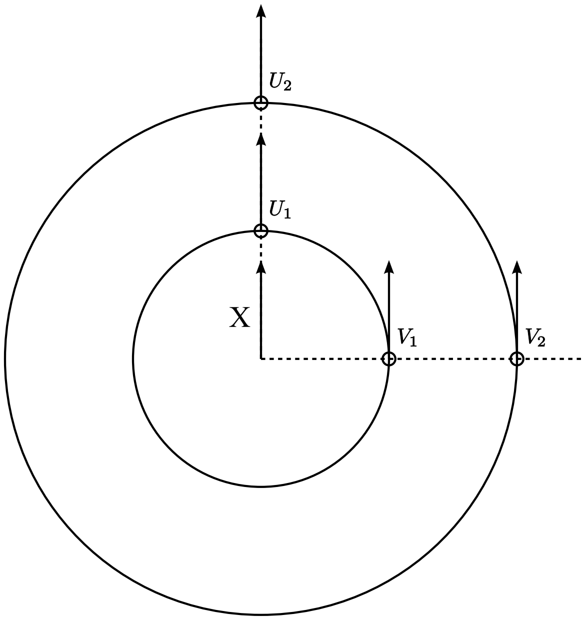

Figure 3.2: One-dimensional ring element with four degrees of freedom

$$\begin{aligned} U(r,t) &\approx \sum_{i=1}^{2} U_i(t)\cdot N_i \\ V(r,t) &\approx \sum_{i=1}^{2} V_i(t)\cdot N_i \end{aligned} \tag{3.9}$$

where U_i is the radial displacement corresponding to the location of $\theta = 0$ at node i: V_i is the azimuthal displacement corresponding to the location of $\theta = \pi/2$ at node i: N_i is the linear shape functions corresponding to the node i, expressed as a function of the local coordinate, ζ, as follows:

$$\begin{aligned} N_1 &= \frac{1}{2}(1-\zeta) \\ N_2 &= \frac{1}{2}(1+\zeta) \end{aligned} \tag{3.10}$$

The nonzero strain components can be expressed in terms of nodal displacements and interpolation functions as follows:

$$\begin{aligned} \begin{bmatrix} \varepsilon_r \\ \varepsilon_\theta \\ \gamma_{r\theta} \end{bmatrix} &= \begin{bmatrix} \dfrac{\mathrm{d}N_1}{\mathrm{d}r} & 0 & \dfrac{\mathrm{d}N_2}{\mathrm{d}r} & 0 \\ \dfrac{N_1}{r} & -\dfrac{N_1}{r} & \dfrac{N_2}{r} & -\dfrac{N_2}{r} \\ \dfrac{N_1}{r} & \dfrac{\mathrm{d}N_1}{\mathrm{d}r} - \dfrac{N_1}{r} & \dfrac{N_2}{r} & \dfrac{\mathrm{d}N_2}{\mathrm{d}r} - \dfrac{N_2}{r} \end{bmatrix} \cdot \begin{bmatrix} U_1 \\ V_1 \\ U_2 \\ V_2 \end{bmatrix} \\ \underset{\sim}{\varepsilon} &= \underset{\sim}{B} \cdot \underset{\sim}{U} \end{aligned} \tag{3.11}$$

Next, assuming elastic behavior, the constitutive relations for the nonzero stress components can be cast in the form:

$$\begin{aligned} \begin{bmatrix} \sigma_r \\ \sigma_\theta \\ \tau_{r\theta} \end{bmatrix} &= \begin{bmatrix} \lambda + 2G & \lambda & 0 \\ \lambda & \lambda + 2G & 0 \\ 0 & 0 & G \end{bmatrix} \begin{bmatrix} \varepsilon_r \\ \varepsilon_\theta \\ \gamma_{r\theta} \end{bmatrix} \\ \underset{\sim}{\sigma} &= \underset{\sim}{D} \cdot \underset{\sim}{\varepsilon} \end{aligned} \tag{3.12}$$

Regarding to the displacement variation in Equations 3.1 and 3.2, the stress variations with respect to θ are given by

$$\begin{aligned}
\sigma_r(r,\theta,t) &= \sigma_r(r,0,t)\cdot\cos(\theta) && (3.13)\\
\sigma_\theta(r,\theta,t) &= \sigma_\theta(r,0,t)\cdot\cos(\theta) && (3.14)\\
\tau_{r\theta}(r,\theta,t) &= -\tau_{r\theta}(r,\pi/2,t)\cdot\sin(\theta) && (3.15)
\end{aligned}$$

Now, the soil reaction, P, on the disk with radius equal to R, can be calculated from two stresses acting on the disk surface as shown in Figure 3.3. The contribution of σ_r and $\tau_{r\theta}$ in the x direction are taken into account by $\cos(\theta)$ and $-\sin(\theta)$ respectively. Then, the soil reaction on the disk can be determined by

$$\begin{aligned}
P &= \int_0^{2\pi}\Big[[\sigma_r(R,0,t)\cdot\cos(\theta)\cdot\cos(\theta)] - [\tau_{r\theta}(R,\pi/2,t)\cdot\sin(\theta)\cdot(-\sin(\theta))]\Big]\mathrm{d}\theta\\
&= \pi R[\sigma_r(R,0,t)+\tau_{r\theta}(R,\pi/2,t)] \qquad (3.16)
\end{aligned}$$

As can be seen, the integration with respect to θ leads to the constant factor π multiplying the sum of radial and shearing stresses at $\theta = 0$ and $\theta = \pi/2$, respectively.

3.1.1 Stiffness Matrix

First, consider the virtual work done by the stress in an infinitesimal soil element. The virtual strain-energy density, $\mathbb{E}^*$, is given by

$$\mathbb{E}^* = \delta\underset{\sim}{\varepsilon}^T\underset{\sim}{\sigma} \qquad (3.17)$$

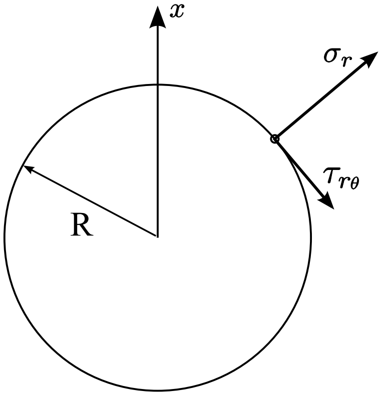

Figure 3.3: Positive sense of σ_r and $\tau_{r\theta}$ used in soil reaction force calculation

In an infinitesimal soil element in cylindrical coordinates, shown in Figure 3.4, the strain energy can be written as

$$\mathbb{E}\, r\mathrm{d}r\, \mathrm{d}\theta = \left(\delta \underset{\sim}{\varepsilon}^T \cdot \underset{\sim}{\sigma}\right) \cdot (r\mathrm{d}\theta) \cdot (\mathrm{d}r) \tag{3.18}$$

Thus, the internal virtual work in a ring element is:

$$\mathbb{W}_{int} = \int_0^{2\pi} \int_{r_i}^{r_o} \delta \underset{\sim}{\varepsilon}^T \underset{\sim}{\sigma}\, r\, \mathrm{d}r\mathrm{d}\theta \tag{3.19}$$

where r_i is the inner radius of the ring and r_o is the outer radius:
Since the inner product from the virtual strain and stress is

$$\begin{aligned} \delta \underset{\sim}{\varepsilon}^T \cdot \underset{\sim}{\sigma} &= \delta\varepsilon_r(r,0) \cdot \sigma_r(r,0) \cdot \cos^2(\theta) + \delta\varepsilon_\theta(r,0) \cdot \sigma_\theta(r,0) \cdot \cos^2(\theta) \\ &\quad + \delta\gamma_{r\theta}(r,\pi/2) \cdot \tau_{r\theta}(r,\pi/2) \cdot \sin^2(\theta) \end{aligned} \tag{3.20}$$

The integration with respect to θ of the trigonometry functions $\sin^2(\theta)$ and $\cos^2(\theta)$ can be replaced by the constant factor π and Equation 3.19 will be

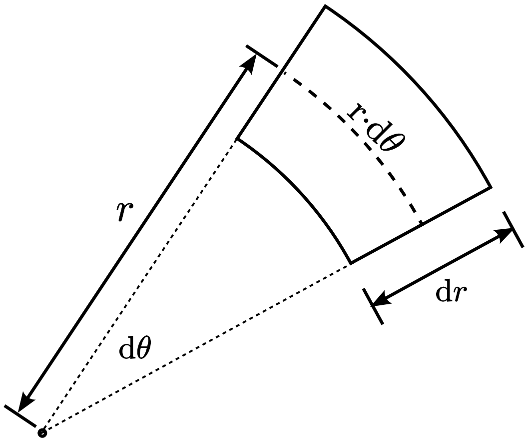

Figure 3.4: An infinitesimal soil element in cylindrical coordinates

rewritten as follows:

$$\begin{aligned} \mathbb{W}_{int} &= \pi \int_{r_i}^{r_o} \delta \underset{\sim}{\varepsilon}^T \underset{\sim}{\sigma}\, r\mathrm{d}r \\ &= \pi \int_{r_i}^{r_o} \delta \underset{\sim}{U}^T \underset{\sim}{B}^T \underset{\sim}{\sigma}\, r\mathrm{d}r \\ &= \pi \delta \underset{\sim}{U}^T \Big(\int_{r_i}^{r_o} \underset{\sim}{B}^T \underset{\sim}{\sigma}\, r\mathrm{d}r \Big) \end{aligned} \tag{3.21}$$

Next, from Equation 3.21, the internal forces, P^{int}, produced by stress in the ring element can be written as:

$$\underset{\sim}{P}^{\mathrm{int}} = \pi \int_{r_i}^{r_o} \underset{\sim}{B}^T \underset{\sim}{\sigma}\, r\mathrm{d}r \tag{3.22}$$

Now, consider the derivative of the internal force

$$\begin{aligned} \mathrm{d}\underset{\sim}{P}^{\mathrm{int}} &= \pi \int_{r_i}^{r_o} \underset{\sim}{B}^T \mathrm{d}\underset{\sim}{\sigma}\, r\mathrm{d}r \\ &= \pi \int_{r_i}^{r_o} \underset{\sim}{B}^T \underset{\sim}{\mathbf{D}} \mathrm{d}\underset{\sim}{\varepsilon}\, r\mathrm{d}r \\ &= \pi \Big(\int_{r_i}^{r_o} \underset{\sim}{B}^T \underset{\sim}{\mathbf{D}} \underset{\sim}{B}\, r\mathrm{d}r \Big) \mathrm{d}\underset{\sim}{U} \end{aligned} \tag{3.23}$$

Thus, the tangent stiffness matrix of the ring element can be written as follows:

$$\mathbb{K} = \pi \int_{r_i}^{r_o} \underset{\sim}{B}^T \underset{\sim}{\mathbf{D}} \underset{\sim}{B} \, r\mathrm{d}r \tag{3.24}$$

The integration in Equation 3.24 will be evaluated by numerical integration using 2 Gauss-Legendre points.

3.1.2 Material Inelasticity

Soil inelasticity will be simulated by a Von Mises plasticity model. The stress variation in the θ direction is approximated by the elastic displacement variation. Thus, the integration with respect to θ can be carried out as in Equation 3.19 (constant factor π). The soil domain will be separated into two regions on the basis of stress variation with respect to θ, one with $\cos(\theta)$ and the other with $\sin(\theta)$. Considering the waves emanating from the disk, longitudinal waves propagate in the direction $\theta = 0$ while shear waves propagate in the orthogonal direction, $\theta = \pi/2$. The treatment of material nonlinearities will be handled separately in the two regions, as discussed below.

3.1.2.1 Inelastic Treatment for Longitudinal-Wave Region

Yielding in the region corresponding to $\theta = 0$ affects longitudinal-wave propagation. Assuming that the elastic variation with θ is maintained, the trial shear stress intensity, T^{trial}, is given by:

$$T^{\mathrm{trial}} = \sqrt{\sigma_r^2 + \sigma_\theta^2 + \sigma_z^2} \tag{3.25}$$

The modification of the tangent rigidity matrix, $\underset{\sim}{D}$, due to inelasticity will affect at the entries corresponding to σ_r and σ_θ as denoted by the letter L in Equation 3.26:

$$\underset{\sim}{D} = \begin{bmatrix} L_{11} & L_{12} & 0 \\ L_{21} & L_{22} & 0 \\ 0 & 0 & S_{33} \end{bmatrix} \tag{3.26}$$

The matrix $\underset{\sim}{D}$ can be derived as an approximate algorithmic tangent rigidity. First, determine the quantity λ such that

$$\underset{\sim}{D} = \underset{\sim}{D}^{\text{elastic}} - \lambda \underset{\sim}{S}^{\text{trial}} (\underset{\sim}{S}^{\text{trial}})^T \tag{3.27}$$

and

$$\Delta \underset{\sim}{\sigma} = \underset{\sim}{D} \Delta \underset{\sim}{\varepsilon} \tag{3.28}$$

where: $\Delta \underset{\sim}{\sigma}$ is the increment of stress resulting from the strain increment $\Delta \underset{\sim}{\varepsilon}$ by application of a method of integration, e.g. the radial-return method: $\underset{\sim}{S}$ is the deviatoric stress:

Using Equations 3.27 and 3.28, $\underset{\sim}{\sigma} + \Delta \underset{\sim}{\sigma}$ can be written as:

$$\begin{aligned} \underset{\sim}{\sigma} + \Delta \underset{\sim}{\sigma} &= \underset{\sim}{\sigma} + \underset{\sim}{D} \underset{\sim}{\varepsilon} - \lambda \underset{\sim}{S}^{\text{trial}} (\underset{\sim}{S}^{\text{trial}})^T \Delta \underset{\sim}{\varepsilon} && (3.29) \\ &= \underset{\sim}{\sigma}^{\text{trial}} - \lambda \underset{\sim}{S}^{\text{trial}} (\underset{\sim}{S}^{\text{trial}})^T \Delta \underset{\sim}{\varepsilon} && (3.30) \end{aligned}$$

Taking the deviatoric parts of both sides of Equation 3.30, Equation 3.31 is obtained as:

$$\underset{\sim}{S} + \Delta \underset{\sim}{S} = \underset{\sim}{S}^{\text{trial}} - \lambda \underset{\sim}{S}^{\text{trial}} (\underset{\sim}{S}^{\text{trial}})^T \Delta \underset{\sim}{\varepsilon} \tag{3.31}$$

Next, by the radial-return method, in the case of perfect plasticity, $\underset{\sim}{S} + \Delta \underset{\sim}{S}$ is given by:

$$\underset{\sim}{S} + \Delta \underset{\sim}{S} = \left(1 - \frac{3G \Delta \hat{\varepsilon}^P}{\sqrt{3} T^{\text{trial}}} \right) \underset{\sim}{S}^{\text{trial}} \tag{3.32}$$

Finally, setting the right-hand sides of Equations 3.31 and 3.32 equal to each other, the coefficient λ is found from:

$$\frac{3G\Delta\hat{\varepsilon}^P}{\sqrt{3}T^{\text{trial}}} = \lambda(\underset{\sim}{S}^{\text{trial}})^T \Delta\underset{\sim}{\varepsilon} \tag{3.33}$$

and, therefore,

$$\lambda = \frac{\frac{3G\Delta\hat{\varepsilon}^P}{\sqrt{3}T^{\text{trial}}}}{(\underset{\sim}{S}^{\text{trial}})^T \Delta\underset{\sim}{\varepsilon}} \tag{3.34}$$

Since the trial deviatoric stress is given by:

$$\underset{\sim}{S}^{\text{trial}} = \begin{bmatrix} S_r^{\text{trial}} & S_\theta^{\text{trial}} & S_z^{\text{trial}} \end{bmatrix}^T \tag{3.35}$$

the tangent rigidity matrix for longitudinal-wave region can be calculated by Equation 3.27:

$$\underset{\sim}{D}^L = \begin{bmatrix} D_{11}^L & D_{12}^L & D_{13}^L \\ D_{21}^L & D_{22}^L & D_{23}^L \\ D_{31}^L & D_{32}^L & D_{33}^L \end{bmatrix} \tag{3.36}$$

with entries given by:

$$L_{11} = D_{11}^L \quad , \quad L_{12} = D_{12}^L \tag{3.37}$$

$$L_{21} = D_{21}^L \quad , \quad L_{22} = D_{22}^L \tag{3.38}$$

3.1.2.2 Inelastic Treatment for Shear-Wave Region

Yielding in the region corresponding to $\theta = \pi/2$ is produced exclusively by $\tau_{r\theta}$. The S entry in Equation 3.26 is affected by shear yielding and the trial shear stress intensity is given by:

$$T^{\text{trial}} = \sqrt{\tau_{r\theta}^2 + \tau_{\theta r}^2} \tag{3.39}$$

$$= 2 \cdot \sqrt{\tau_{r\theta}^2} \tag{3.40}$$

with the trial deviatoric stress

$$\underset{\sim}{S}^{\text{trial}} = \left[S_{r\theta}^{\text{trial}}\right]^T \tag{3.41}$$

The tangent rigidity matrix for the shear-wave region can be determined using Equation 3.27:

$$\underset{\sim}{D}^L = \left[D_{11}^L\right] \tag{3.42}$$

Finally,

$$S_{33} = D_{11}^L \tag{3.43}$$

3.1.3 Mass Matrix

The mass of an infinitesimal soil element (see Figure 3.4) is:

$$\rho \cdot \Delta z \left(\mathrm{d}r \cdot (r\mathrm{d}\theta)\right) \tag{3.44}$$

where Δz is the thickness of the soil slice. Therefore, the consistent mass matrix for the ring element can be calculated as:

$$\begin{aligned}\underset{\sim}{\mathbb{M}} &= \Delta z \cdot \int_{r_i}^{r_o} \int_{2\pi}^{0} \rho \cdot r(\underset{\sim}{\Phi}^T \underset{\sim}{\Phi})\, \mathrm{d}\theta \mathrm{d}r \\ &= \rho \cdot \pi \cdot \Delta z \cdot \Delta r \int_{1}^{-1} r(\zeta)(\underset{\sim}{\Phi}^T \underset{\sim}{\Phi})\mathrm{d}\zeta \end{aligned} \tag{3.45}$$

where

$$\underset{\sim}{N} = \begin{bmatrix} N_1 & 0 & N_2 & 0 \\ 0 & N_1 & 0 & N_2 \end{bmatrix} \tag{3.46}$$

Furthermore, r can be written as a function of the local coordinate, ζ:

$$r(\zeta) = r_i + \frac{\Delta z}{2}(\zeta + 1) \tag{3.47}$$

where Δr is the thickness of the ring $(r_o - r_i)$.

Finally, the mass matrix can be expressed as

$$\mathbb{M} = \frac{\rho \Delta r \Delta z \pi}{6} \begin{bmatrix} 2r_i + \dfrac{\Delta r}{2} & 0 & r_i + \dfrac{\Delta r}{2} & 0 \\ 0 & 2r_i + \dfrac{\Delta r}{2} & 0 & r_i + \dfrac{\Delta r}{2} \\ r_i + \dfrac{\Delta r}{2} & 0 & 2r_i + \dfrac{3\Delta r}{2} & 0 \\ 0 & r_i + \dfrac{\Delta r}{2} & 0 & 2r_i + \dfrac{3\Delta r}{2} \end{bmatrix} \tag{3.48}$$

3.1.4 Equation of Motion and Time Integration Scheme

Time integration is performed by the Newmark constant-average acceleration scheme. The constant acceleration over a time step, a, is taken as the average of the accelerations at the beginning and end of step n. The displacement increment over the step, $\Delta \underset{\sim}{U}$, will be computed.

Denoting the time step by Δt, the velocity at the beginning of the step by $\underset{\sim}{\dot{U}}^{(n)}$ and the acceleration at the beginning and end of the step by $\underset{\sim}{\ddot{U}}^{(n)}$ and $\underset{\sim}{\ddot{U}}^{(n+1)}$, the displacement increment can be approximated as:

$$\Delta \underset{\sim}{U} = \underset{\sim}{\dot{U}}^{(n)} \Delta t + \frac{1}{2} \underset{\sim}{a} t^2 \tag{3.49}$$

with

$$a = \frac{1}{2} (\underset{\sim}{\ddot{U}}^{(n)} + \underset{\sim}{\ddot{U}}^{(n+1)}) \tag{3.50}$$

Next, insert the expression for the average acceleration, a, into Equation 3.49 and the acceleration at the end of the step $n + 1$ can be expressed in Equation

3.51 as follows:

$$\begin{aligned}
\Delta\underset{\sim}{U} &= \underset{\sim}{\dot{U}}^{(n)}\Delta t + \frac{1}{2}\left[\frac{1}{2}(\underset{\sim}{\ddot{U}}^{(n)} + \underset{\sim}{\ddot{U}}^{(n+1)})\right]\Delta t^2 \\
\frac{4}{\Delta t^2}\Delta\underset{\sim}{U} &= \frac{4}{\Delta t}\underset{\sim}{\dot{U}}^{(n)} + \underset{\sim}{\ddot{U}}^{(n)} + \underset{\sim}{\ddot{U}}^{(n+1)} \\
\underset{\sim}{\ddot{U}}^{(n+1)} &= \frac{4}{\Delta t^2}\Delta\underset{\sim}{U} - \frac{4}{\Delta t}\underset{\sim}{\dot{U}}^{(n)} - \underset{\sim}{\ddot{U}}^{(n)}
\end{aligned} \tag{3.51}$$

The velocity at the end of the step can be written as:

$$\begin{aligned}
\underset{\sim}{\dot{U}}^{(n+1)} &= \underset{\sim}{\dot{U}}^{(n)} + a\Delta t \\
&= \underset{\sim}{\dot{U}}^{(n)} + \frac{1}{2}(\underset{\sim}{\ddot{U}}^{(n)} + \underset{\sim}{\ddot{U}}^{(n+1)})\Delta t
\end{aligned} \tag{3.52}$$

Substituting the expression for $\underset{\sim}{\ddot{U}}^{(n+1)}$ from Equation 3.51 into Equation 3.52, the velocity, $\underset{\sim}{\dot{U}}^{(n+1)}$, at the end of the step and can be expressed in terms of information exclusively from the n-th step as follows:

$$\begin{aligned}
\underset{\sim}{\dot{U}}^{(n+1)} &= \underset{\sim}{\dot{U}}^{(n)} + \frac{1}{2}\underset{\sim}{\ddot{U}}^{(n)}\Delta t + \frac{1}{2}\left(\frac{4}{\Delta t^2}\Delta\underset{\sim}{U} - \frac{4}{\Delta t}\underset{\sim}{\dot{U}}^{(n)} - \underset{\sim}{\ddot{U}}^{(n)}\right)\Delta t \\
&= \frac{2}{\Delta t}\Delta\underset{\sim}{U} - \underset{\sim}{\dot{U}}^{(n)}
\end{aligned} \tag{3.53}$$

Next, consider the equation of motion at the end of the step:

$$\underset{\sim}{\mathbb{M}}\underset{\sim}{\ddot{U}}^{(n+1)} + \underset{\sim}{\mathbb{C}}\underset{\sim}{\dot{U}}^{(n+1)} + \underset{\sim}{P}^{\text{int}(n+1)} = \underset{\sim}{\mathbb{P}}^{(n+1)} \tag{3.54}$$

and substitute the expressions for $\underset{\sim}{\dot{U}}_{n+1}$ and $\underset{\sim}{\ddot{U}}_{n+1}$ into the equation of motion

$$\begin{aligned}
0 &= \left(\frac{4}{\Delta t^2}\right)\underset{\sim}{\mathbb{M}}\Delta\underset{\sim}{U} - \left(\frac{4}{\Delta t}\right)\underset{\sim}{\mathbb{M}}\underset{\sim}{\dot{U}}^{(n)} - \underset{\sim}{\mathbb{M}}\underset{\sim}{\ddot{U}}^{(n)} \\
&\quad + \left(\frac{2}{\Delta t}\right)\underset{\sim}{\mathbb{C}}\Delta\underset{\sim}{U} - \underset{\sim}{\mathbb{C}}\underset{\sim}{\dot{U}}^{(n)} + \underset{\sim}{P}^{\text{int}(n+1)} - \underset{\sim}{\mathbb{P}}^{(n+1)}
\end{aligned} \tag{3.55}$$

Now, let the right-hand-side of Equation 3.55 be the residual denoted by $\mathbb{F}(\Delta \underset{\sim}{U})$

$$\begin{aligned}\mathbb{F}(\Delta \underset{\sim}{U}) &= \left(\frac{4}{\Delta t^2}\right)\underset{\sim}{\mathbb{M}}\Delta \underset{\sim}{U} - \left(\frac{4}{\Delta t}\right)\underset{\sim}{\mathbb{M}}\underset{\sim}{\dot{U}}^{(n)} - \underset{\sim}{\mathbb{M}}\underset{\sim}{\ddot{U}}^{(n)} \\ &\quad + \left(\frac{2}{\Delta t}\right)\underset{\sim}{\mathbb{C}}\Delta \underset{\sim}{U} - \underset{\sim}{\mathbb{C}}\underset{\sim}{\dot{U}}^{(n)} + \underset{\sim}{P}^{\mathrm{int}(n+1)} - \underset{\sim}{\mathbb{P}}^{(n+1)} \qquad (3.56)\end{aligned}$$

where $\underset{\sim}{\mathbb{P}}$ is the external load vector. To solve the system of nonlinear equations, a Taylor's series expansion will be applied to the residual of the equation of motion as follows:

$$\mathbb{F}(\Delta \underset{\sim}{U}) = 0 \approx \mathbb{F}(\Delta \underset{\sim}{U_0}) + (\Delta \underset{\sim}{U} - \Delta \underset{\sim}{U_0})\left[\frac{\partial \mathbb{F}(\Delta \underset{\sim}{U})}{\partial \Delta \underset{\sim}{U}}\right]_{\Delta \underset{\sim}{U_0}} \qquad (3.57)$$

where $\Delta \underset{\sim}{U_0}$ is the initial estimate of the displacement increment, normally taken as $\underset{\sim}{0}$. The differentiation of the residual with respect to $\Delta \underset{\sim}{U}$ is given by

$$\frac{\partial \mathbb{F}(\Delta \underset{\sim}{U})}{\partial \Delta \underset{\sim}{U}} = \left(\frac{4}{\Delta t^2}\right)\underset{\sim}{\mathbb{M}} + \left(\frac{2}{\Delta t}\right)\underset{\sim}{\mathbb{C}} + \frac{\partial \underset{\sim}{P}^{\mathrm{int}(n+1)}}{\partial(\Delta \underset{\sim}{U})} \qquad (3.58)$$

Note that $\frac{\partial \underset{\sim}{P}^{\mathrm{int}(n+1)}}{\partial(\Delta \underset{\sim}{U})}$ is the tangent stiffness matrix constructed from the tangent rigidity matrix. Finally, a linear system of equation can be set up for each iteration as follows:

$$\left[\frac{\partial \mathbb{F}(\Delta \underset{\sim}{U})}{\partial \Delta \underset{\sim}{U}}\right]_{\Delta \underset{\sim}{U_0}} (\Delta \underset{\sim}{U} - \Delta \underset{\sim}{U_0}) = -\mathbb{F}(\Delta \underset{\sim}{U_0}) \qquad (3.59)$$

3.1.5 Pile-Soil Element Connectivities

The nodal displacements of the pile, u_z^P, at a particular depth will be set equal to the displacement of the adjacent soil, u_z^S and v_z^S, as shown in

Figure 3.5. The total external force acting on the pile will be denoted by $\mathbb{P}$ and the soil resistance contributed by the longitudinal-wave and shear-wave regions by $\mathbb{L}_z$ and $\mathbb{S}_z$, respectively. These three forces must be in equilibrium:

$$(\mathbb{L}_z + \mathbb{S}_z) = -\mathbb{P}_z \tag{3.60}$$

while

$$u_z^P = u_z^S \tag{3.61}$$

$$u_z^P = v_z^S \tag{3.62}$$

or, in symmetric matrix form,

$$\begin{bmatrix} 0 & 0 & 0 & 1 & 1 \\ 0 & 0 & 0 & -1 & 0 \\ 0 & 0 & 0 & 0 & -1 \\ 1 & -1 & 0 & 0 & 0 \\ 1 & 0 & -1 & 0 & 0 \end{bmatrix} \begin{bmatrix} u_z^P \\ u_z^S \\ v_z^S \\ \mathbb{U}_z \\ \mathbb{V}_z \end{bmatrix} = \begin{bmatrix} -\mathbb{P}_z \\ -\mathbb{U}_z \\ -\mathbb{V}_z \\ 0 \\ 0 \end{bmatrix} \tag{3.63}$$

The system of equations for an equilibrium iteration of nonlinear dynamic analysis can be written as:

$$\mathbf{LHS} \cdot \left(\Delta \underset{\sim}{U} - \Delta \underset{\sim}{U}_0 \right) = -\mathbf{RHS} \tag{3.64}$$

where the left-hand side matrix, **LHS**, is given by

$$\left(\frac{4}{\Delta t^2} \right) \underset{\sim}{\mathbb{M}} + \frac{\partial \underset{\sim}{P}^{\mathrm{int}(n+1)}}{\partial (\Delta \underset{\sim}{U})} \tag{3.65}$$

and the right-hand side matrix, **RHS**, is given by:

$$\left(\frac{4}{\Delta t^2} \right) \underset{\sim}{\mathbb{M}} \Delta \underset{\sim}{U} - \left(\frac{4}{\Delta t} \right) \underset{\sim}{\mathbb{M}} \underset{\sim}{\dot{U}}^{(n)} - \underset{\sim}{\mathbb{M}} \underset{\sim}{\ddot{U}}^{(n)} + \underset{\sim}{P}^{\mathrm{int}(n+1)} - \underset{\sim}{\mathbb{P}}^{(n+1)} \tag{3.66}$$

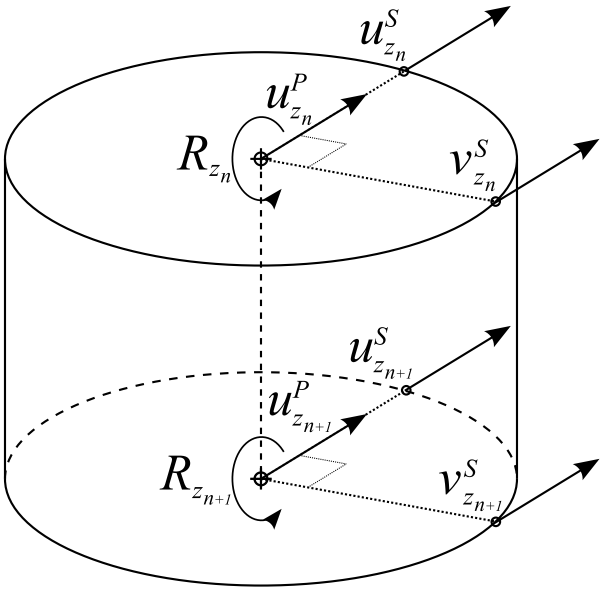

Figure 3.5: Soil-pile displacements coupling

The constraints of Equation 3.63 can be introduced by augmenting the system of equations as follows:

$$\begin{aligned}
\mathrm{LHS}_{u^P} \cdot (\Delta U - \Delta U_0)_{u^P} + \mathbb{L}_z + \$_z &= \mathrm{RHS}^*_{u^P} \\
\mathrm{LHS}_{u^S} \cdot (\Delta U - \Delta U_0)_{u^S} - \mathbb{L}_z &= \mathrm{RHS}^*_{u^S} \\
\mathrm{LHS}_{v^S} \cdot (\Delta U - \Delta U_0)_{v^S} - \$_z &= \mathrm{RHS}^*_{v^S} \\
u^P_z - u^S_z &= 0 \\
u^P_z - v^S_z &= 0
\end{aligned} \tag{3.67}$$

The revised right-hand side, $\mathbf{RHS}^*$, is given by

$$\left(\frac{4}{\Delta t^2}\right) \underset{\sim}{\mathbb{M}} \Delta \underset{\sim}{U} - \left(\frac{4}{\Delta t}\right) \underset{\sim}{\mathbb{M}} \underset{\sim}{\dot{U}}^{(n)} - \underset{\sim}{\mathbb{M}} \underset{\sim}{\ddot{U}}^{(n)} + \underset{\sim}{P}^{\mathrm{int}(n+1)} \tag{3.68}$$

3.2 Results

The performance of the 1D-2DOF ring element will be examined differently for the elastic and inelastic cases. The results from elastic analysis of a harmonically vibrating disk will be compared with the available exact solution by Novak et al (1978). Since the exact solution is not available for transient dynamic analysis or inelasticity, the comparison will be made with the reference solution from the 2-D plane strain FE model from Chapter 2.

3.2.1 Elastic Harmonically Vibrating Disk

The dimensionless force response from FE model with 1D-2DOF ring element for particular excitation frequencies will be plotted versus time in comparison with the theoretical response by Novak et al (1978). Dimensionless frequencies from 0.1 to 1.3 will be considered. The theoretical dimensionless force amplitude and the variation with respect to time are given by

$$P(t) = \left(U \cdot G\sqrt{S_{u1}^2 + S_{u2}^2}\right) \cdot \sin(\omega t + \arctan\left(\frac{S_{u2}}{S_{u1}}\right)) \tag{3.69}$$

where U is the amplitude of excitation: G is the soil shear modulus.

Now, the responses from 1D-2DOF FE analysis and the theoretical solution, denoted by solid and dashed line respectively, are shown in Figures 3.6 to 3.12. Excellent agreement in terms of both amplitude and phase of the dimensionless force can be observed.

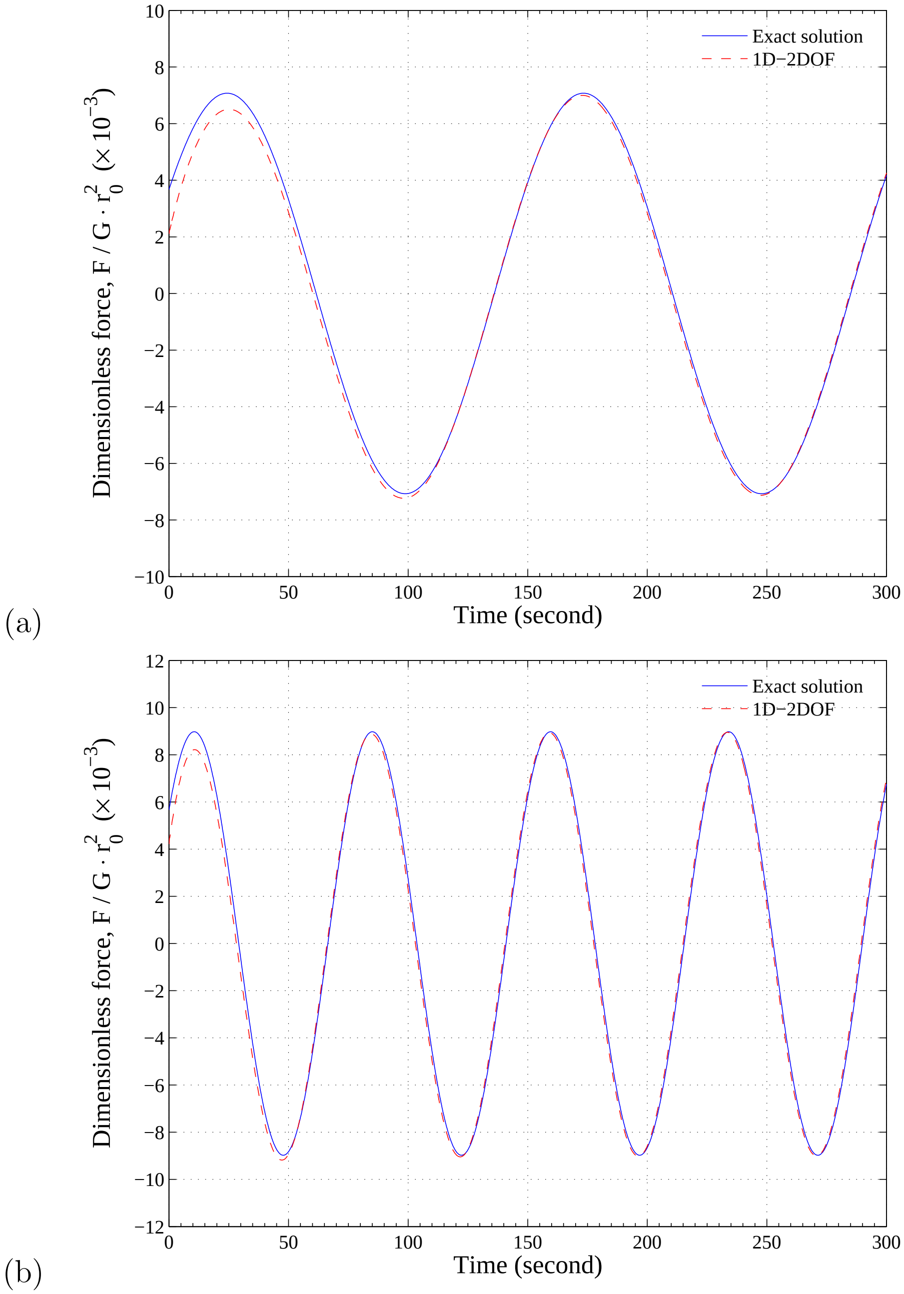

Figure 3.6: Dimensionless force versus time: (a) $a_0 = 0.1$ (b) $a_0 = 0.2$. ($a_0 = \omega \cdot r_0/c_s$)

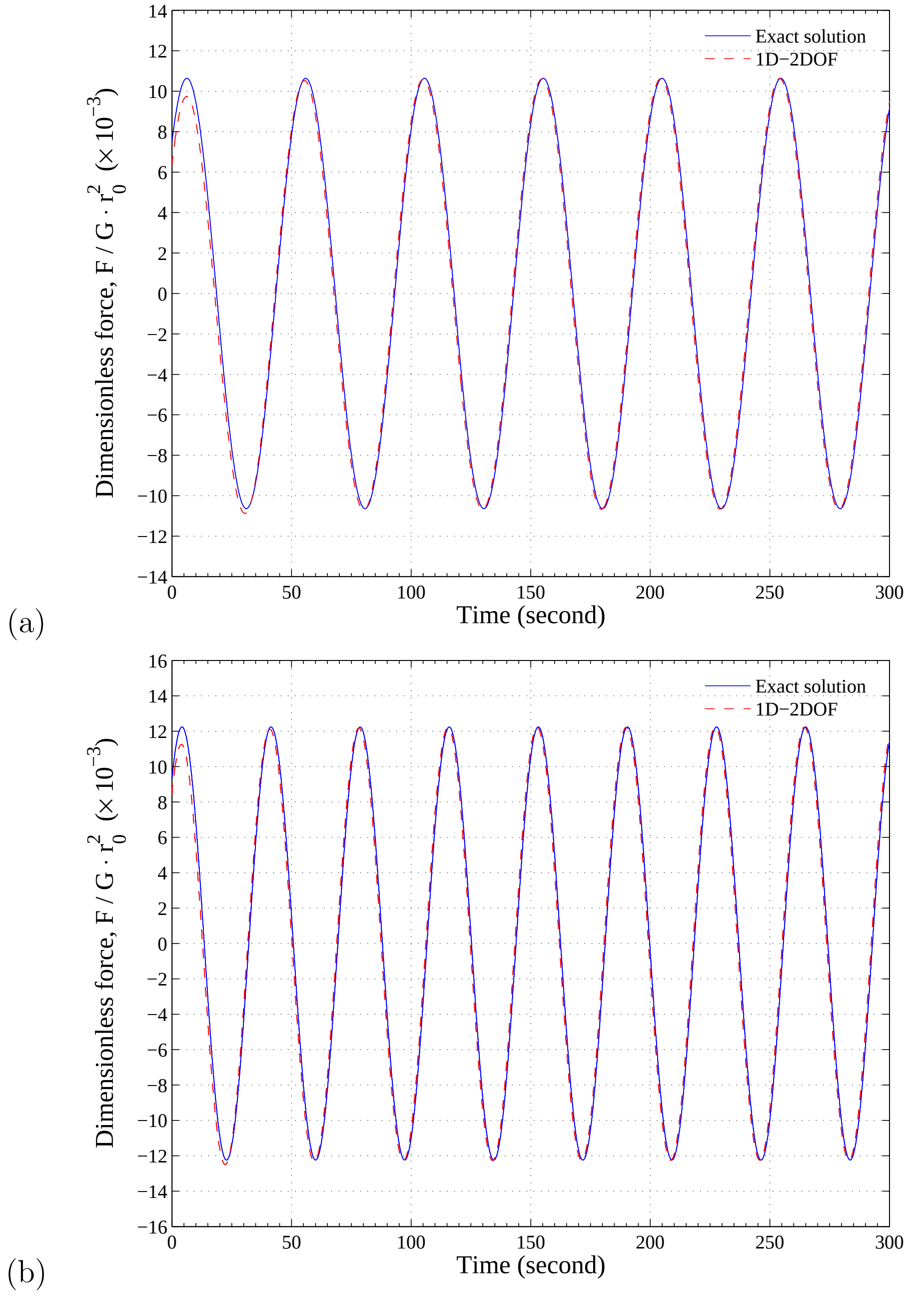

Figure 3.7: Dimensionless force versus time: (a) $a_0 = 0.3$ (b) $a_0 = 0.4$. ($a_0 = \omega \cdot r_0/c_s$)

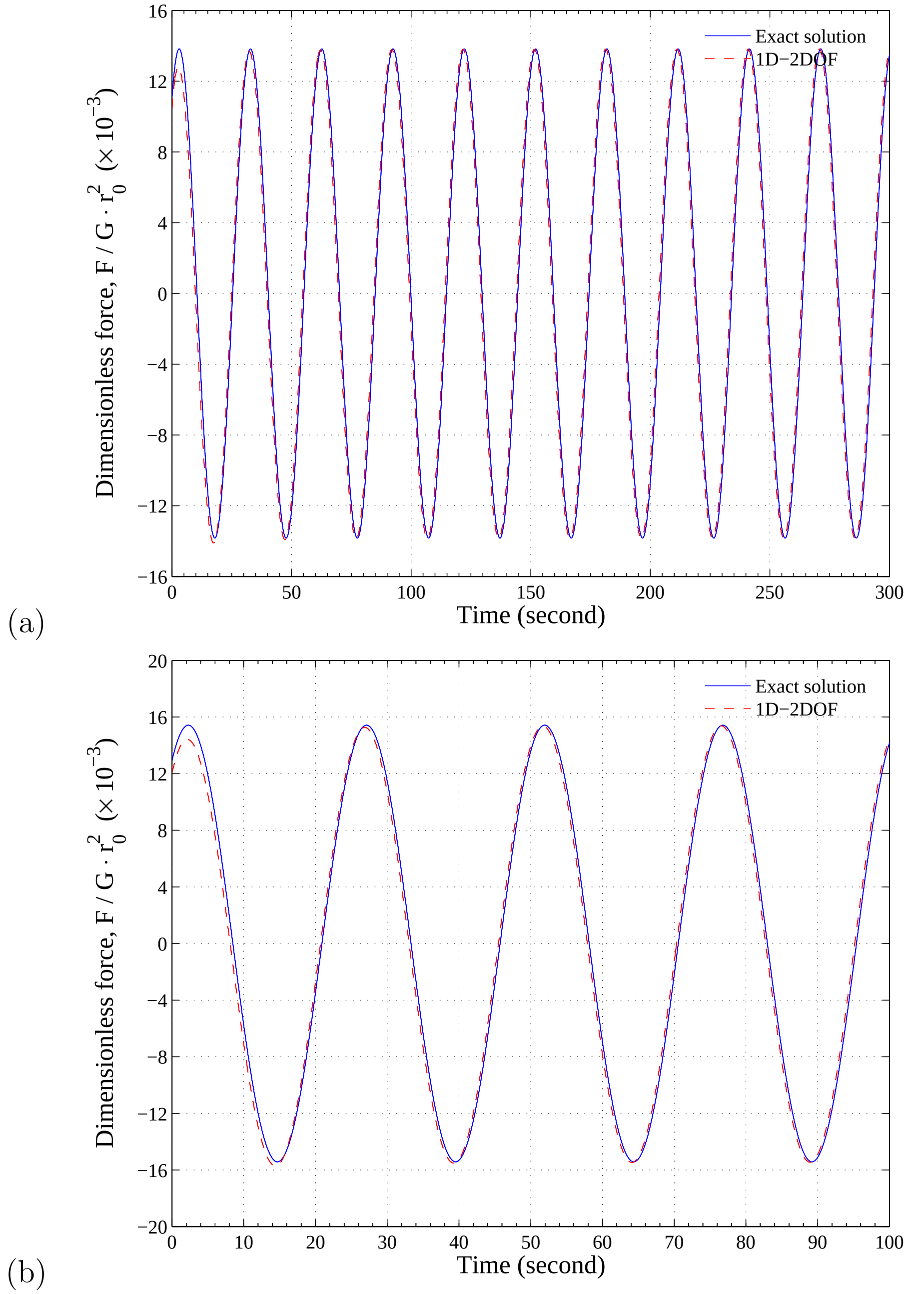

Figure 3.8: Dimensionless force versus time: (a) $a_0 = 0.5$ (b) $a_0 = 0.6$. ($a_0 = \omega \cdot r_0/c_s$)

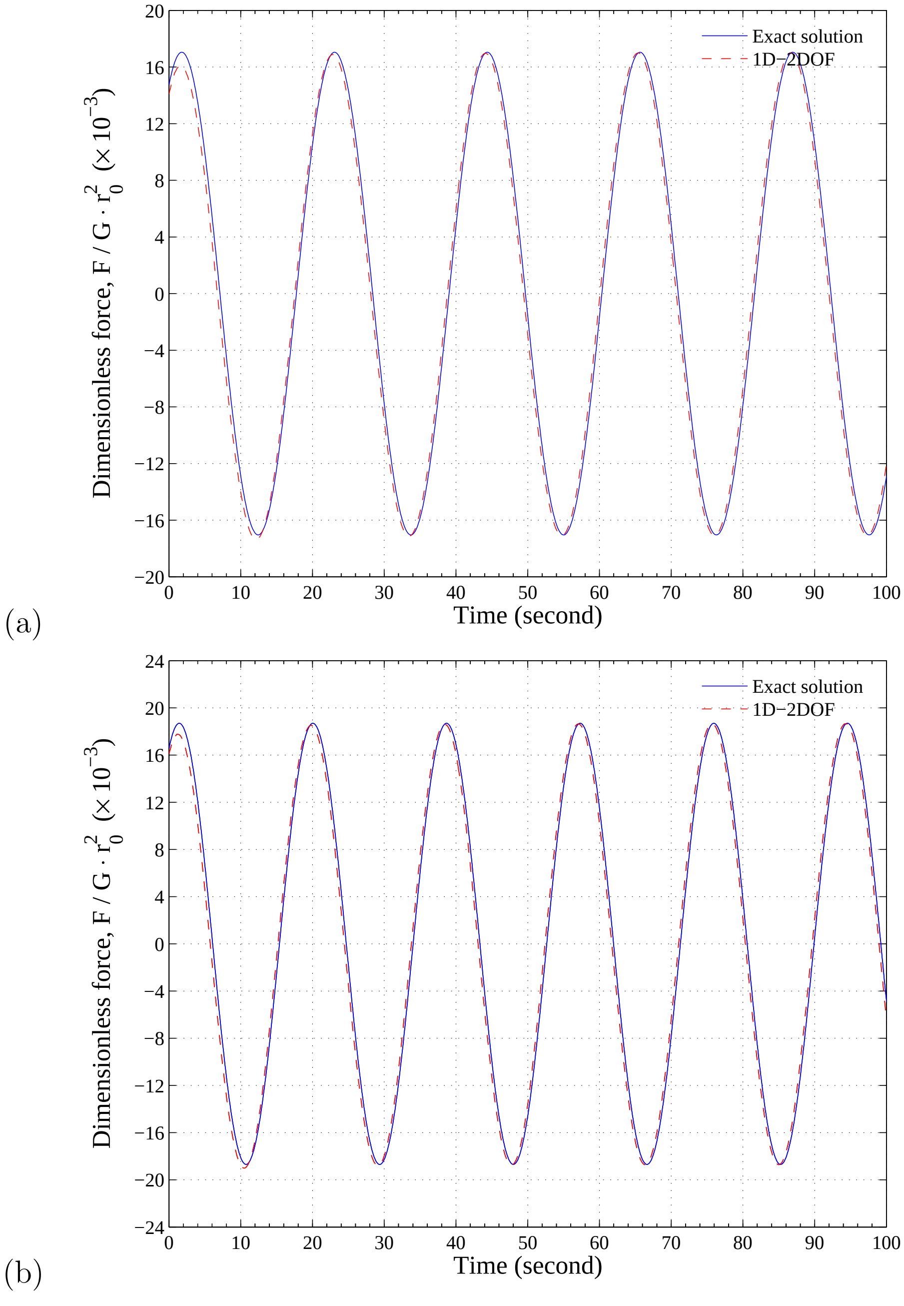

Figure 3.9: Dimensionless force versus time: (a) $a_0 = 0.7$ (b) $a_0 = 0.8$. ($a_0 = \omega \cdot r_0/c_s$)

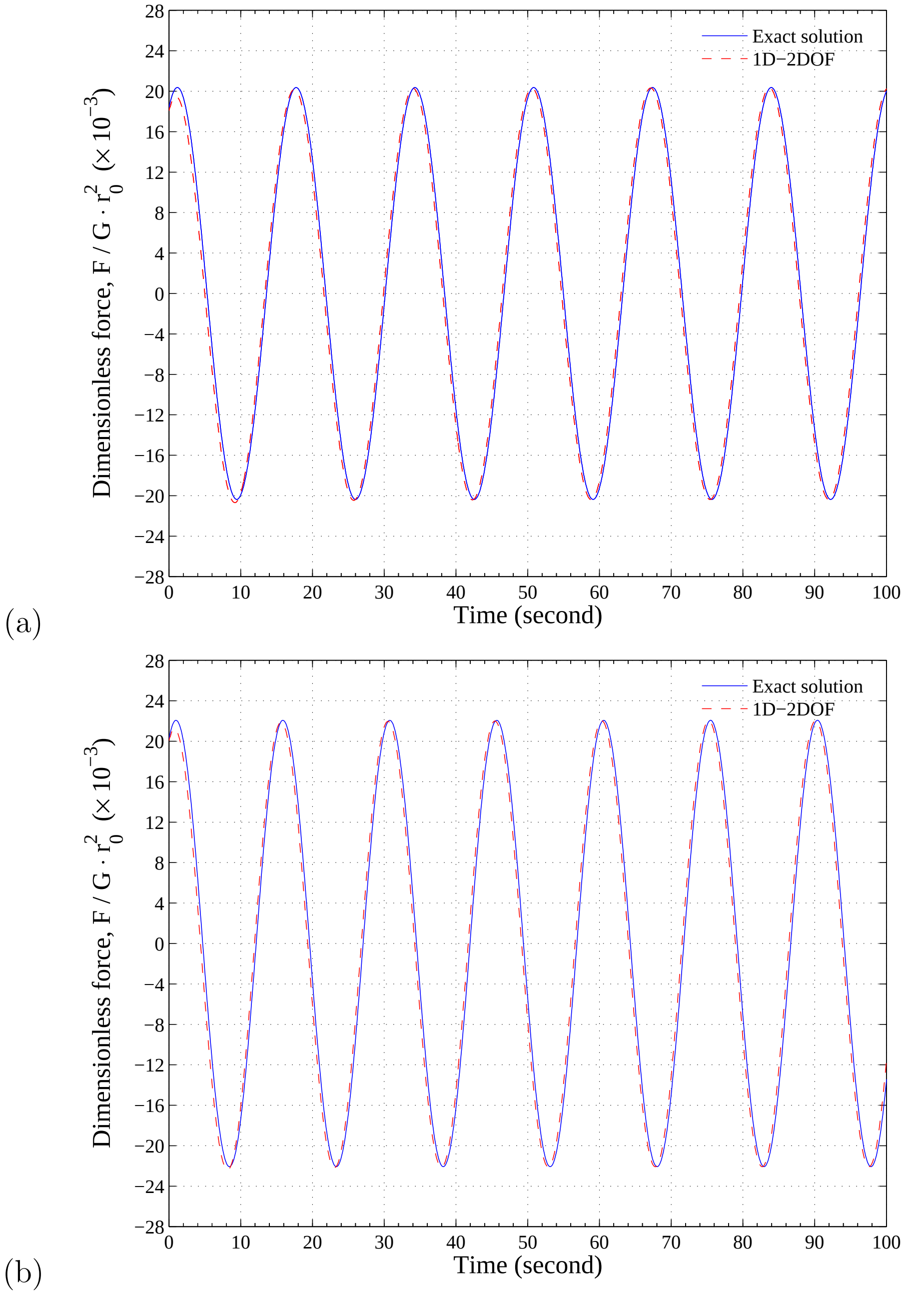

Figure 3.10: Dimensionless force versus time: (a) $a_0 = 0.9$ (b) $a_0 = 1.0$. ($a_0 = \omega \cdot r_0/c_s$)

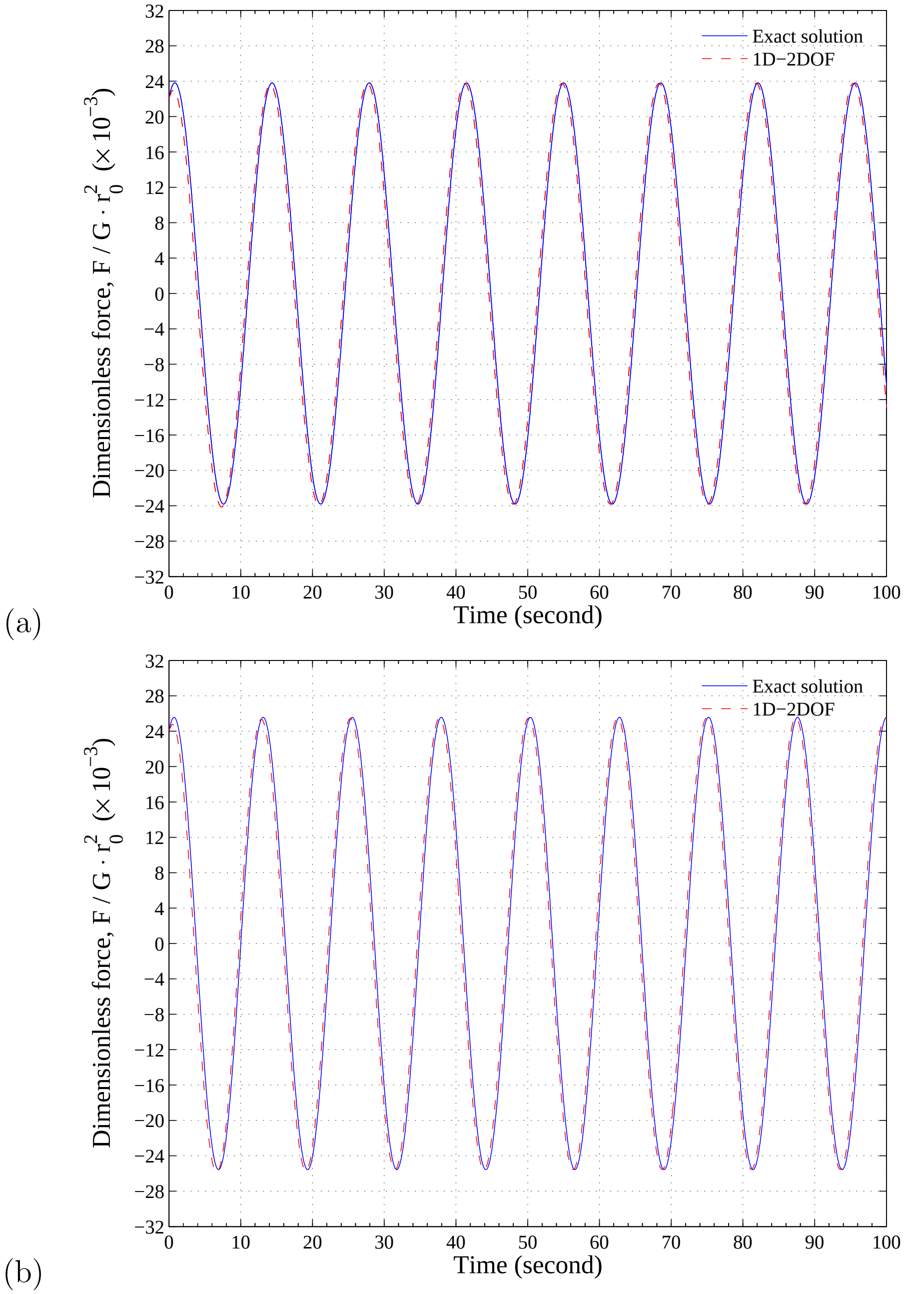

Figure 3.11: Dimensionless force versus time: (a) $a_0 = 1.1$ (b) $a_0 = 1.2$. ($a_0 = \omega \cdot r_0 / c_s$)

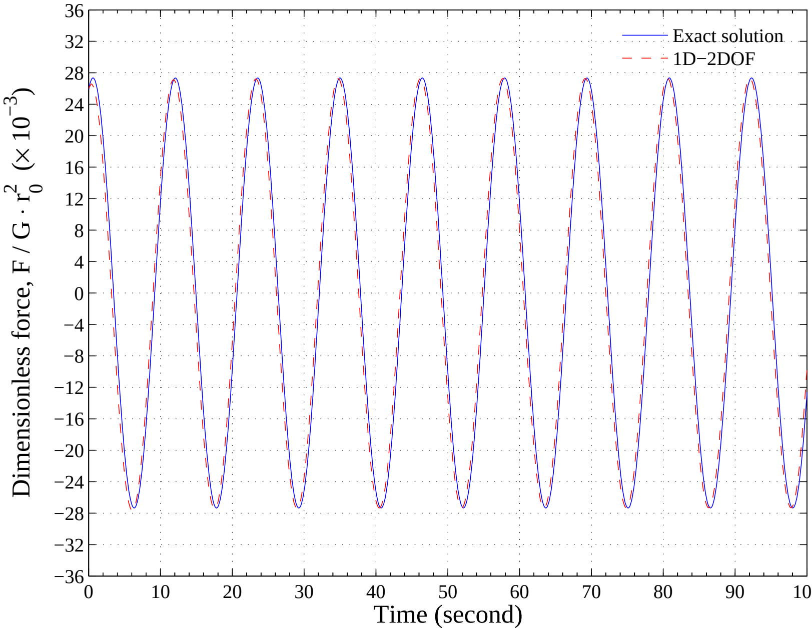

(a)

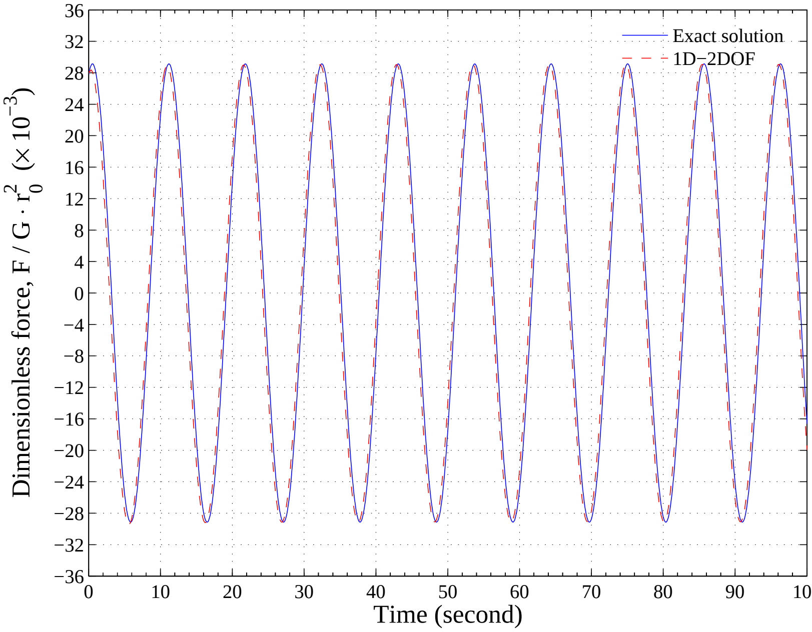

(b)

Figure 3.12: Dimensionless force versus time: (a) $a_0 = 1.3$ (b) $a_0 = 1.4$. ($a_0 = \omega \cdot r_0 / c_s$)

3.2.2 Transient and Inelastic Disk Response

Since the exact solution is available exclusively for elastic soil and harmonically vibrating disk, the numerical solution from 2-D plane-strain FE analysis will be employed as a reference solution for cases involving transient dynamic analysis and inelasticity.

First, the responses from the FE model with the 1D-2DOF ring element, denoted by solid line, to Ricker wavelet displacement excitation, representing transient dynamic analysis, compare very well with the reference solution, represented by dashed line, as shown in Figures 3.13 (a) and (b). The 1-D FE model has been proved clearly to overcome the frequency dependency, problematic in the dynamic spring and dashpot model.

Next, the performance of the 1D-2DOF soil model taking into account soil plasticity will be investigated under two types of displacement excitation, harmonic and Ricker wavelet. Because of the assumed (elastic) displacement variation with respect to azimuthal direction, θ, some error is expected in the computations. However, it will be seen that the error in the dimensionless force amplitude, is less than 15%, and there is no perceptible error in the phase. The dimensionless force versus time plots from the 1D-2DOF model and the 2-D reference model, denoted by solid and dashed lines respectively, are provided in Figures 3.14 to 3.16. The comparison of inelastic behavior of the disk under Ricker wavelet excitation from the reference solution and 1D-2DOF solution are shown in Figures 3.17 (a), (b) and 3.18 (a), (b).

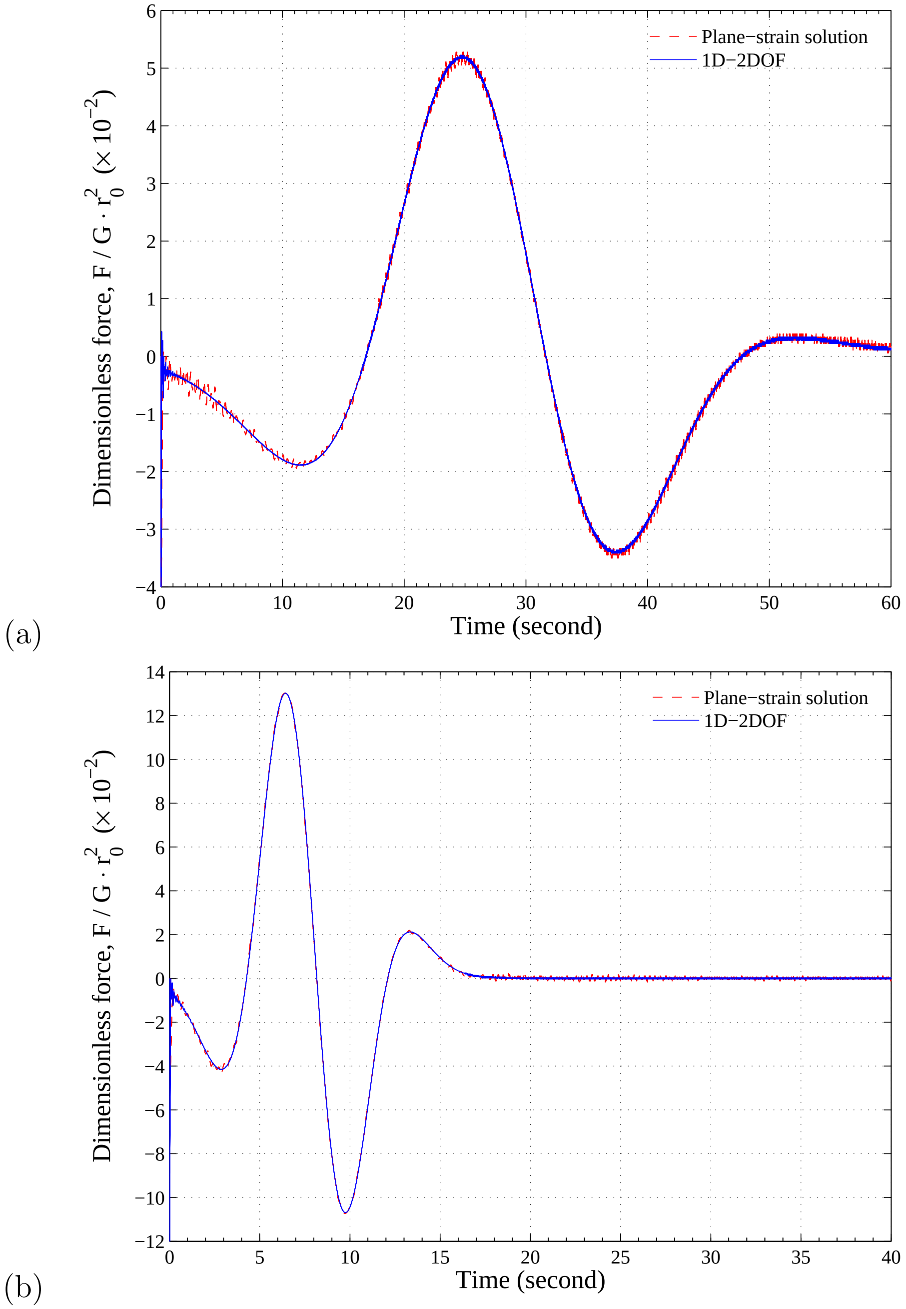

Figure 3.13: Dimensionless force versus time plots for Ricker wavelets with dominant dimensionless frequency: (a) $a_0 = 0.9$ (b) $a_0 = 4.7$. ($a_0 = \omega \cdot r_0 / c_s$)

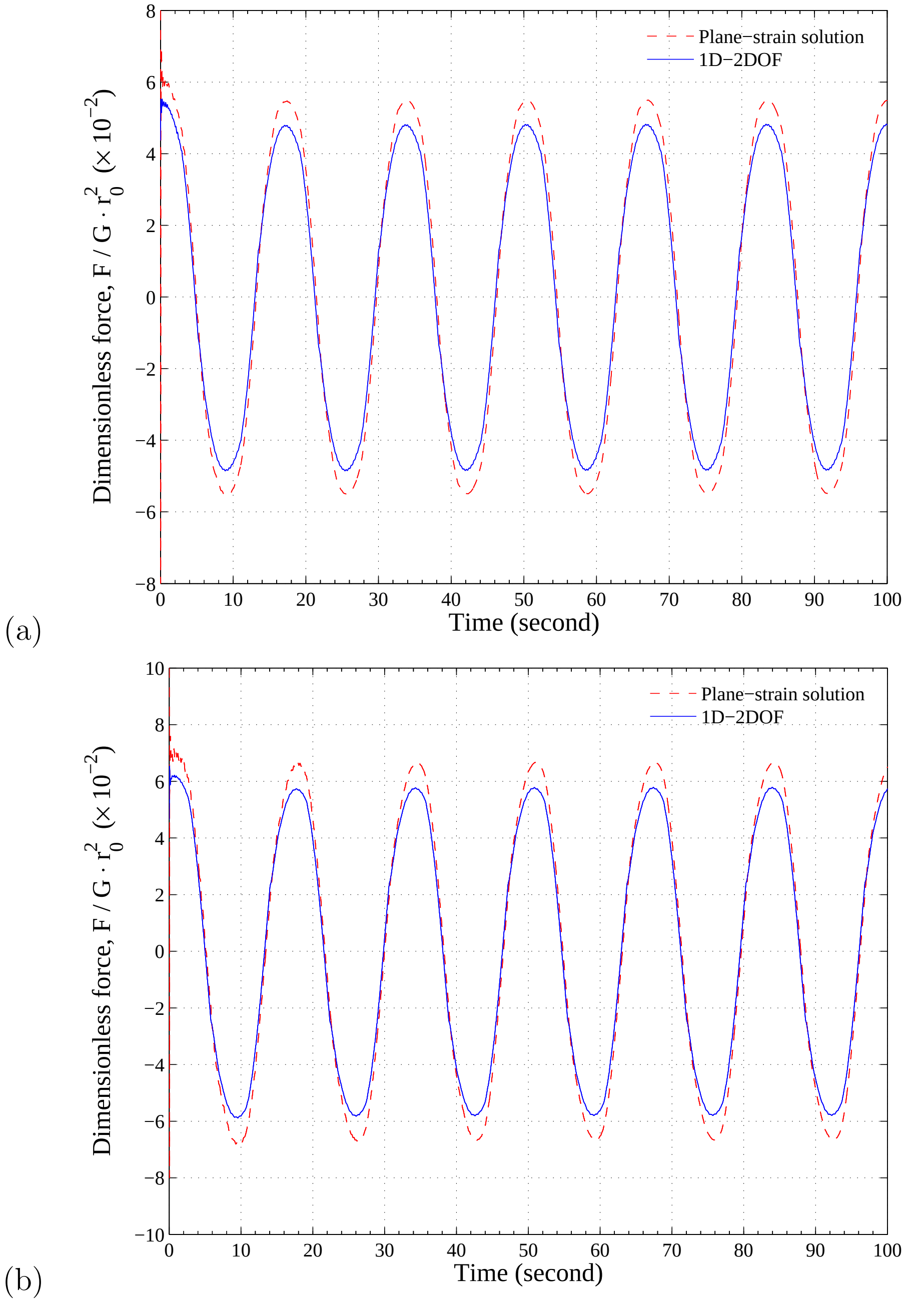

Figure 3.14: Dimensionless force versus time plots for dimensionless frequency $a_0 = 0.9$ ($a_0 = \omega \cdot r_0/c_s$), with yield stress equal to (a) $\sigma_{\text{yield}} = 0.125 \cdot G$ (b) $\sigma_{\text{yield}} = 0.175 \cdot G$.

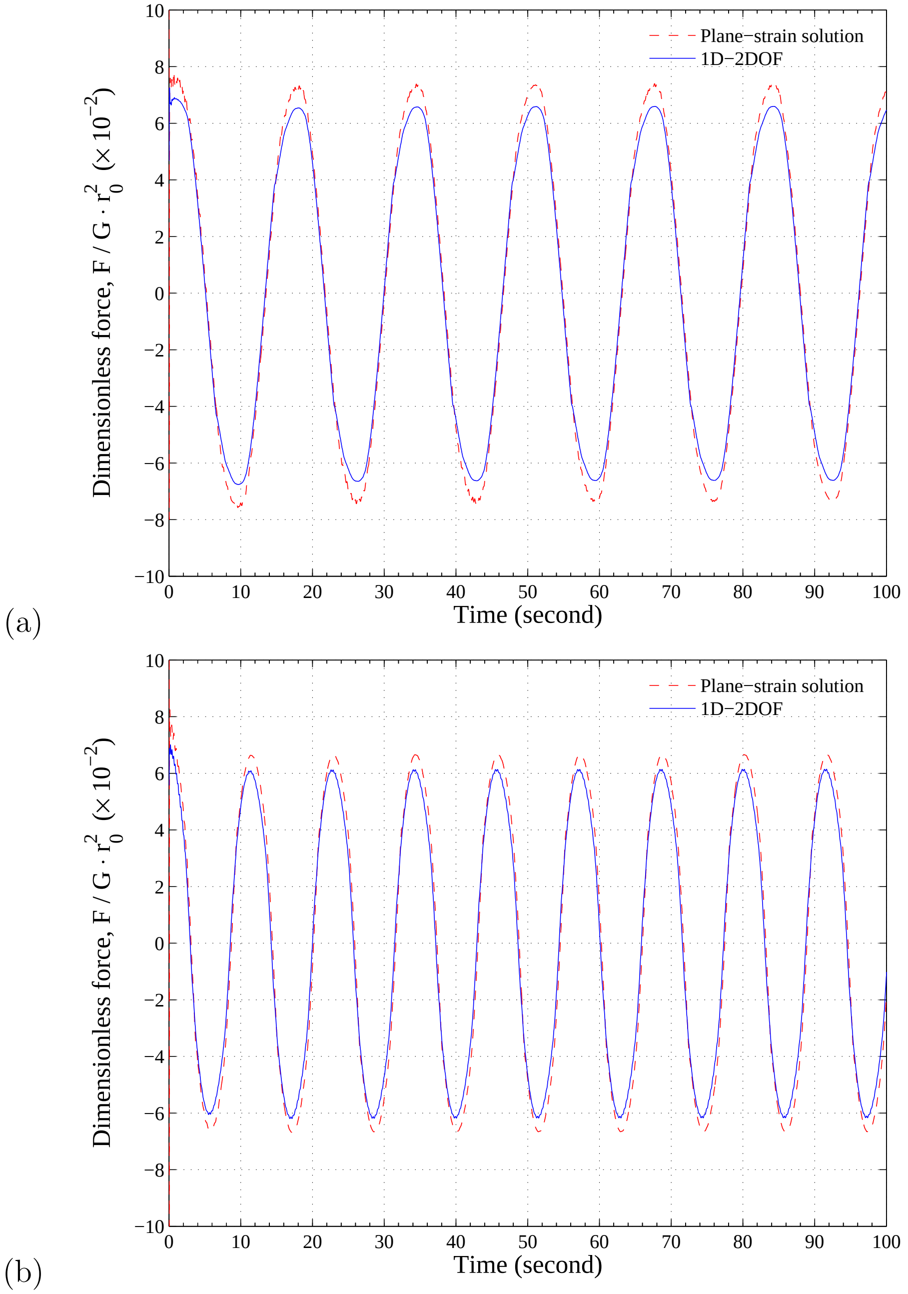

Figure 3.15: Dimensionless force versus time plots for dimensionless frequency (a) $a_0 = 0.9$ (b) 1.3 ($a_0 = \omega \cdot r_0/c_s$), with yield stress equal to (a) $\sigma_{\text{yield}} = 0.225 \cdot G$ (b) $\sigma_{\text{yield}} = 0.125 \cdot G$.

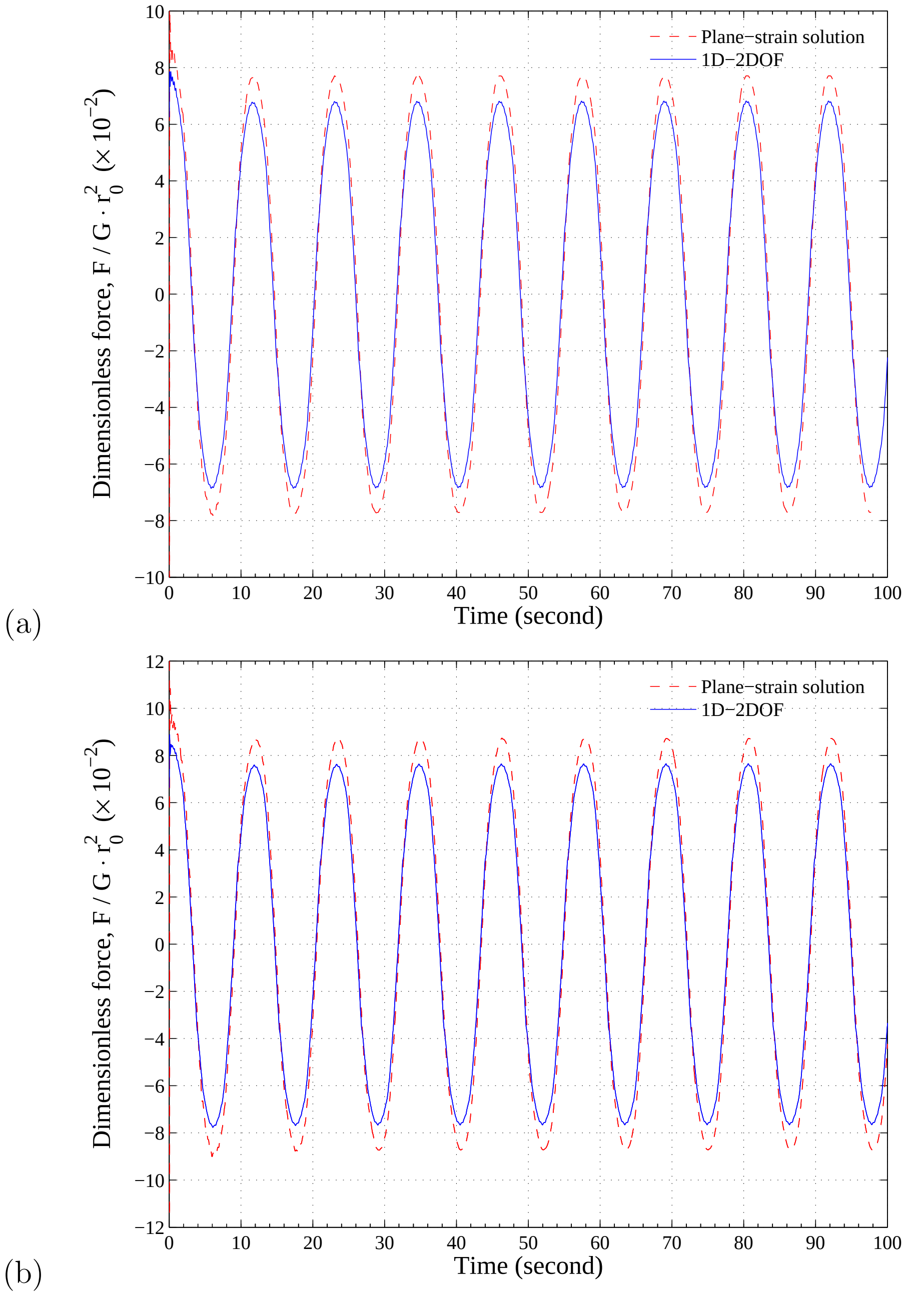

Figure 3.16: Dimensionless force versus time plots for dimensionless frequency $a_0 = 1.3$ ($a_0 = \omega \cdot r_0/c_s$), with yield stress equal to (a) $\sigma_{\text{yield}} = 0.175 \cdot G$ (b) $\sigma_{\text{yield}} = 0.225 \cdot G$.

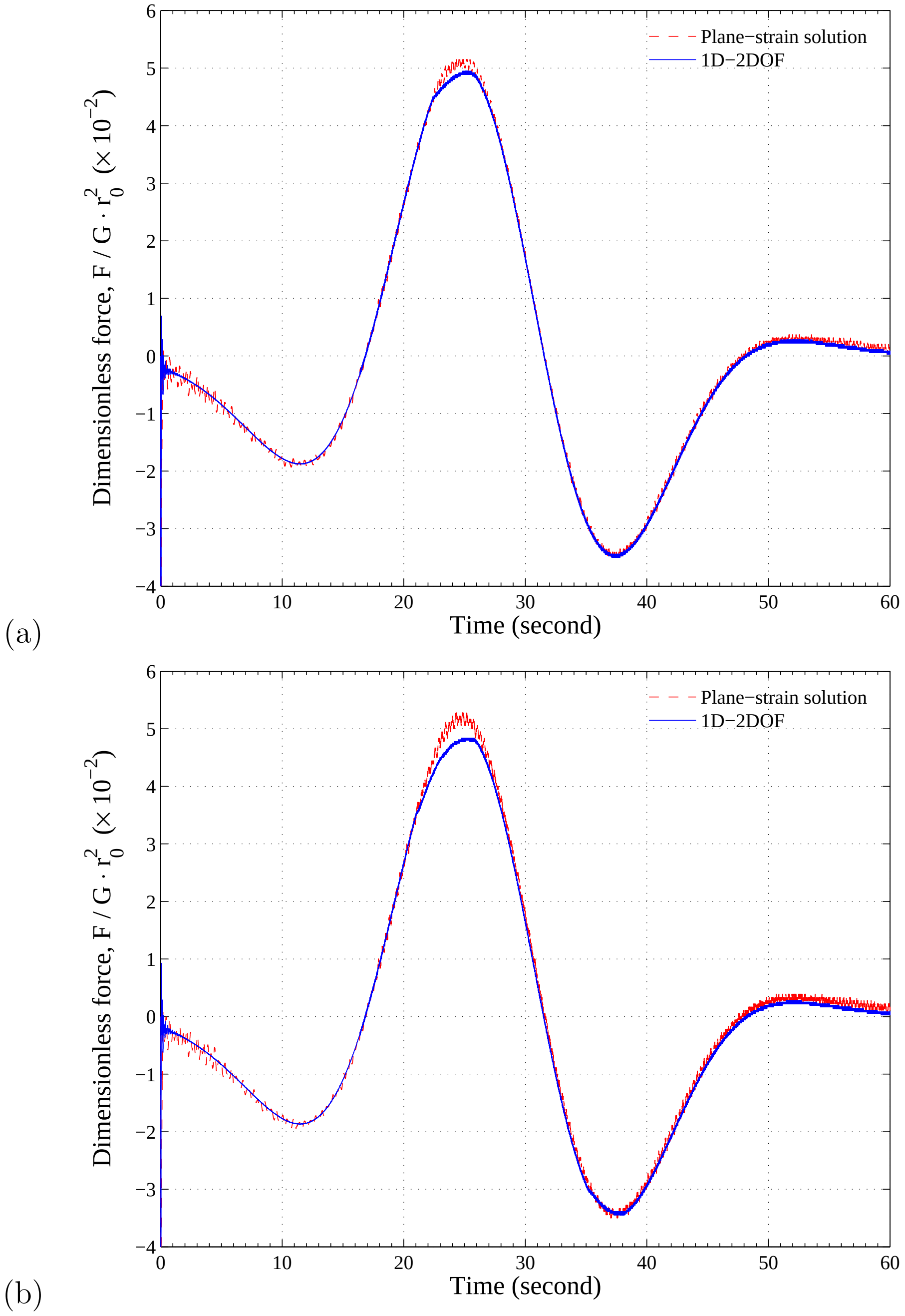

Figure 3.17: Dimensionless force versus time plots for Ricker wavelets with dominant dimensionless frequency $a_0 = 0.9$ ($a_0 = \omega \cdot r_0/c_s$), and yield stress equal to (a) $\sigma_{\text{yield}} = 0.175 \cdot G$ (b) $\sigma_{\text{yield}} = 0.225 \cdot G$.

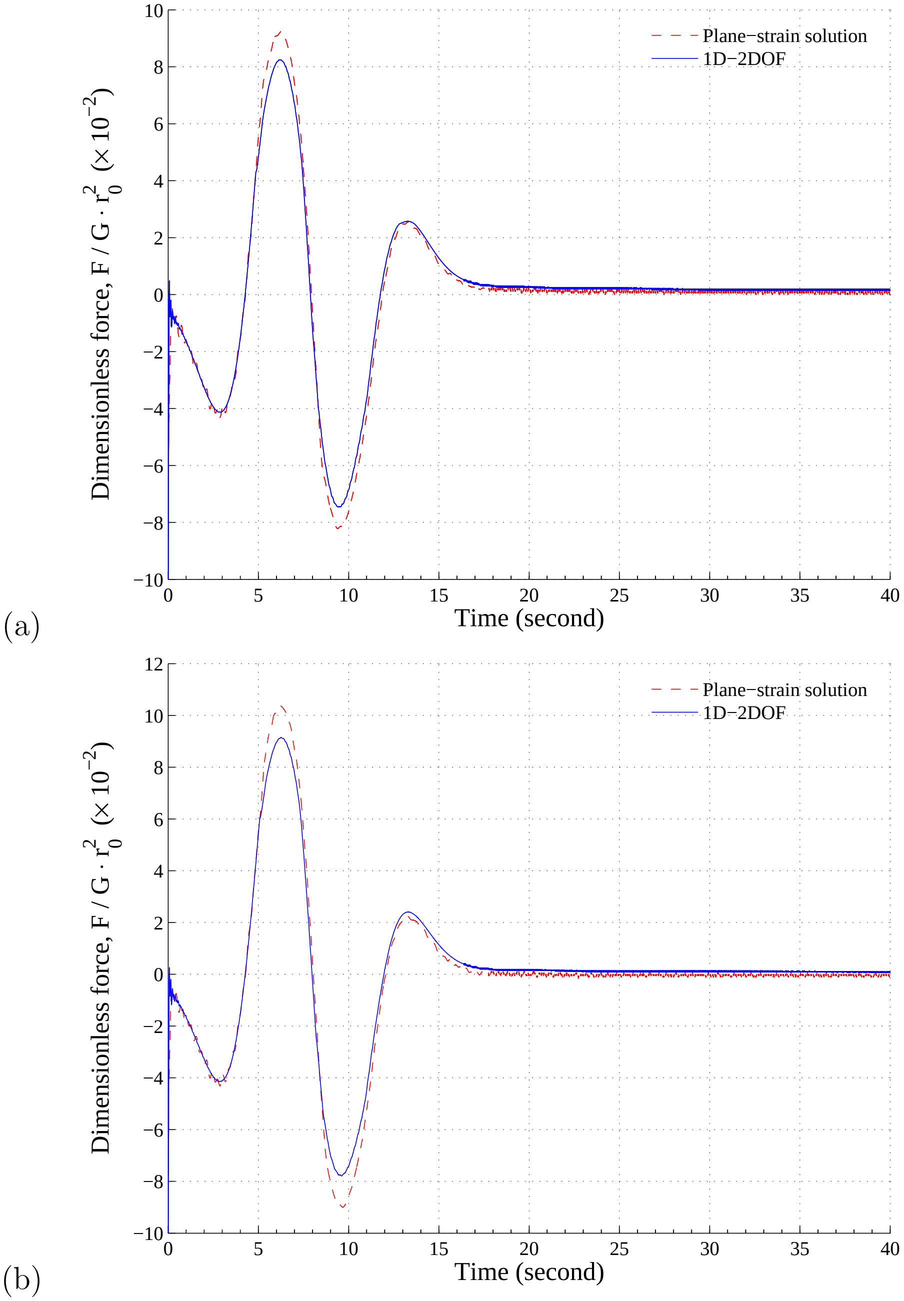

Figure 3.18: Dimensionless force versus time plots for Ricker wavelets with dominant dimensionless frequency $a_0 = 4.7$ ($a_0 = \omega \cdot r_0/c_s$) and yield stress equal to (a) $\sigma_{\text{yield}} = 0.175 \cdot G$ (b) $\sigma_{\text{yield}} = 0.225 \cdot G$.

3.3 Beam with 1D-2DOF Ring Element

A finite-element model of a beam with 1D-2DOF soil elements was constructed for comparison of the computed lateral-pile response with the available experimental data. Euler beam elements are employed as a representation of a pile of which the deflection is linked to the adjacent soil radial and azimuthal displacement corresponding to $\theta = 0$ and $\pi/2$, respectively. The validations of the program is carried out using the exact solution of the harmonically excited Euler beam on elastic springs and dashpots foundation of which the complex stiffness, $k = G(S_{u1} + i \cdot S_{u2})$, is obtained from Novak et al. (1978). The governing differential equation of the Euler beam is given by

$$EI\frac{\partial^4 s(y,t)}{\partial y^4} + k \cdot s(y,t) + \rho A\frac{\partial^2 s(y,t)}{\partial t^2} = 0 \tag{3.70}$$

For harmonic excitation, the displacement $s(y,t)$ can be written as

$$s(y,t) = S(y) \cdot e^{i\omega t} \tag{3.71}$$

Next, substitute the expression of $s(y,t)$ into Equation 3.70:

$$\begin{aligned} EI \cdot e^{i\omega t}\frac{\partial^4 S(y)}{\partial y^4} + S(y)e^{i\omega t}k - \rho A\omega^2 S(y)e^{i\omega t} &= 0 \cdot e^{i\omega t} \\ EI \cdot e^{i\omega t}\left[\frac{\partial^4 S(y)}{\partial y^4} - \left(\frac{\rho A\omega^2 - k}{EI}\right)S(y)\right] &= 0 \end{aligned} \tag{3.72}$$

Now, Equation 3.72 leads to:

$$\frac{\partial^4 S(y)}{\partial y^4} - \beta^4 S(y) = 0 \tag{3.73}$$

where:

$$\beta^4 = \frac{\rho A\omega^2 - k}{EI} \tag{3.74}$$

Then, the solution to Equation 3.74 is given by:

$$S(y) = A\sin(\beta y) + B\cos(\beta y) + C\sinh(\beta y) + D\cosh(\beta y) \tag{3.75}$$

The coefficients A, B, C, and D are to be determined from the boundary conditions at the top and the bottom of the pile:

$$\text{Deflection} \;:\; A\sin(\beta y) + B\cos(\beta y) + C\sinh(\beta y) + D\cosh(\beta y) \tag{3.76}$$

$$\text{Slope} \;:\; A\beta\cos(\beta y) - B\beta\sin(\beta y) + C\beta\cosh(\beta y) + D\beta\sinh(\beta y) \tag{3.77}$$

$$\text{Moment} \;:\; EI\cdot(-A\beta^2\sin(\beta y) - B\beta^2\cos(\beta y) + C\beta^2\sinh(\beta y) + D\beta^2\cosh(\beta y)) \tag{3.78}$$

$$\text{Shear force} \;:\; EI\cdot(-A\beta^3\cos(\beta y) + B\beta^3\sin(\beta y) + C\beta^3\cosh(\beta y) + D\beta^3\sinh(\beta y)) \tag{3.79}$$

The first problem analyzed for the purpose of verification is described as in Figure 3.19. A 7-unit long pile is fully embedded in an isotropic homogeneous soil layer. The pile head displacement and rotation are not constrained while the pile tip is fixed against displacement. The pile has one-unit area and ten-unit second-area-moment-of-inertia. The elastic modulus and density of the pile are 1 unit and 1 unit, respectively. Young's modulus of the soil is 400 unit and Poisson's ratio is 0.25. The soil density is 10 unit. Harmonic force-excitation is applied at the top of the pile with angular frequency of 4 radian/second (equivalent to dimensionless frequency $a_0 = 0.5$) and amplitude of 1-unit force excitation.

The result from the FE code and the exact solution are in excellent

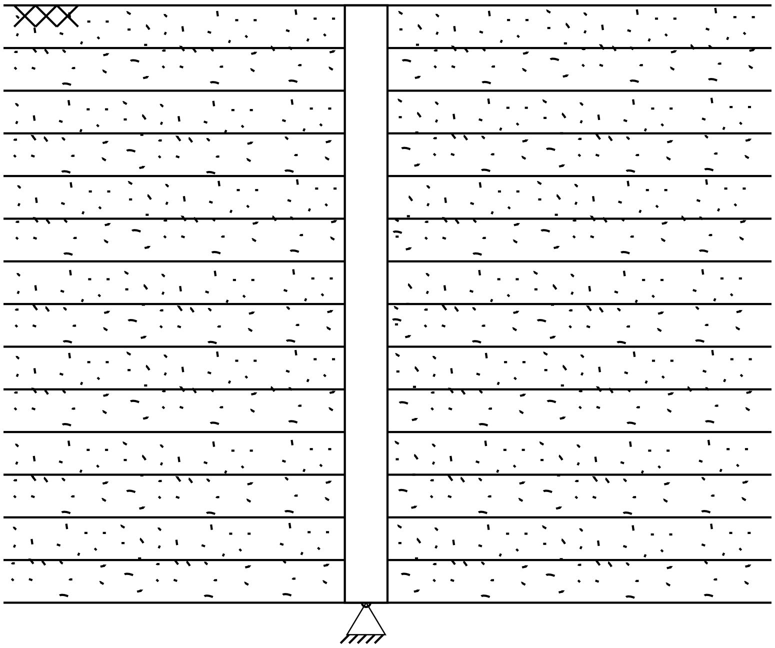

Figure 3.19: A fully embedded pile in a homogeneous soil layer with a pinned-end at the bottom

agreement, as shown in Figure 3.20. The thick solid line represents the displacement amplitude from the exact solution. Hollow circular and triangular markers represent the solution from FE model with 1D-2DOF ring element with 30 layers and 50 layers of the vertical soil domain discretization, respectively.

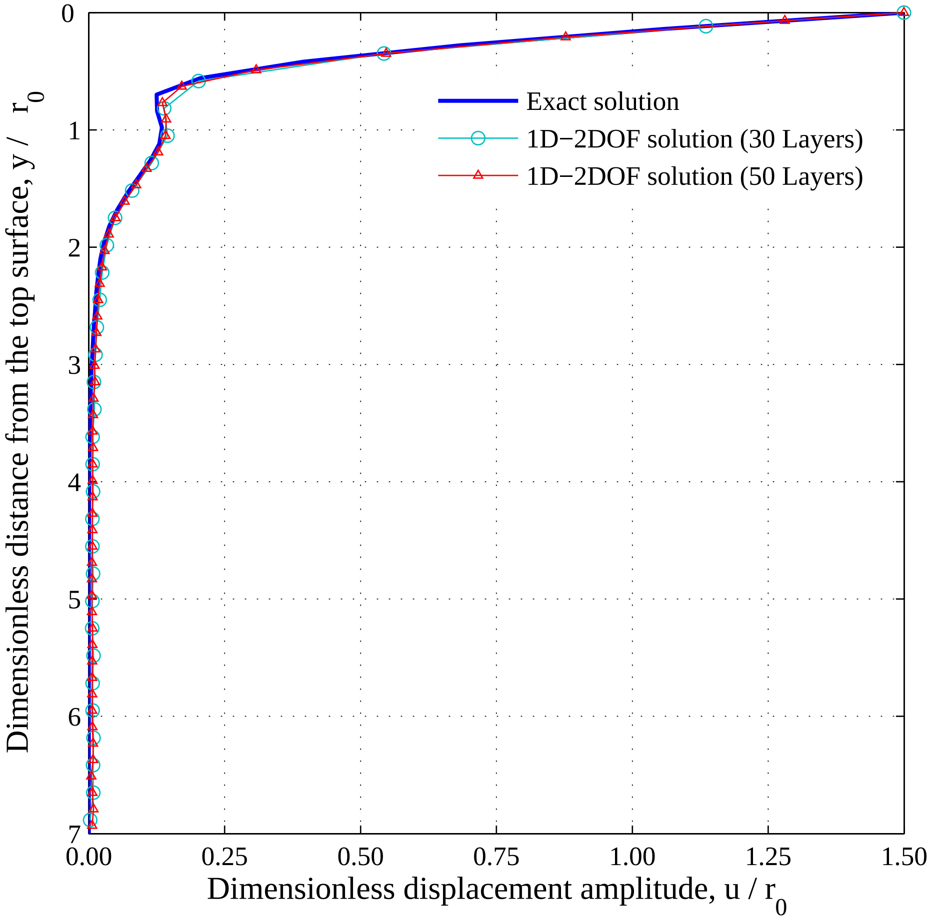

Figure 3.20: The dimensionless displacement amplitude versus dimensionless distance from the top surface of the fixed bottom pile

Another validation of the 1D-2DOF element is carried out in the case of a floating pile (free pile bottom) in a homogeneous soil layer. The pile-head displacement and rotation are not constrained. The soil elastic modulus, Poisson's ratio, and soil density are 2.5, 0.4, and 1.0, respectively while the radius, area, second area-moment-of-inertia, elastic modulus, and density of the pile are 0.5, 1.0, 100, 1.0, and 1.0 respectively. The frequency of excitation is set as 2.0, corresponding to the dimensionless frequency $a_0 = 1.05$, with the force amplitude at the pile head at 1.0.

Now, the results are validated by comparison with the response from the exact solution of the pile embedded in the soil independent slices. However, it should be kept in mind that the actual pile in the 3-D soil domain may behave differently from the exact solution of a Winkler beam with springs and dashpots with coefficients determined from soil-slices model. The performance of the pile model with 1D-2DOF soil element will next be evaluated against actual field experimental data. A well-documented experimental work on a laterally loaded pile was conducted and reported by El-Marsafawi et al (1992). The test set-up is described in Figure 3.22 and the soil shear-wave velocity and density profiles are given in Figure 3.23.

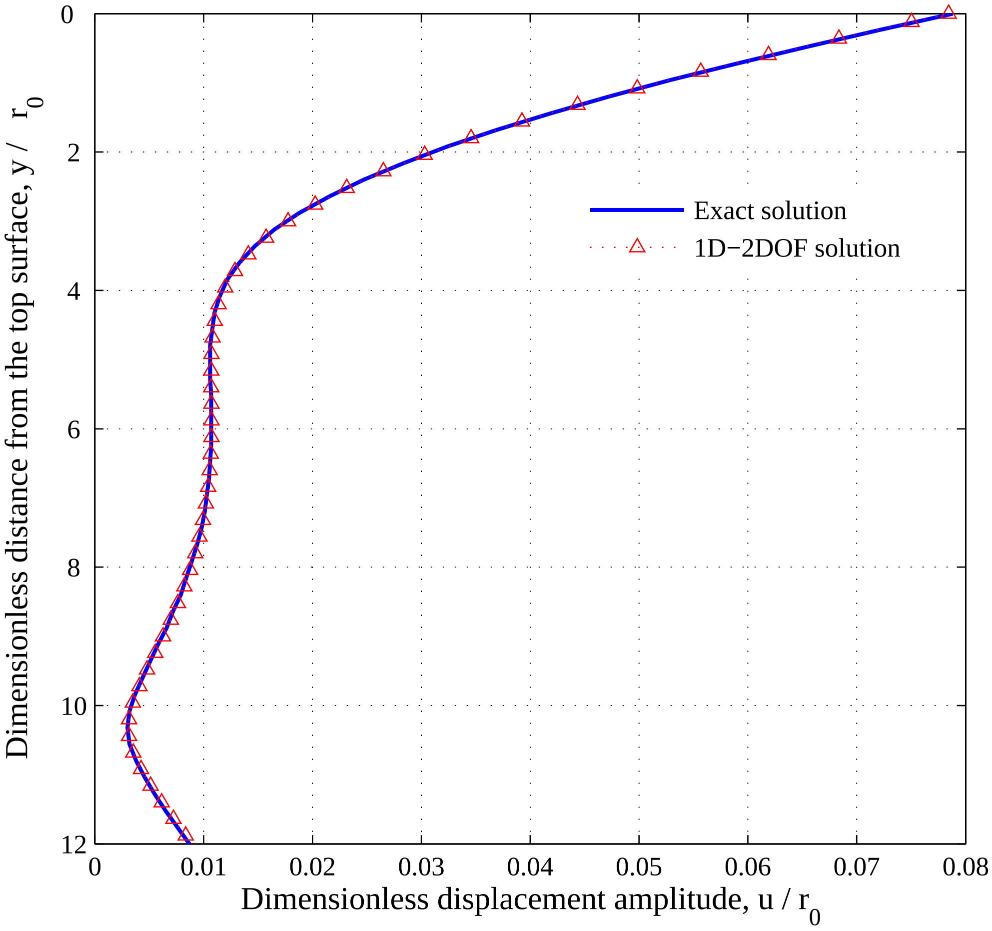

Figure 3.21: The dimensionless displacement amplitude versus dimensionless distance from the top surface of the free-bottom pile.

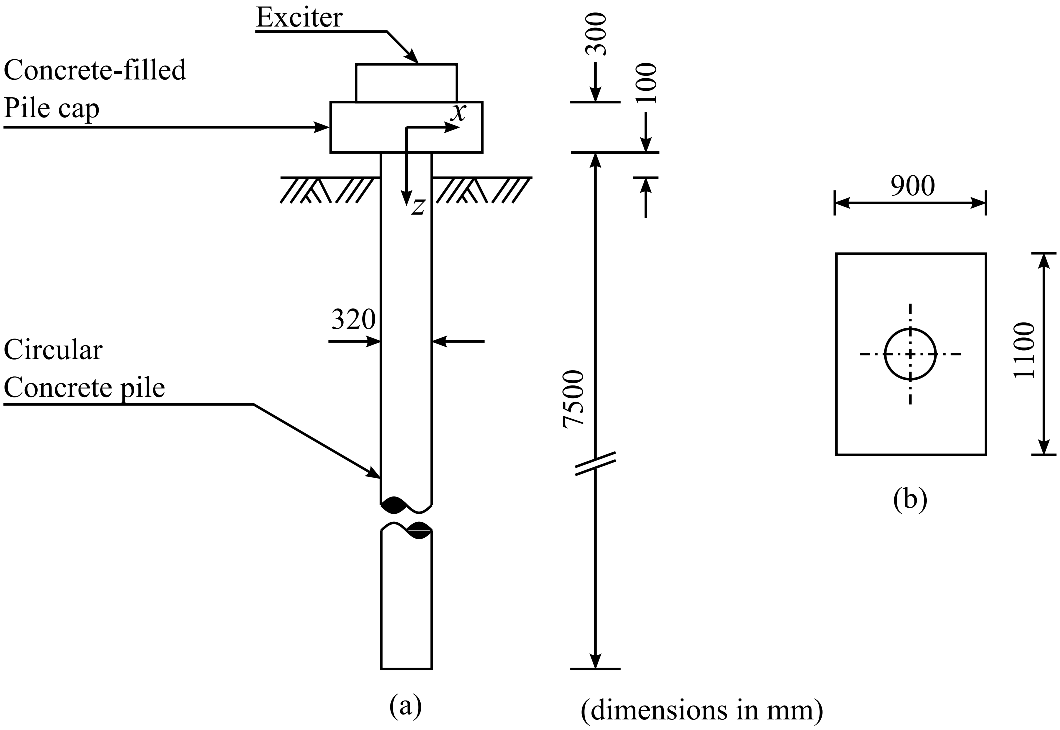

Figure 3.22: The experimental set-up in El-Marsafawi et al (1992): (a) elevation view (b) plan view of cap.

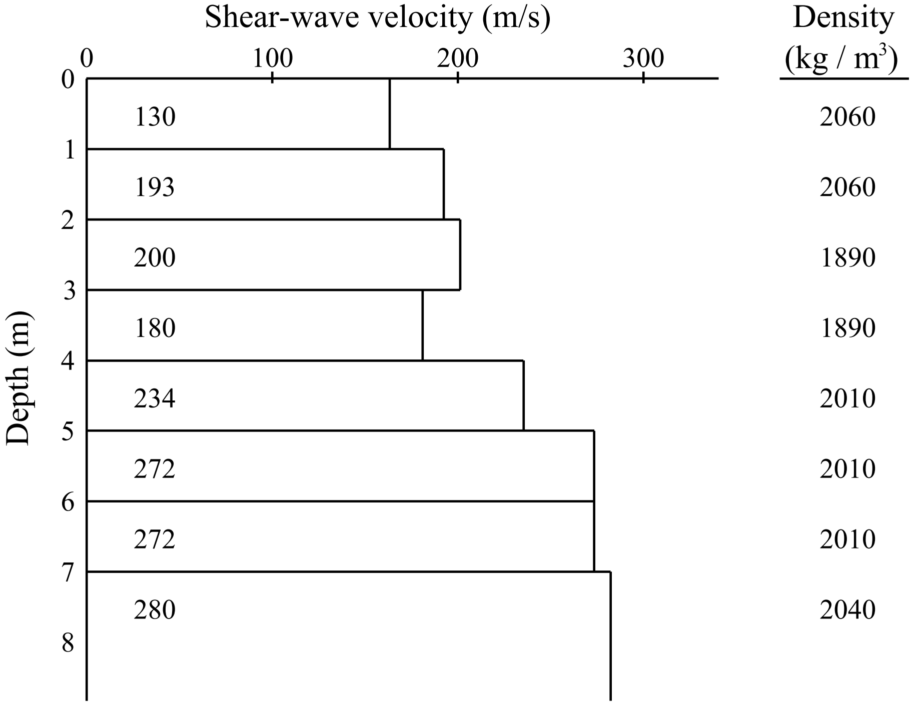

Figure 3.23: Shear-wave velocity and mass-density profiles of the soil

The 7.5 m-long reinforced concrete pile with diameter of 0.32 m was cast-in-place. The pile cap was built in order to achieve a realistic, practical resonant frequency. The cap mass and mass moment of inertia about the out-of-plane principal axis are 860 kg (including the mass of exciter) and 95 $kg \cdot m^2$ respectively. The force excitation is produced by the centrifugal force of the unbalanced mass. The excitation intensity, $m_e \cdot e$ (where m_e is the eccentric mass: e is eccentricity), is the unbalanced mass times the eccentricity and the excitation force is determined by

$$P(t) = (m_e e) \cdot \omega^2 \cdot \cos(\omega t) \tag{3.80}$$

The plot in the Figure 3.24 exhibits the dimensionless displacement amplitude at the top of the pile cap versus the excitation frequency in Hz. The triangular and circular markers represent the experimental data corresponding to the excitation intensity, $m_e \cdot e = 96\text{kg} \cdot \text{mm}$, and the result from 1D-2DOF ring model respectively. Clearly, the FE model does not predict the correct amplitude or resonant frequency. Also, note that the results from the test with the higher excitation intensities ($m_e \cdot e$ = 171 and 259 kg·mm.) are almost identical indicating that the system behaves in the elastic range.

3.4 Disk Behavior at Low Frequencies

Referring to Figure 3.24, it can be inferred from the resonant-frequency overestimation that the actual pile system is less stiff than the FE model of the pile with 1D-2DOF soil model. The peak of the response curve (the dimensionless amplitude at resonant frequency) from the FE model is lower than the

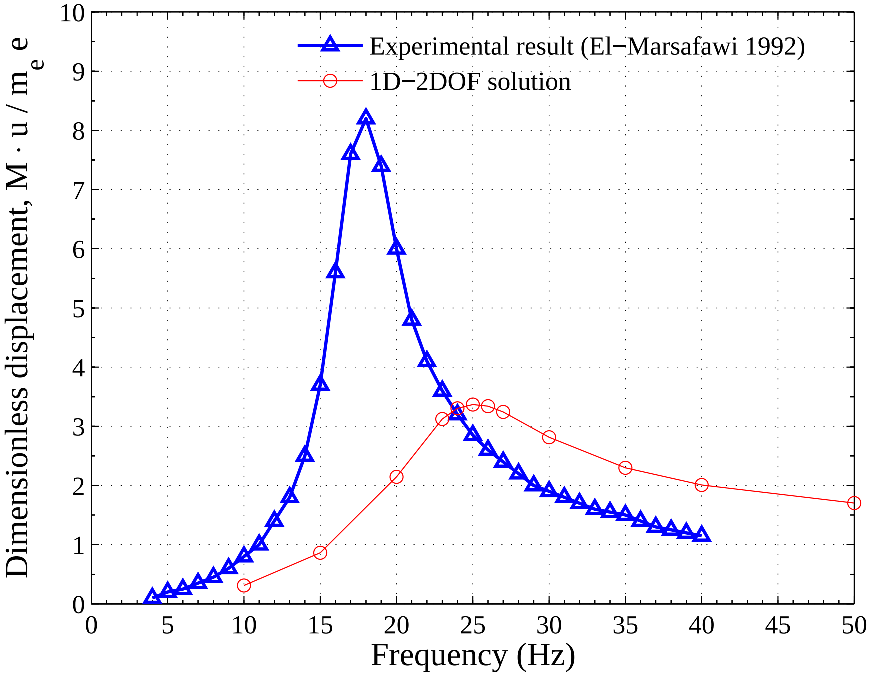

Figure 3.24: Dimensionless displacement amplitude versus excitation frequency plot from experimental data and 1D-2DOF model

peak from experimental result, caused by underestimation of the soil real stiffness. A sample problem of the mass,spring, and dashpot system representing the pile, cap, and soil is illustrated in Figure 3.25.

The parallel spring-dashpot system, denoted by (A), is the representation of a portion of the pile embedded in the soil. The spring (B) is the portion above the ground surface. The complex stiffness of each spring system

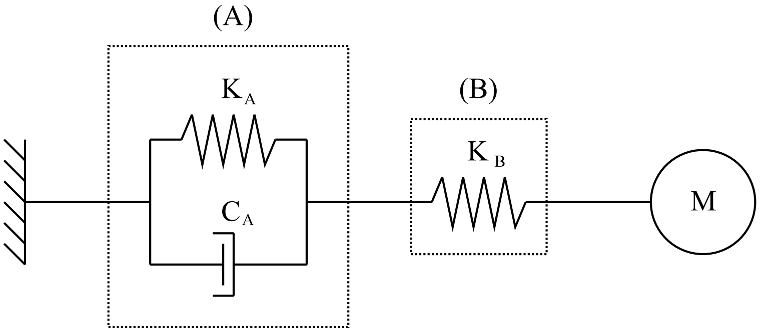

Figure 3.25: A simple spring and dashpot representation of laterally loaded pile

is given by

$$K^{(A)} = K_A + C_A\omega \cdot i \tag{3.81}$$

$$K^{(B)} = K_B \tag{3.82}$$

The overall stillness of the system can be calculated as

$$\begin{aligned} K^{\text{system}} &= \left(\frac{1}{K_A + C_A\omega \cdot i} + \frac{1}{K_B}\right)^{-1} \\ &= \frac{K_A + K_B + C_A\omega \cdot i}{(K_A + C_A\omega \cdot i) \cdot (K_B)} \\ &= \frac{K_A^2 + K_A \cdot K_B + C_A^2}{(K_A^2 + \omega^2 C_A^2) \cdot K_B} + \frac{\omega C_A}{K_A^2 + \omega^2 C_A^2} \cdot i \end{aligned} \tag{3.83}$$

First, the real part of K^{system} is considered since the real stiffness affects the resonant frequency (natural frequency), ω_{n}, of the system:

$$\omega_{\text{n}} \cong \sqrt{\frac{Re(K^{\text{system}})}{M}} \tag{3.84}$$

Equation 3.84 indicates that the resonant frequency of the system is proportional to the square root of the real part of K^{system}. Next, assuming that K_A is underestimated, replace K_A by the larger number, $K_A + \Delta K_A$, in the expression for $Re(K^{\text{system}})$. Then, compare $Re(K^{\text{system}}(K_A))$ with $Re(K^{\text{system}}(K_A + \Delta K_A))$ in the following:

$$\frac{K_A^2 + K_A \cdot K_B + C_A^2}{(K_A^2 + \omega^2 \cdot C_A^2) \cdot K_B} \overset{?}{>} \frac{(K_A + \Delta K_A)^2 + (K_A + \Delta K_A) \cdot K_B + C_A^2}{((K_A + \Delta K_A)^2 + \omega^2 C_A^2) \cdot K_B} \tag{3.85}$$

carry out the expansion of the above inequality to obtain the equivalent comparison

$$K_B^2 \cdot \Delta K_A \cdot \left(K_A^2 + K_A \cdot \Delta K_A - \omega^2 C_A^2\right) \overset{?}{>} 0 \tag{3.86}$$

Normally, the real part of horizontal disk stiffness, S_{u1} (represented by K_A in this simple system), is greater than the imaginary part, S_{u2} (represented by ωC_A), as shown in Figure 2.19, in the low frequency range. Then, the inequality 3.86 is true for low frequencies, thus leading to the conclusion that the underestimated real stiffness of the disk results in the overestimated resonant frequency.

It can be observed from Equation 3.83 that the imaginary stiffness of the system decreases as K_A increases. Thus, the resonant displacement amplitude will increase with higher K_A. The lack of real stiffness of the soil slice as the dimensionless frequency approaches zero is responsible for the low prediction in displacement in the laterally-loaded-pile problem. Indeed, the excitation frequency in typical applications (e.g. earthquake and machine vibration) ranges from 0 to 20 Hz so that the dimensionless frequency, $\omega r/c_s$, will be so small that the lack of disk stiffness will always be problematic in laterally-loaded-pile analysis.

The approximate static stiffness was presented by Novak and Sheta (1982). The real stiffness of the disk, S_{u1}, for the dimensionless frequency range below 0.3 can be prescribed to be S_{u1} corresponding to 0.3 as shown in Figure 3.26. This solution can be applied exclusively to the case of free-head pile because the static spring stiffness of soil slice is actually dependent on pile head fixity and the ratio of pile to soil stiffness. In other words, the deflected shape of the pile affects pile head stiffness as concluded in Gazetas and Dobry (1984).

Then, the pile model with 1D-2DOF element was modified by adding

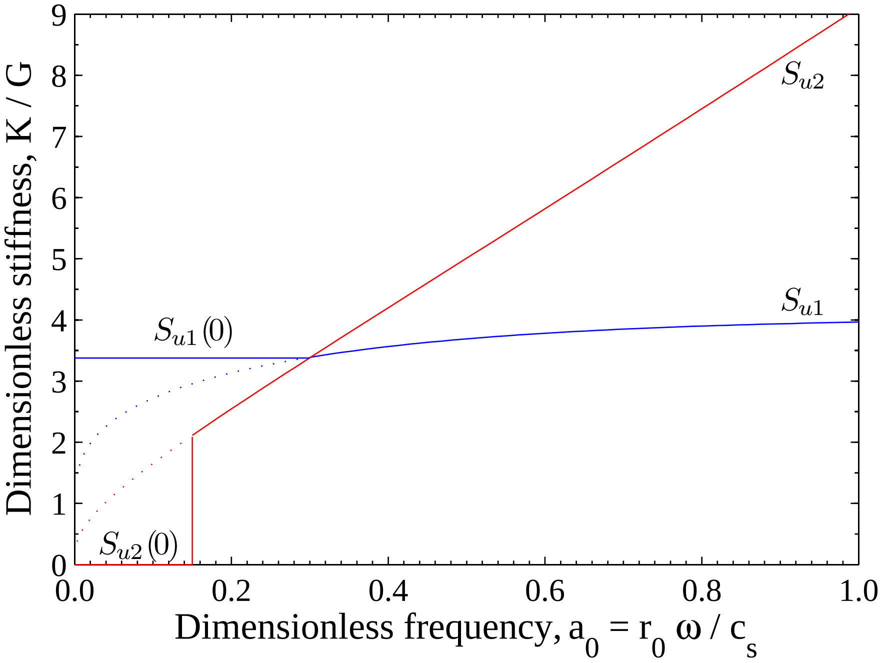

Figure 3.26: Treatment for the lack of disk stiffness for the dimensionless frequency below 0.3 proposed by Novak and Sheta

a constant spring stiffness along the depth of the pile. The spring coefficient was selected to be $2.8G$ which is slightly less than the value suggested in Novak and Sheta (1982). The elastic modulus of the top 50-cm top soil layer is reduced to accommodate the weak top soil by the fourth degree polynomial. The weakness of top soil results in a shift of resonant frequency to the left (lower resonant frequency). Finally, the excellent matches in both peak displacement amplitude and resonant frequency were obtained as shown in Figure 3.27. Notice that the reduction of top soil stiffness by fourth degree polynomial may not be consistent with the actual soil profile. Also, during inelasticity, it is far from clear how the constant spring stiffness can be adjusted appropriately.

Since the independent soil-slice assumption employs plane-strain conditions in the formulation, the out-of-plane shear stress components, τ_{rz}, τ_{zr}, $\tau_{\theta z}$, and $\tau_{z\theta}$, are assumed to be zero. Then, in order to improve disk behavior at low frequencies, a distributed horizontal spring, K_{shear}, providing additional resistance to the soil motion, will be installed uniformly throughout the soil domain. The governing partial differential equation of the vibrating disk in the plane-strain soil medium (Equation 2.48) will be modified as follows:

$$\begin{aligned}(\lambda+2G)\frac{\partial\Delta}{\partial r}-\frac{2G}{r}\frac{\partial\omega_z}{\partial\theta} &= \rho\frac{\partial^2 u}{\partial t^2}+K_{\text{shear}}\cdot u\\ (\lambda+2G)\frac{\partial\Delta}{r\partial\theta}+2G\frac{\partial\omega_z}{\partial r} &= \rho\frac{\partial^2 v}{\partial t^2}+K_{\text{shear}}\cdot v\end{aligned}\tag{3.87}$$

If the soil motion is harmonic, the soil displacements u and v are given by:

$$\begin{aligned}u(r,\theta,t) &= U(r,\theta)\cdot\sin(\omega t)\\ v(r,\theta,t) &= V(r,\theta)\cdot\sin(\omega t)\end{aligned}\tag{3.88}$$

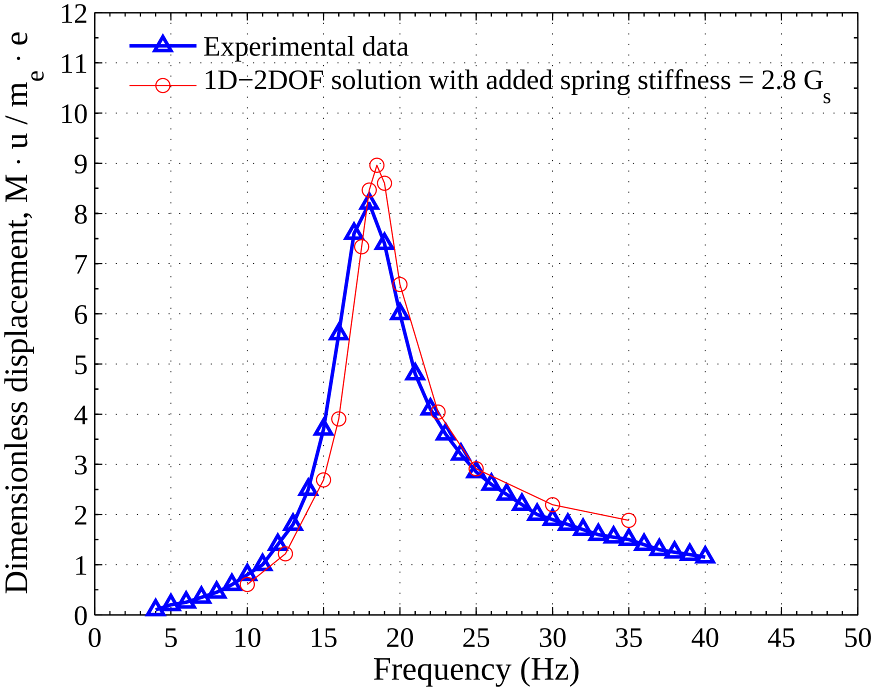

Figure 3.27: Dimensionless displacement amplitude versus excitation frequency plot from experimental data and 1D-2DOF model with additional stiffness of $2.8G$

Substituting the above expressions of u and v into Equation 3.87:

$$\begin{aligned}(\lambda+2G)\frac{\partial\Delta}{\partial r}-\frac{2G}{r}\frac{\partial\omega_z}{\partial\theta} &= -(\rho\omega^2-K_{\text{shear}})\cdot U\\ (\lambda+2G)\frac{\partial\Delta}{r\partial\theta}+2G\frac{\partial\omega_z}{\partial r} &= -(\rho\omega^2-K_{\text{shear}})\cdot V\end{aligned}\tag{3.89}$$

where

$$\begin{aligned}\Delta &= \frac{1}{r}\frac{\partial(r\cdot U)}{\partial r}+\frac{1}{r}\frac{\partial V}{\partial\theta}\\ \omega_z &= \frac{1}{2}\Big(\frac{1}{r}\frac{\partial(r\cdot V)}{\partial r}-\frac{1}{r}\frac{\partial U}{\partial\theta}\Big)\end{aligned}\tag{3.90}$$

Since it can be observed that Equation 3.89 resembles Equation 2.50, therefore, the variation of complex disk stiffness without distributed shear spring with respect to $\omega_{\text{effective}}/c_s$ will be identical to the variation of complex disk stiffness with shear spring with respect to $\sqrt{(\omega^2_{\text{excitation}}/c_s^2) - (K_{\text{shear}}/G)}$. Now, consider the complex disk stiffness in the presence of a shear spring over a range of excitation frequencies. Notice that, for the frequency range from $\omega_{\text{excitation}} = 0$ to $\omega_{\text{excitation}} = \sqrt{K_{\text{shear}}/G}$ (cut-off frequency), the corresponding $\omega_{\text{effective}}$ is negative. The real stiffness is decreasing from $\omega_{\text{excitation}} = 0$ and approaching zero at $\omega^{\text{cut-off}}$ while the imaginary part is equal to zero throughout this frequency range.

Next, consider the frequency range above the cut-off frequency. The variation of complex disk stiffness is identical to the stiffness of the disk without distributed shear spring. The plot of complex disk stiffness versus the excitation frequency is shown in Figure 3.28 with the shear-wave velocity, shear-spring stiffness, and radius of the pile equal to 100, 3.0, and 0.16, respectively.

The shear-spring stiffness, K_{shear}, was given as $b^2 \cdot G$ in Mylonakis (2001). Assuming that the displacement field of the soil can be written in the form:

$$\delta(r, \theta, z) = \Delta(r, \theta) \cdot \chi(z) \tag{3.91}$$

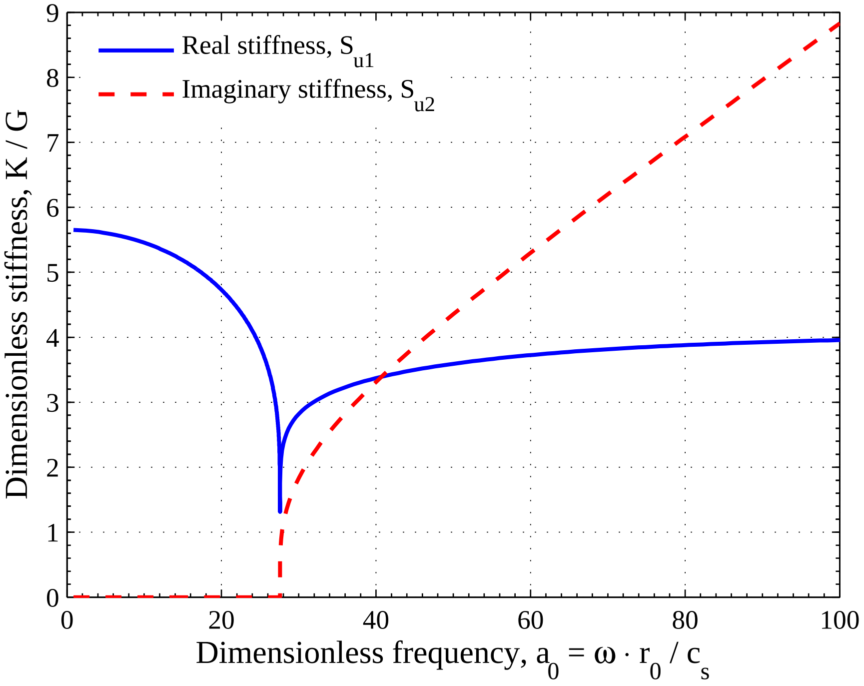

Figure 3.28: Vibrating disk stiffness with the introduction of horizonal shear spring

where $\chi(z)$ is the approximate deflected shape of the pile and neglecting the vertical soil displacement w, the shear stresses, τ_{rz} and $\tau_{\theta z}$, are given by:

$$\begin{aligned} \tau_{rz} &= G\frac{\partial^2 u}{\partial z^2} = G \cdot U(r,\theta) \cdot \frac{\partial^2 \chi(z)}{\partial z^2} \\ \tau_{\theta z} &= G\frac{\partial^2 v}{\partial z^2} = G \cdot V(r,\theta) \cdot \frac{\partial^2 \chi(z)}{\partial z^2} \end{aligned} \tag{3.92}$$

Now, the variation with respect to the z direction will be replaced by a coefficient b^2 (Mylonakis 2001).

$$\begin{aligned} G \cdot U(r,\theta) \cdot \frac{\partial^2 \chi(z)}{\partial z^2} &\approx G \cdot U(r,\theta) \cdot b^2 \\ G \cdot V(r,\theta) \cdot \frac{\partial^2 \chi(z)}{\partial z^2} &\approx G \cdot V(r,\theta) \cdot b^2 \end{aligned} \tag{3.93}$$

where

$$\frac{\partial^2\chi(z)}{\partial z^2} \approx \int_0^L \left(\frac{\mathrm{d}\chi(z)}{\mathrm{d}z}\right)^2 \mathrm{d}z \,/ \int_0^L \chi(z)^2 \mathrm{d}z = b^2 \tag{3.94}$$

Although this modification renders the overall pile behavior more realistic, the limitations such as frequency dependence and accuracy of the treatment for soil inelasticity still persist. Moreover, for the pile embedded in homogeneous soil layer, the available solution employing 3-D elasticity with the assumption that the soil movement in the vertical direction is negligible works even more accurately for the case of slender pile since the calculation of the factor, b^2, involves the assumed pile deflected shape. A more sophisticated improvement to the 1D-2DOF ring element will be explained in detail in the next chapter.

Chapter 4

Ring Element for Shear Interactions between Soil-Slice

Because of the lack of (static) stiffness in the soil slice model under plane-strain conditions at low frequencies discussed in Chapter 3, improvements of the computed behavior of the soil slice model will be made herein by introduction of shear interactions between soil slices. The technique by which the angular variable, θ, was omitted in Chapter 3 will be employed in order to maintain computational simplicity. In this improved formulation, all stress components of 3-D mechanics will be taken into account but, still, approximation will persist in the strain calculation. The soil vertical displacement will be taken as zero. The formulation of the complete 3-D ring element denoted by 2D-3DOF is also described herein and the results comparison is included. Later in this chapter, the limitation of such approximation will be discussed.

In this chapter, the formulation including the shear interactions between soil slices will be presented first. Next, the closed-form solution of the vibrating circular pile embedded in a homogeneous soil layer with the assumed zero soil z-displacement presented by Novak and Nogami (1977) will be explained briefly. The results will be validated subsequently with closed-form solution and 3-D FE solution. Finally, the solution from FE model with 2D-

2DOF ring element will be compared with the available experimental results.

4.1 Ring Finite Element with Shear Interaction

4.1.1 Stiffness Matrix

The behavior of the 1-D ring element (1D-2DOF) will be improved by introduction of previously omitted shear strain components, γ_{rz} and $\gamma_{\theta z}$. The strain calculations employ the soil displacements at the top and the bottom of the element rather than using just displacements at the middle of the slice. This introduction of the shear strains between soil slices will not change the soil discretization. However, the bandwidth of the resulting system of equations will be increased causing a slight increase of computational cost from 1D-2DOF element. Figures 4.1 (a) and (b) illustrate the differences in the nodal locations and nodal displacements of the plane 1D-2DOF model and the model with shear interactions that will be referred to as the 2D-2DOF FE model.

The variation of soil displacements with respect to the circular cylindrical coordinates r, θ, z, and time t, assuming purely-elastic behavior, can be written as:

$$u(r,\theta,z,t) = U(r,z,t)\cdot\cos(\theta) \tag{4.1}$$

$$v(r,\theta,z,t) = -V(r,z,t)\cdot\sin(\theta) \tag{4.2}$$

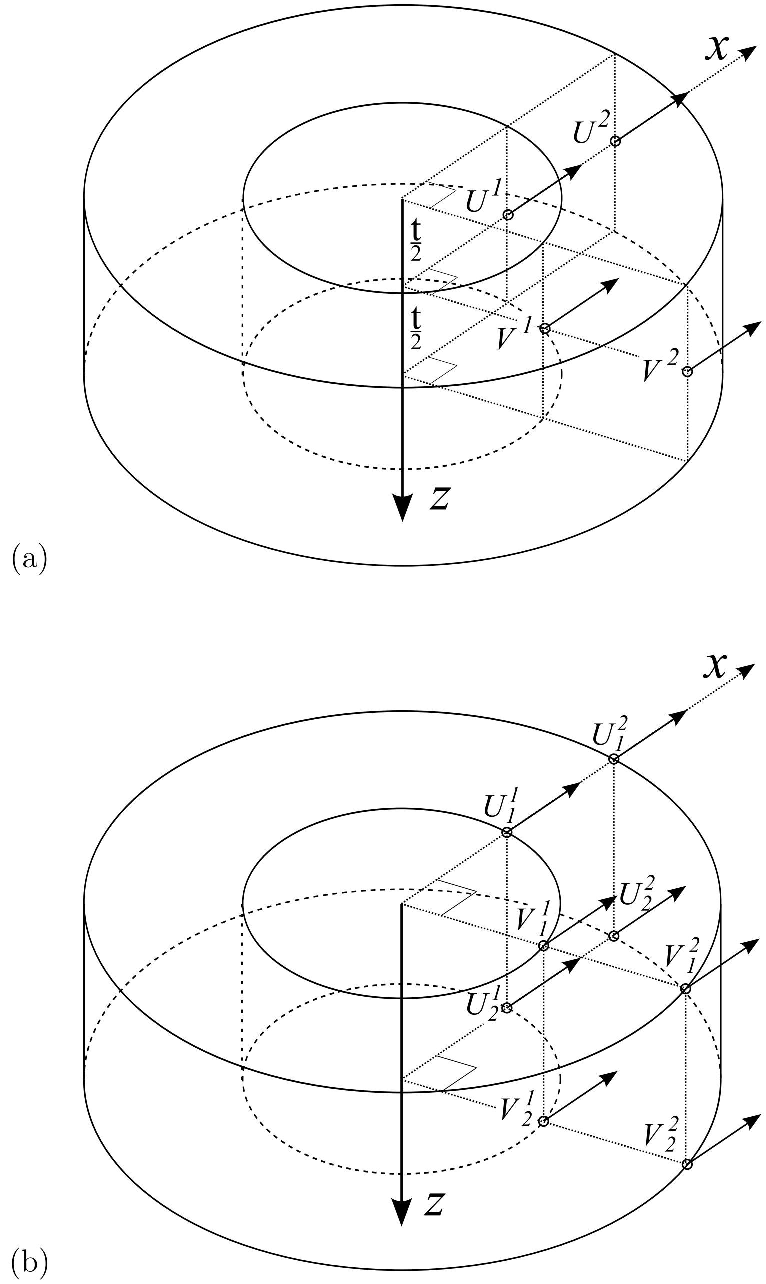

Figure 4.1: (a) Plane-strain 1D-2DOF element: (b) 2D-2DOF ring element with variation in the z-direction.

Next, the strain components can be calculated from the displacements in Equations 4.1 and 4.2 as follows:

$$\begin{align*}
\varepsilon_r &= \frac{\partial u}{\partial r} \\
&= \frac{\partial U}{\partial r} \cdot \cos(\theta) \tag{4.3} \\
\varepsilon_\theta &= \frac{u}{r} + \frac{1}{r}\frac{\partial v}{\partial \theta} \\
&= \frac{U}{r} \cdot \cos(\theta) - \frac{V}{r} \cdot \cos(\theta) \\
&= \frac{U - V}{r} \cdot \cos(\theta) \tag{4.4} \\
\varepsilon_z &= \frac{\partial w}{\partial z} \cong 0 \tag{4.5} \\
\gamma_{r\theta} &= \frac{\partial v}{\partial r} - \frac{v}{r} + \frac{1}{r}\frac{\partial u}{\partial \theta} \\
&= -\frac{\mathrm{d}V}{r} \cdot \sin(\theta) + \frac{V}{r} \cdot \sin(\theta) - \frac{U}{r} \cdot \sin(\theta) \\
&= -\left(\frac{\mathrm{d}V}{\mathrm{d}r} + \frac{U - V}{r}\right) \cdot \sin(\theta) \tag{4.6} \\
\gamma_{rz} &= \frac{\partial w}{\partial r} + \frac{\partial u}{\partial z} \\
&\cong \frac{\partial U}{\partial z} \cdot \cos(\theta) \tag{4.7} \\
\gamma_{z\theta} &= \frac{1}{r} \cdot \frac{\partial w}{\partial \theta} + \frac{\partial v}{\partial z} \\
&\cong -\frac{\partial V}{\partial z} \cdot \sin(\theta) \tag{4.8}
\end{align*}$$

Now, the displacements can be approximated in terms of nodal values and interpolation functions. As can be seen from Equation 4.6, 4.7, and 4.8, the influence of the z-displacement on the strain components is neglected. With ζ and η as the local coordinates in radial and vertical directions, as shown in Figure 4.2, the displacement approximations can be written as:

$$u(r,\theta,z,t) \approxeq \sum_{m=1}^{2}\sum_{n=1}^{2} U_n^m(t)\cdot\Psi_m(\zeta)\cdot\Phi_n(\eta) \tag{4.9}$$

$$v(r,\theta,z,t) \approxeq \sum_{m=1}^{2}\sum_{n=1}^{2} V_n^m(t)\cdot\Psi_m(\zeta)\cdot\Phi_n(\eta) \tag{4.10}$$

where Ψ_m is the interpolation function with respect to the radial direction at location m (m =1,2): Φ_n is the interpolation function with respect to the vertical direction at location n (n = 1,2). Considering the orientations of local coordinates in Figure 4.2, the expressions of Ψ_m and Φ_n (m,n =1,2) are as follows:

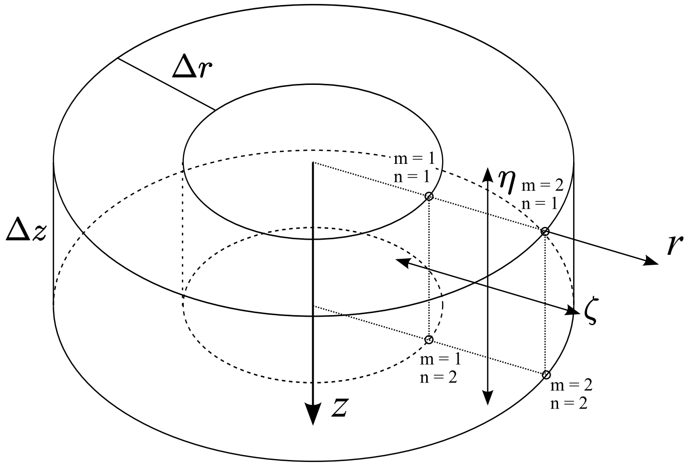

Figure 4.2: Orientation of local coordinates.

$$\Psi_1(\zeta) = \frac{1}{2}(1-\zeta) \tag{4.11}$$

$$\Psi_2(\zeta) = \frac{1}{2}(1+\zeta) \tag{4.12}$$

$$\Phi_1(\eta) = \frac{1}{2}(1+\eta) \tag{4.13}$$

$$\Phi_2(\eta) = \frac{1}{2}(1-\eta) \tag{4.14}$$

with

$$\begin{aligned} r &= r_{\text{inner}} + \frac{\Delta r}{2}\cdot(\zeta+1) && (4.15)\\ z &= z_{\text{top}} + \frac{\Delta z}{2}\cdot(1-\eta) && (4.16) \end{aligned}$$

where Δr is the difference between the inner and outer radii of the element while Δz is the thickness of the element shown in Figure 4.2. Then, the derivatives of r and z with respect to ζ and η, respectively, are given by:

$$\begin{aligned} \frac{\mathrm{d}r}{\mathrm{d}\zeta} &= \frac{\Delta r}{2}\\ \frac{\mathrm{d}z}{\mathrm{d}\eta} &= -\frac{\Delta z}{2} && (4.17) \end{aligned}$$

The nonzero strain components from Equations 4.3 to 4.8 can be rewritten as:

$$\varepsilon_r = \sum_{m=1}^{2}\sum_{n=1}^{2}\left[U_n^m\cdot\frac{\mathrm{d}\Psi_m(\zeta)}{\mathrm{d}r}\cdot\Phi_n(\eta)\right]\cdot\cos(\theta) \qquad (4.18)$$

$$\varepsilon_\theta = \sum_{m=1}^{2}\sum_{n=1}^{2}\left[\frac{U_n^m - V_n^m}{r}\cdot\Psi_m(\zeta)\cdot\Phi_n(\eta)\right]\cdot\cos(\theta) \qquad (4.19)$$

$$\gamma_{r\theta} = \sum_{m=1}^{2}\sum_{n=1}^{2}\left[U_n^m\Phi_n(\eta)\frac{\Psi_m(\zeta)}{r} + V_n^m\Phi_n(\eta)\left(\frac{\mathrm{d}\Psi_m(\zeta)}{\mathrm{d}r} - \frac{\Psi_m(\zeta)}{r}\right)\right]\cdot[-\sin(\theta)] \qquad (4.20)$$

$$\gamma_{rz} = \sum_{m=1}^{2}\sum_{n=1}^{2}\left[U_n^m\Psi_m(\zeta)\frac{\mathrm{d}\Phi_n(\eta)}{\mathrm{d}z}\right]\cdot(\cos(\theta)) \qquad (4.21)$$

$$\gamma_{z\theta} = \sum_{m=1}^{2}\sum_{n=1}^{2}\left(V_n^m\Psi_m(\zeta)\frac{\mathrm{d}\Phi_n(\eta)}{\mathrm{d}z}\right)\cdot(-\sin(\theta)) \qquad (4.22)$$

The functions of θ will be omitted next since they can be replaced by the constant, π, when the integrals are carried out with respect to θ. Now, the strain column-vector can be expressed in the matrix form as:

$$\underset{\sim}{\varepsilon} = \underset{\sim}{B}\underset{\sim}{U} \tag{4.23}$$

where:

$$\underset{\sim}{U} = \begin{bmatrix} U_1^1 & V_1^1 & U_1^2 & V_1^2 & U_2^1 & V_2^1 & U_2^2 & V_2^2 \end{bmatrix}^T \tag{4.24}$$

$$\underset{\sim}{B} = \begin{bmatrix} \chi_{11} & 0 & \chi_{12} & 0 & \chi_{21} & 0 & \chi_{22} & 0 \\ \beta_{11} & -\beta_{11} & \beta_{12} & -\beta_{12} & \beta_{21} & -\beta_{21} & \beta_{22} & -\beta_{22} \\ \beta_{11} & \alpha_{11} & \beta_{12} & \alpha_{12} & \beta_{21} & \alpha_{21} & \beta_{22} & \alpha_{22} \\ \psi_{11} & 0 & \psi_{12} & 0 & \psi_{21} & 0 & \psi_{22} & 0 \\ 0 & \psi_{11} & 0 & \psi_{12} & 0 & \psi_{21} & 0 & \psi_{22} \end{bmatrix} \tag{4.25}$$

and

$$\begin{aligned} \chi_{pq} &= \Phi_q(\eta) \cdot \frac{\mathrm{d}\Psi_p(\zeta)}{\mathrm{d}r} \\ &= \Phi_q(\eta) \cdot \frac{\mathrm{d}\Psi_p(\zeta)}{\mathrm{d}\zeta} \cdot \frac{\mathrm{d}\zeta}{\mathrm{d}r} \\ &= \Phi_q(\eta) \cdot \frac{\mathrm{d}\Psi_p(\zeta)}{\mathrm{d}\zeta} \cdot \frac{2}{\Delta r} \end{aligned} \tag{4.26}$$

$$\beta_{pq} = \frac{\Psi_p(\zeta) \cdot \Phi_q(\eta)}{r} \tag{4.27}$$

$$\begin{aligned} \alpha_{pq} &= \Phi_q(\eta) \left(\frac{\mathrm{d}\Psi_p(\zeta)}{\mathrm{d}r} - \frac{\Psi_p(\zeta)}{r} \right) \\ &= \Phi_q(\eta) \left(\frac{\mathrm{d}\Psi_p(\zeta)}{\mathrm{d}\zeta} \cdot \frac{\mathrm{d}\zeta}{\mathrm{d}r} - \frac{\Psi_p(\zeta)}{r} \right) \\ &= \Phi_q(\eta) \left(\frac{\mathrm{d}\Psi_p(\zeta)}{\mathrm{d}\zeta} \cdot \frac{2}{\Delta r} - \frac{\Psi_p(\zeta)}{r} \right) \end{aligned} \tag{4.28}$$

$$\begin{aligned} \psi_{pq} &= \Psi_p(\zeta) \frac{\mathrm{d}\Phi_q(\eta)}{\mathrm{d}z} \\ &= \Psi_p(\zeta) \frac{\mathrm{d}\Phi_q(\eta)}{\mathrm{d}\eta} \cdot \frac{\mathrm{d}\eta}{\mathrm{d}z} \\ &= -\Psi_p(\zeta) \frac{\mathrm{d}\Phi_q(\eta)}{\mathrm{d}z} \cdot \frac{2}{\Delta z} \end{aligned} \tag{4.29}$$

4.1.2 Material Inelasticity

The procedure for inelastic analysis will be the same as the one presented in Chapter 3. Two different treatments, involving different stress components, will be applied in two separate regions: the longitudinal-wave region and the shear-wave region. The purely-elastic distribution of stress components with respect to the angular coordinate θ will be assumed to hold approximately even for inelastic analysis.

4.1.2.1 Inelastic Treatment for Longitudinal-Wave Region

Since the stress components, σ_r, σ_θ, σ_z, and τ_{rz} correspond to the location $\theta = 0$, the trial shear stress intensity for the longitudinal-wave region can be computed by:

$$\begin{aligned} T^{\text{trial}} &= \sqrt{\sigma_r^2 + \sigma_\theta^2 + \sigma_z^2 + \tau_{rz}^2 + \tau_{zr}^2} \\ &= \sqrt{\sigma_r^2 + \sigma_\theta^2 + \sigma_z^2 + 2 \cdot \tau_{rz}^2} \end{aligned} \tag{4.30}$$

The tangent rigidity matrix for the 2D-2DOF ring element can be expressed as:

$$\underset{\sim}{D} = \begin{bmatrix} L_{11} & L_{12} & 0 & 0 & 0 \\ L_{21} & L_{22} & 0 & 0 & 0 \\ 0 & 0 & S_{33} & 0 & 0 \\ 0 & 0 & 0 & L_{44} & 0 \\ 0 & 0 & 0 & 0 & S_{55} \end{bmatrix} \tag{4.31}$$

The L entries will be calculated from Equation 3.27 with the vector of trial deviatoric stress, $\underset{\sim}{S}^{\text{trial}}$, given by

$$\underset{\sim}{S}^{\text{trial}} = \begin{bmatrix} S_r^{\text{trial}} & S_\theta^{\text{trial}} & S_z^{\text{trial}} & S_{rz}^{\text{trial}} \end{bmatrix}^T \tag{4.32}$$

Then, by Equation 3.27, the tangent rigidity matrix of the longitudinal-wave region can be written as follows:

$$\begin{bmatrix} D^L_{11} & D^L_{12} & D^L_{13} & D^L_{14} \\ D^L_{21} & D^L_{22} & D^L_{23} & D^L_{24} \\ D^L_{31} & D^L_{32} & D^L_{33} & D^L_{34} \\ D^L_{41} & D^L_{42} & D^L_{43} & D^L_{44} \end{bmatrix} \tag{4.33}$$

Finally, the individual L entries are given by:

$$\begin{aligned} L_{11} &= D^L_{11} \quad , \quad L_{12} = D^L_{12} \\ L_{21} &= D^L_{21} \quad , \quad L_{22} = D^L_{22} \\ L_{44} &= D^L_{44} \end{aligned} \tag{4.34}$$

4.1.2.2 Inelastic Treatment for Shear-Wave Region

The trial shear stress intensity for the shear-wave region involves $\tau_{r\theta}$, $\tau_{\theta r}$, $\tau_{\theta z}$, and $\tau_{z\theta}$:

$$\begin{aligned} T^{\text{trial}} &= \sqrt{\tau^2_{r\theta} + \tau^2_{\theta r} + \tau^2_{\theta z} + \tau^2_{z\theta}} \\ &= \sqrt{2 \cdot \tau^2_{r\theta} + 2 \cdot \tau^2_{\theta z}} \end{aligned} \tag{4.35}$$

In the element tangent rigidity matrix, the entries corresponding to the shear-wave region, denoted by the S entries in Equation 4.31, will be calculated by taking the vector of trial deviatoric stress as:

$$\underset{\sim}{S}^{\text{trial}} = \begin{bmatrix} S^{\text{trial}}_{r\theta} & S^{\text{trial}}_{\theta z} \end{bmatrix}^T \tag{4.36}$$

By Equation 3.27,

$$\underset{\sim}{D}^S = \begin{bmatrix} D^S_{11} & D^S_{12} \\ D^S_{21} & D^S_{22} \end{bmatrix} \tag{4.37}$$

and the individuals entries in the element tangent rigidity matrix are given by:

$$S_{33} = D^S_{11} \quad , \quad S_{55} = D^S_{22} \tag{4.38}$$

4.1.3 Mass Matrix

The radial part of the consistent mass matrix for the 2D-2DOF element is identical to the mass matrix for the axial (z) part of 1D-2DOF element (without shear interaction) in Equation 3.48. The consistent mass matrix is given by:

$$\begin{aligned}
& 2\pi \int_{z^{\mathrm{top}}}^{z^{\mathrm{bottom}}} (\underset{\sim}{\Phi}^T(\eta)\underset{\sim}{\Phi}(\eta))\mathrm{d}z \\
&= 2\pi \int_{1}^{-1} (\underset{\sim}{\Phi}^T(\eta)\underset{\sim}{\Phi}(\eta)) \left(-\frac{\Delta z}{2}\right) \mathrm{d}\eta \\
&= 2\pi \int_{-1}^{1} (\underset{\sim}{\Phi}^T(\eta)\underset{\sim}{\Phi}(\eta)) \left(\frac{\Delta z}{2}\right) \mathrm{d}\eta \qquad (4.39) \\
&= \pi \begin{bmatrix} 1/3 & 1/6 \\ 1/6 & 1/3 \end{bmatrix} \qquad (4.40)
\end{aligned}$$

Finally, the complete mass matrix of the 2D-2DOF ring element can be cast as follows:

$$\frac{(\pi \cdot \Delta z \cdot \Delta r \cdot \rho)}{36} \begin{bmatrix}
2\mathbb{m}_1 & 0 & \mathbb{m}_1 & 0 & 2\mathbb{m}_2 & 0 & \mathbb{m}_2 & 0 \\
0 & 2\mathbb{m}_1 & 0 & \mathbb{m}_1 & 0 & 2\mathbb{m}_2 & 0 & \mathbb{m}_2 \\
\mathbb{m}_1 & 0 & 2\mathbb{m}_1 & 0 & \mathbb{m}_2 & 0 & 2\mathbb{m}_2 & 0 \\
0 & \mathbb{m}_1 & 0 & 2\mathbb{m}_1 & 0 & \mathbb{m}_2 & 0 & 2\mathbb{m}_2 \\
2\mathbb{m}_2 & 0 & \mathbb{m}_2 & 0 & 2\mathbb{m}_3 & 0 & \mathbb{m}_3 & 0 \\
0 & 2\mathbb{m}_2 & 0 & \mathbb{m}_2 & 0 & 2\mathbb{m}_3 & 0 & \mathbb{m}_3 \\
\mathbb{m}_2 & 0 & 2\mathbb{m}_2 & 0 & \mathbb{m}_3 & 0 & 2\mathbb{m}_3 & 0 \\
0 & \mathbb{m}_2 & 0 & 2\mathbb{m}_2 & 0 & \mathbb{m}_3 & 0 & 2\mathbb{m}_3
\end{bmatrix} \tag{4.41}$$

ρ being mass-density and

$$\begin{aligned} \mathbb{m}_1 &= 2r_i + \frac{\Delta r}{2} \\ \mathbb{m}_2 &= r_i + \frac{\Delta r}{2} \\ \mathbb{m}_3 &= 2r_i + \frac{3\Delta r}{2} \end{aligned} \tag{4.42}$$

4.1.4 Pile Element

The pile element based on the Euler beam formulation will be modified here for conformity with the soil elements (displacement continuity). This is because the 2D-2DOF and 2D-3DOF model linearly interpolate the displacement in the horizontal and vertical directions while the pile displacement in the conventional beam element is approximated by Hermite interpolation functions and the nonconformity of soil and pile displacements occurs at the interface. In order to resolve the lack of conformity, a modified beam element with linear interpolation of displacements will be derived as follows:

First, consider the beam element with positive sense of nodal displacements and rotations in Figure 4.3. The pile elastic modulus, shear modulus, cross-sectional area, area moment of inertia, and length are equal to E, G, A, I, and L, respectively. Assuming that there is no out-of-plane displacement in the z-axis, the displacement u and v can be approximated by:

$$v = \phi_1(\zeta) \cdot v_1 + \phi_2(\zeta) \cdot v_2 \tag{4.43}$$

$$u = \phi_1 \cdot (-\theta_1 \cdot y) + \phi_2 \cdot (-\theta_2 \cdot y) \tag{4.44}$$

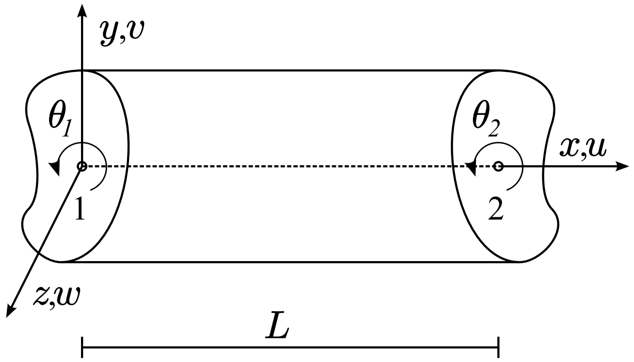

Figure 4.3: Positive sense of beam displacements and rotations

where the interpolation functions are given by:

$$\phi_1 = \frac{1}{2}(1-\zeta) \tag{4.45}$$

$$\phi_2 = \frac{1}{2}(1+\zeta) \tag{4.46}$$

and the location x can be written in terms of ζ as follows:

$$x = x_1 + \frac{L}{2}(1+\zeta) \tag{4.47}$$

$$\frac{\mathrm{d}x}{\mathrm{d}\zeta} = \frac{L}{2} \tag{4.48}$$

Now, the two non-zero strain components are given by:

$$\varepsilon_x = \frac{\mathrm{d}u}{\mathrm{d}x} = \frac{\mathrm{d}\phi_1}{\mathrm{d}\zeta}\cdot\frac{2}{L}(-\theta_1\cdot y) + \frac{\mathrm{d}\phi_2}{\mathrm{d}\zeta}\cdot\frac{2}{L}(-\theta_2\cdot y) \tag{4.49}$$

$$\gamma_{xy} = \frac{\partial v}{\partial x} + \frac{\partial u}{\partial y} = \phi_1\cdot(-\theta_1) + \phi_2\cdot(-\theta_2) + \frac{\mathrm{d}\phi_1}{\mathrm{d}\zeta}\frac{2}{L}v_1 + \frac{\mathrm{d}\phi_2}{\mathrm{d}\zeta}\frac{2}{L}v_2 \tag{4.50}$$

or in the following matrix form

$$\underset{\sim}{\varepsilon} = \begin{bmatrix} \varepsilon_x \\ \gamma_{xy} \end{bmatrix} = \begin{bmatrix} 0 & -\frac{\mathrm{d}\phi_1}{\mathrm{d}\zeta}\cdot\frac{2}{L}\cdot y & 0 & -\frac{\mathrm{d}\phi_2}{\mathrm{d}\zeta}\cdot\frac{2}{L}\cdot y \\ \frac{\mathrm{d}\phi_1}{\mathrm{d}\zeta}\cdot\frac{2}{L} & -\phi_1 & \frac{\mathrm{d}\phi_2}{\mathrm{d}\zeta}\cdot\frac{2}{L} & -\phi_2 \end{bmatrix} \begin{bmatrix} v_1 \\ \theta_1 \\ v_2 \\ \theta_2 \end{bmatrix} \tag{4.51}$$

Then,

$$\underset{\sim}{B} = \left[\begin{array}{c} B_\varepsilon \\ B_\gamma \end{array} \right] = \left[\begin{array}{cccc} 0 & -\dfrac{\mathrm{d}\phi_1}{\mathrm{d}\zeta} \cdot \dfrac{2}{L} \cdot y & 0 & -\dfrac{\mathrm{d}\phi_2}{\mathrm{d}\zeta} \cdot \dfrac{2}{L} \cdot y \\ \dfrac{\mathrm{d}\phi_1}{\mathrm{d}\zeta} \cdot \dfrac{2}{L} & -\phi_1 & \dfrac{\mathrm{d}\phi_2}{\mathrm{d}\zeta} \cdot \dfrac{2}{L} & -\phi_2 \end{array} \right] \tag{4.52}$$

Next, the virtual work associated to the above strain components is given by:

$$\delta \underset{\sim}{U}^T \left[\int_{\text{section}} \int_{-1}^{1} \underset{\sim}{B}^T \underset{\sim}{D} \underset{\sim}{B} \, \mathrm{d}x d(\text{section}) \right] \underset{\sim}{U} \tag{4.53}$$

where $\underset{\sim}{D}$ is the tangent rigidity matrix as follows:

$$\underset{\sim}{D} = \left[\begin{array}{cc} E_t & 0 \\ 0 & G_t \end{array} \right] \tag{4.54}$$

Now, the stiffness matrix can be written as:

$$\underset{\sim}{\mathbb{K}} = \int_{\text{section}} \int_{-1}^{1} \underset{\sim}{B}^T \underset{\sim}{D} \underset{\sim}{B} \, \mathrm{d}x \, \mathrm{d}(\text{section})$$

or

$$\underset{\sim}{\mathbb{K}} = \frac{L}{2} \int_{\text{section}} \left[\int_{-1}^{1} \underset{\sim}{B_\varepsilon}^T E_t \underset{\sim}{B_\varepsilon} \, \mathrm{d}\zeta + \int_{-1}^{1} \underset{\sim}{B_\gamma}^T G_t \underset{\sim}{B_\gamma} \, \mathrm{d}\zeta \right] \mathrm{d}(\text{section}) \tag{4.55}$$

Evaluate the integrals using midpoint integration to avoid shear locking, the stiffness matrix is found to be:

$$\underset{\sim}{\mathbb{K}} = \left[\begin{array}{cccc} \frac{G_t A}{L} & \frac{G_t A}{2} & \frac{-G_t A}{L} & \frac{G_t A}{2} \\ \frac{G_t A}{2} & \frac{G_t A L}{4} + \frac{E_t I}{L} & \frac{G_t A}{2} & \frac{G_t A L}{4} - \frac{E_t I}{L} \\ \frac{-G_t A}{L} & \frac{-G_t A}{2} & \frac{G_t A}{L} & \frac{-G_t A}{2} \\ \frac{G_t A}{2} & \frac{G_t A L}{4} - \frac{E_t I}{L} & \frac{-G_t A}{2} & \frac{G_t A L}{4} + \frac{E_t I}{L} \end{array} \right] \tag{4.56}$$

with the consistent mass matrix given by:

$$\underset{\sim}{\mathbb{M}} = \frac{\rho L}{6} \cdot \left[\begin{array}{cccc} 2A & 0 & A & 0 \\ 0 & 2I & 0 & I \\ A & 0 & 2A & 0 \\ 0 & I & 0 & 2I \end{array} \right] \tag{4.57}$$

4.1.5 Closed-Form Solution for a Laterally Loaded Pile in a Homogeneous Soil Layer and Validation

Validation of the 2D-2DOF soil element will first be carried out by comparison with the available solution by Novak and Nogami (1977). This approximate, yet closed-form, solution for a vibrating pile in a homogeneous soil layer overlying a rigid bedrock is established by assuming that the vertical soil displacement is negligible. The solution is limited to purely-elastic behavior, harmonic motion, and perfect soil-pile interface "bonding". For the soil slice, the equations governing viscoelastic response are given by:

$$\begin{aligned}(\lambda+2G)\frac{\partial}{\partial r}(\Delta e^{i\omega t})-\frac{2G}{r}\frac{\partial}{\partial\theta}(\omega_z e^{i\omega t}) &= \rho\frac{\partial^2}{\partial t^2}(ue^{i\omega t})-G\frac{\partial^2}{\partial z^2}(ue^{i\omega t})\\ (\lambda+2G)\frac{\partial}{r\partial\theta}(\Delta e^{i\omega t})+2G\frac{\partial}{\partial r}(\omega_z e^{i\omega t}) &= \rho\frac{\partial^2}{\partial t^2}(ve^{i\omega t})-G\frac{\partial^2}{\partial z^2}(ve^{i\omega t})\end{aligned} \tag{4.58}$$

where:

$$\begin{aligned}\Delta &= \frac{1}{r}\frac{\partial}{\partial r}(ru)+\frac{1}{r}\frac{\partial v}{\partial\theta}\\ \omega_z &= \frac{1}{2r}\left[\frac{\partial}{\partial r}(rv)-\frac{\partial u}{\partial\theta}\right]\end{aligned} \tag{4.59}$$

The two stress components contributing to the force acting on the pile are σ_r and $\tau_{r\theta}$. At any location along the pile, the resultant force (per unit length), $p(z)$, can be computed by

$$p(z)=-\int_0^{2\pi}[\sigma_r(r_0,z)cos(\theta)-\tau_{r\theta}(r_0,z)sin(\theta)]r_0d\theta \tag{4.60}$$

Solving the governing differential equation for u and v, as explained in-detail in Novak and Nogami (1977), the expressions for σ_r and $\tau_{r\theta}$ are obtained and the soil resistance can be rewritten as a function of the horizontal resistant factor, α_{hn}, and the pile displacement. Note that the pile displacement at any z location can be taken equal to the summation of the vibration modes of the free-standing pile:

$$p(z) = \sum_{n=1}^{\infty} \alpha_{hn} U_n sin(h_n z) \tag{4.61}$$

where $h_n = (\pi/2H)(2n-1), n = 1, 2, 3, ...$ H = depth of a layer, and the soil resistant factor, α_{hn}, is

$$\alpha_{hn} = \pi r_0 \mu \Big[h_n^2 - \Big(\frac{\omega}{c_s}\Big)^2 \Big] T_n \tag{4.62}$$

with

$$T_n = \frac{4K_1(q_n\, r_0)K_1(s_n\, r_0) + s_n r_0 K_1(q_n\, r_0)K_0(s_n\, r_0) + q_n r_0 K_0(q_n\, r_0)K_1(s_n\, r_0)}{q_n K_0(q_n\, r_0)K_1(s_n\, r_0) + s_n K_1(q_n\, r_0)K_0(s_n\, r_0) + q_n s_n r_0 K_0(q_n\, r_0)K_0(s_n\, r_0)} \tag{4.63}$$

$$\begin{aligned} q_n^2 &= \frac{1}{\eta^2}\Big[h_n^2 - \Big(\frac{\omega}{c_s}\Big)^2\Big] \\ s_n^2 &= h_n^2 - \Big(\frac{\omega}{c_s}\Big)^2 \\ \eta &= \sqrt{\frac{2(1-\nu)}{1-2\nu}} \\ (i &= \sqrt{-1}) \end{aligned} \tag{4.64}$$

Next, the governing differential equation for dynamics of an Euler-beam representation of the laterally vibrating pile is expressed as follows:

$$E_p I \frac{\partial^4}{\partial z^4}(u\, e^{i\omega t}) + m \frac{\partial^2}{\partial t^2}(u\, e^{i\omega t}) = -p(z)(u\, e^{i\omega t}) \tag{4.65}$$

The plot in Figure 4.4 exhibits the horizontal complex stiffness at the pile head versus the dimensionless frequency with the solid line and dashed-line representing the real and imaginary parts of the dimensionless stiffness ($K_{\text{horizontal}} \cdot R_0^3/EI$), respectively. In the case analyzed, the slenderness ratio of the pile, H/r_0, is 50, the soil Poisson's ratio, the soil-to-pile mass density ratio, and the ratio of soil shear modulus to pile elastic modulus are taken as 0.25, 0.6, and 0.00054, respectively.

Now, the comparison of results for the problem analyzed for the dimensionless stiffness magnitude by the closed-form solution, 2D-2DOF FE result, and 3-D FE solution (Tassoulas 1981), denoted by thick line, triangular mark-

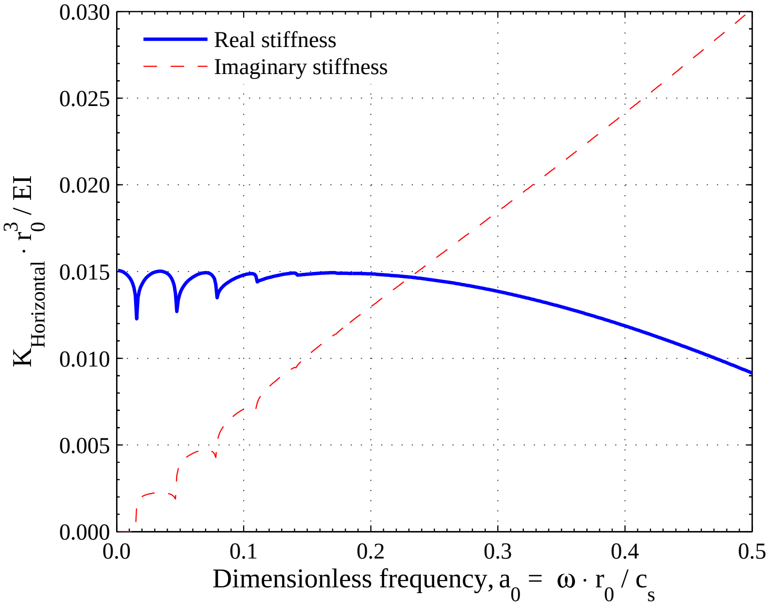

Figure 4.4: Horizontal dimensionless complex stiffness of the pile-head versus dimensionless frequency.

ers, and dotted-line, respectively, can be seen in Figure 4.5. The agreement is excellent over a wide range of dimensionless frequency. The phase of the dimensionless displacement response from 2D-2DOF FE analysis agrees very well with that from the closed-form solution by Novak and Nogami (1977) as shown in pile-head horizontal-dimensionless-displacement-versus-time plots in Figures 4.6 to 4.11.

Since the soil displacement in the z direction is assumed to be zero in the 2D-2DOF ring element, the validity of this assumption against the complete three-dimensional finite-element solution must be examined. The formulation of the 2D-3DOF ring element and the result comparison of results will be given next.

4.2 Complete Three-Dimensional Ring Finite Element

4.2.1 Stiffness Matrix

The 2D-3DOF soil model of the laterally-loaded pile includes two components, assumed to be negligible in the 2D-2DOF FE model: the soil vertical displacement and rotational resistance along the pile due to the vertical motion of the adjacent soil. Inclusion of these components more then doubles the bandwidth of the resulting system of equations (in comparison with the 2D-2DOF ring element). This significant increase in computational effort will be taken into consideration for the selection of the appropriate model for laterally-loaded pile analysis.

The variation of the displacements of the soil with respect to r, θ, z,

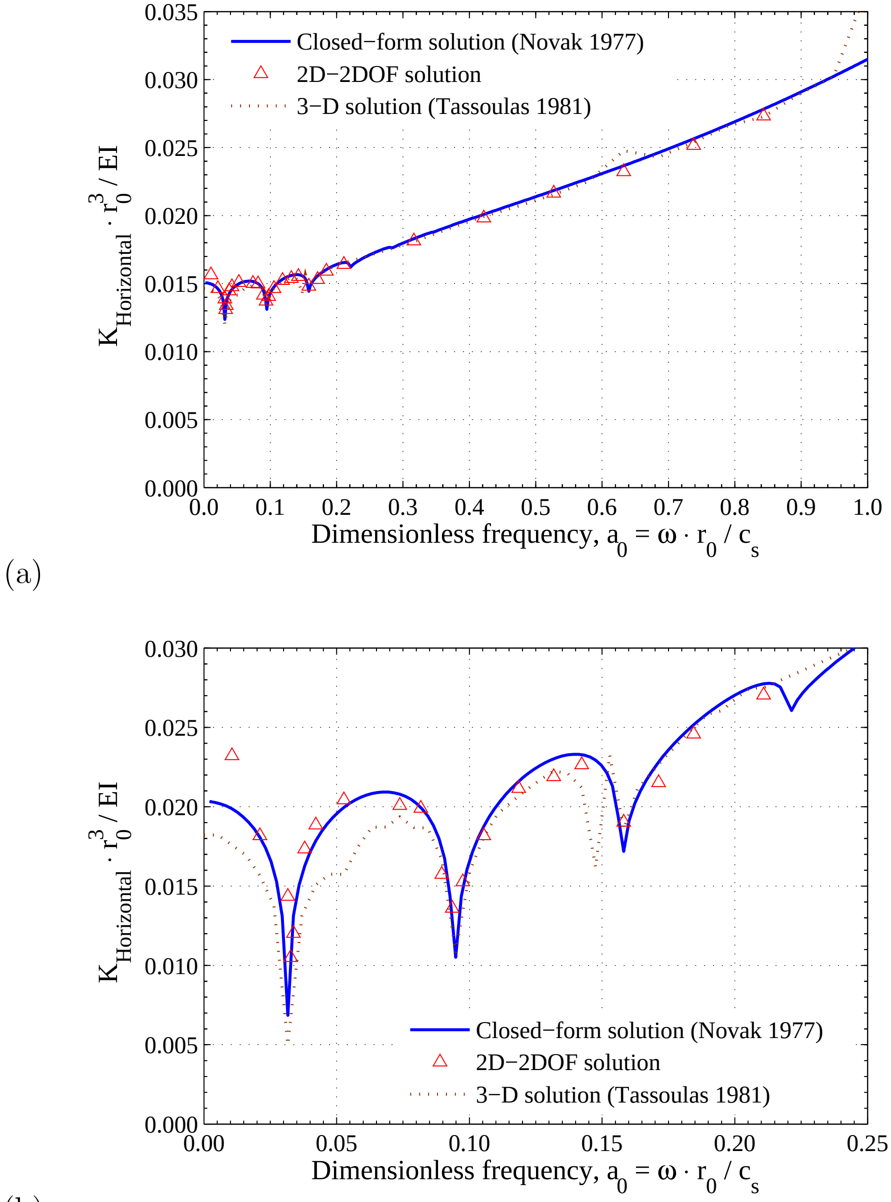

Figure 4.5: Dimensionless stiffness magnitude versus dimensionless frequency.

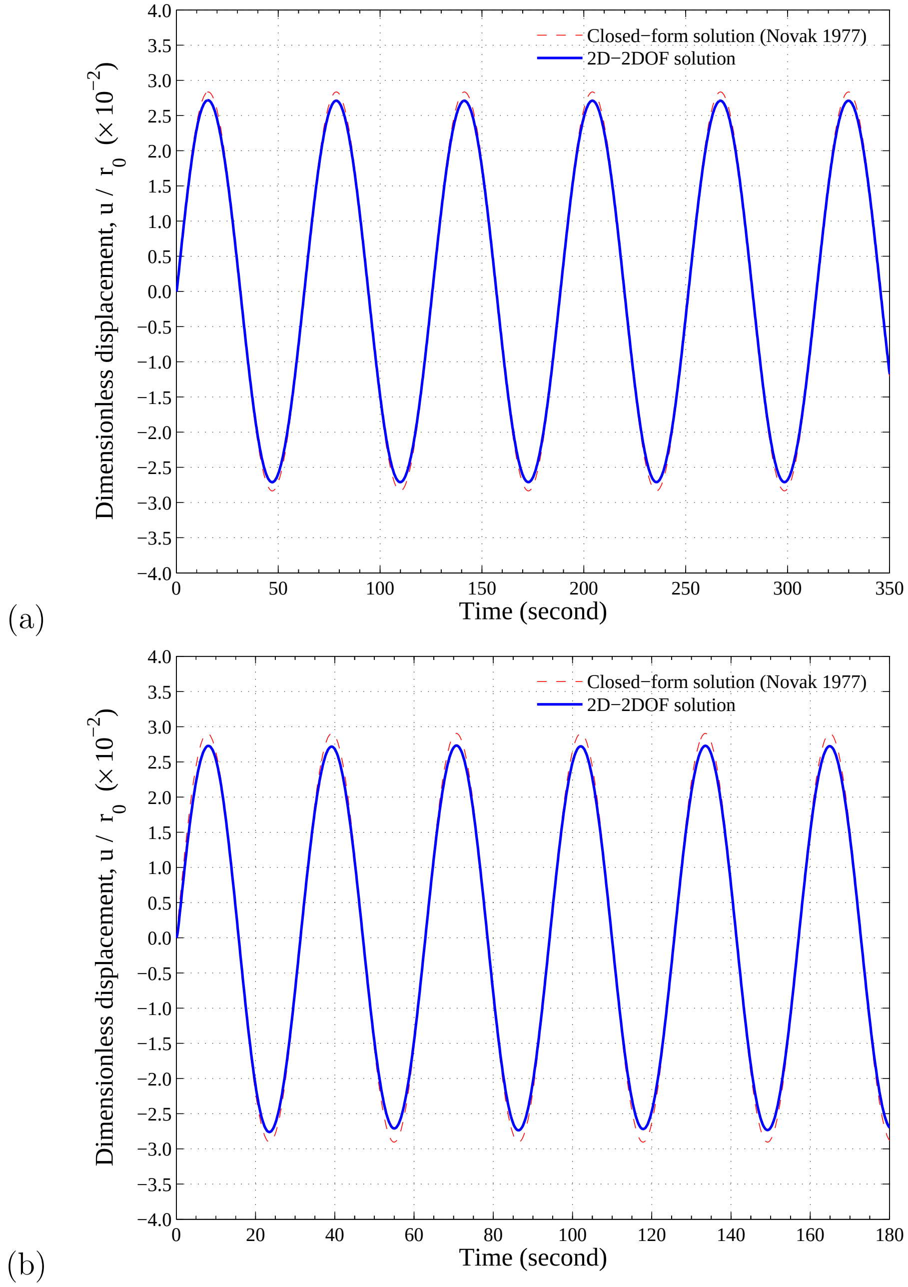

Figure 4.6: Dimensionless displacement versus time: (a) $a_0 = 0.1$ (b) $a_0 = 0.2$. ($a_0 = \omega \cdot r_0/c_s$)

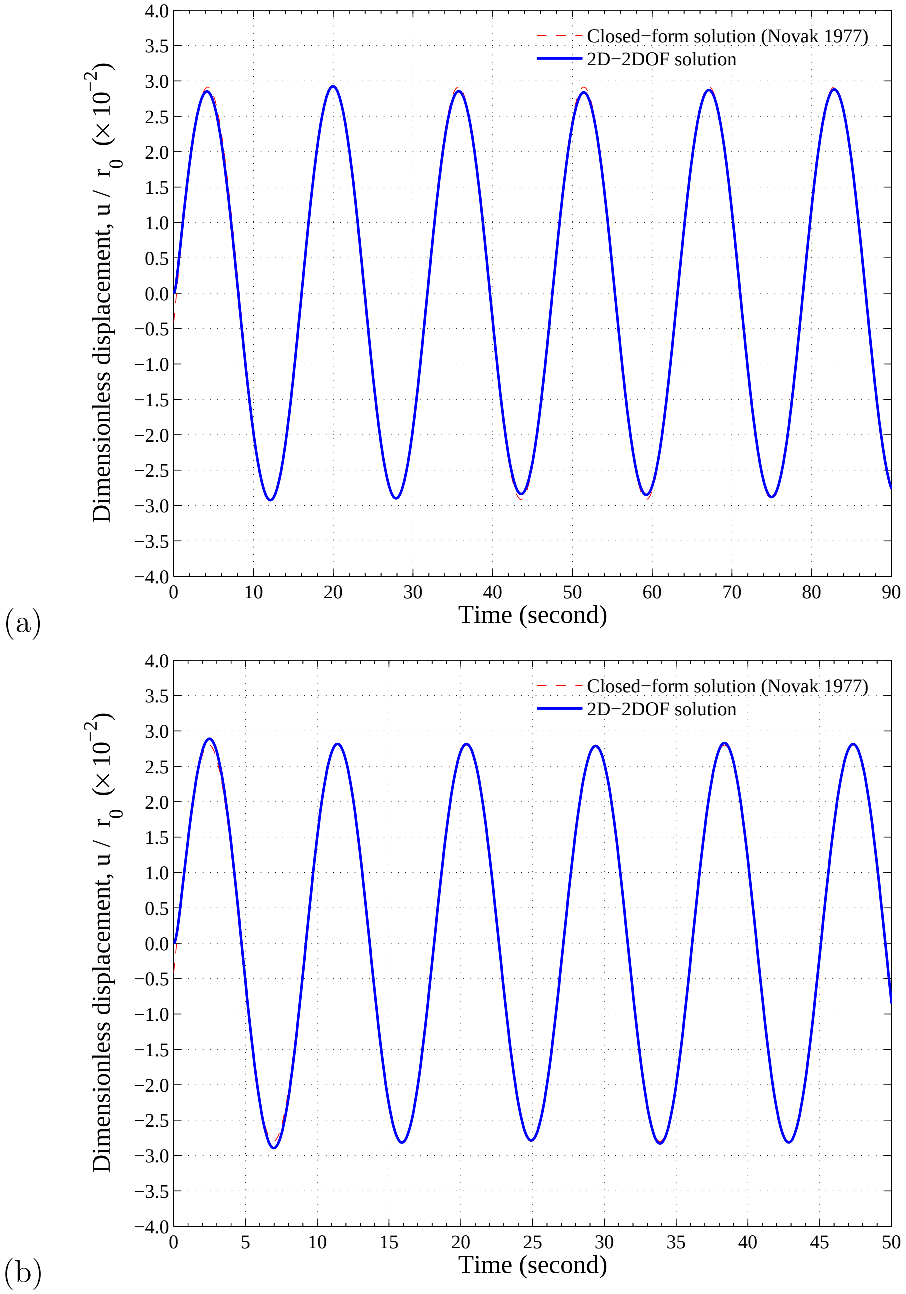

Figure 4.7: Dimensionless displacement versus time: (a) $a_0 = 0.4$ (b) $a_0 = 0.7$. ($a_0 = \omega \cdot r_0/c_s$)

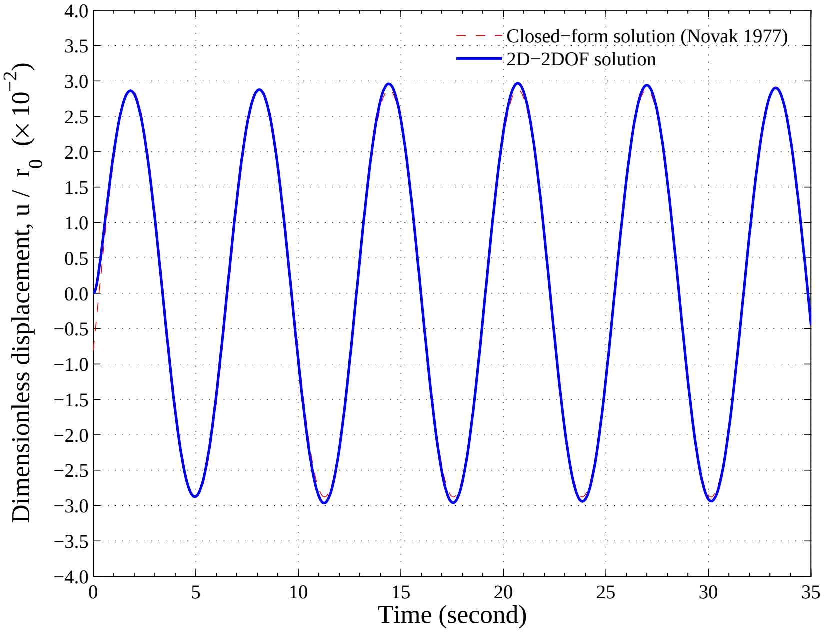

(a)

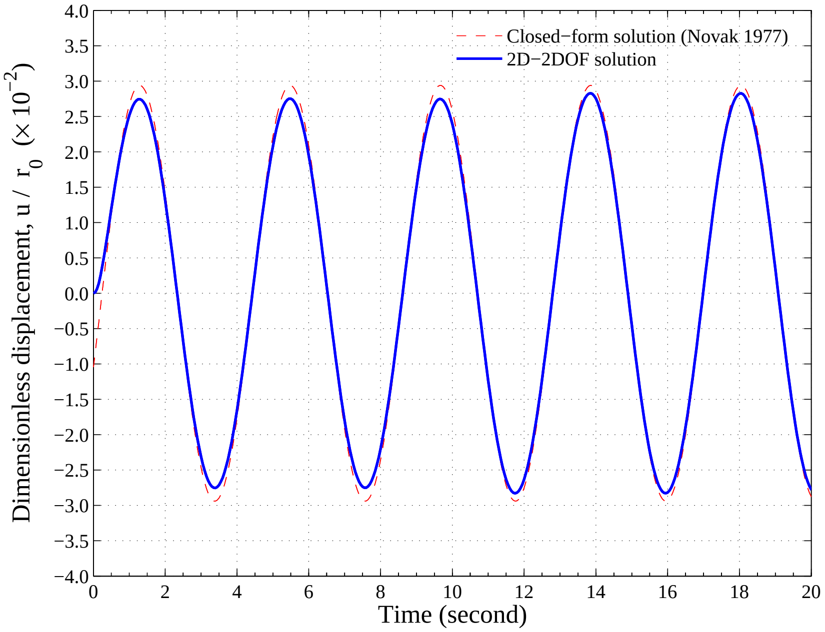

(b)

Figure 4.8: Dimensionless displacement versus time: (a) $a_0 = 1.0$ (b) $a_0 = 1.5$. ($a_0 = \omega \cdot r_0/c_s$)

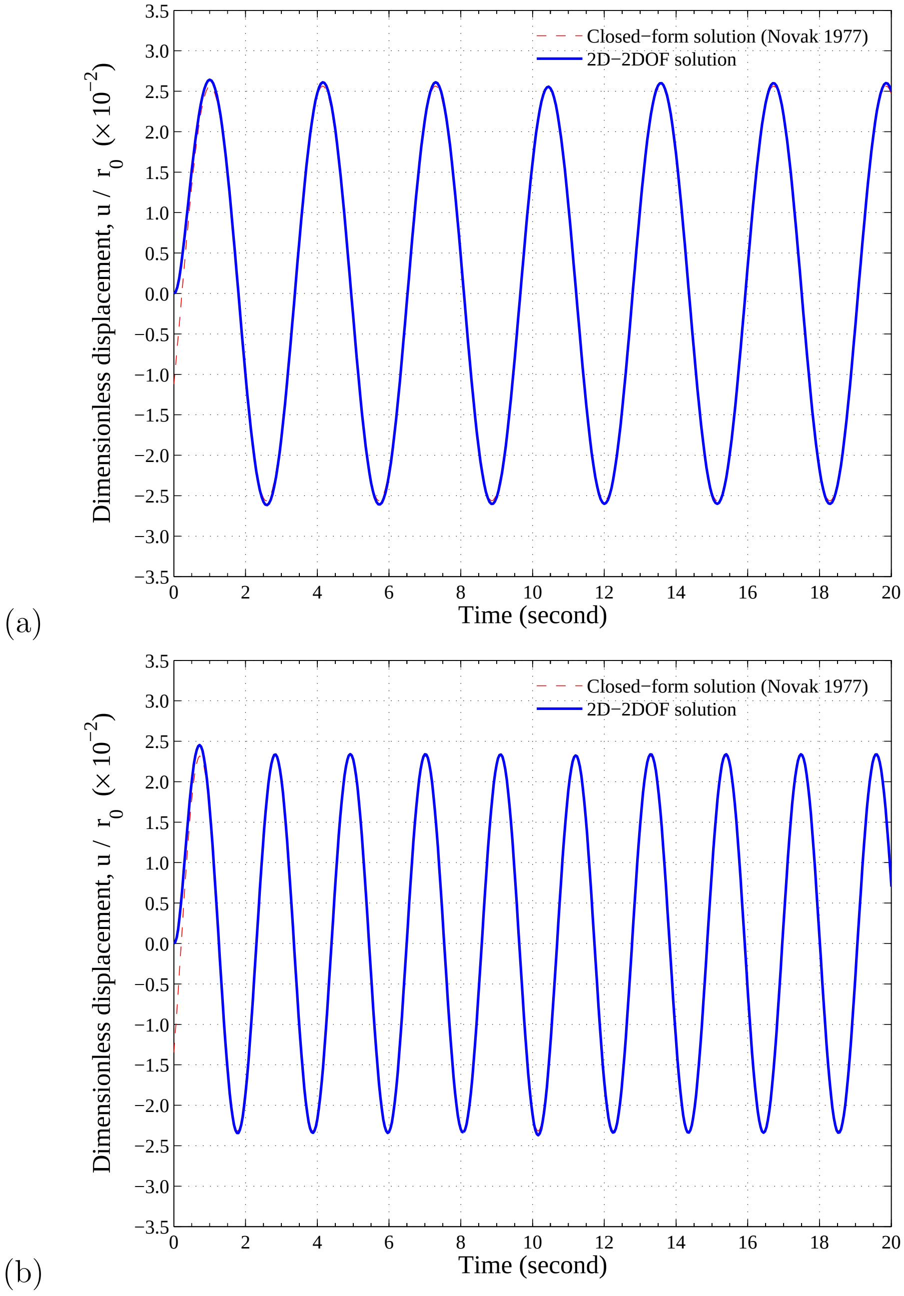

Figure 4.9: Dimensionless displacement versus time: (a) $a_0 = 2.0$ (b) $a_0 = 3.0$. ($a_0 = \omega \cdot r_0/c_s$)

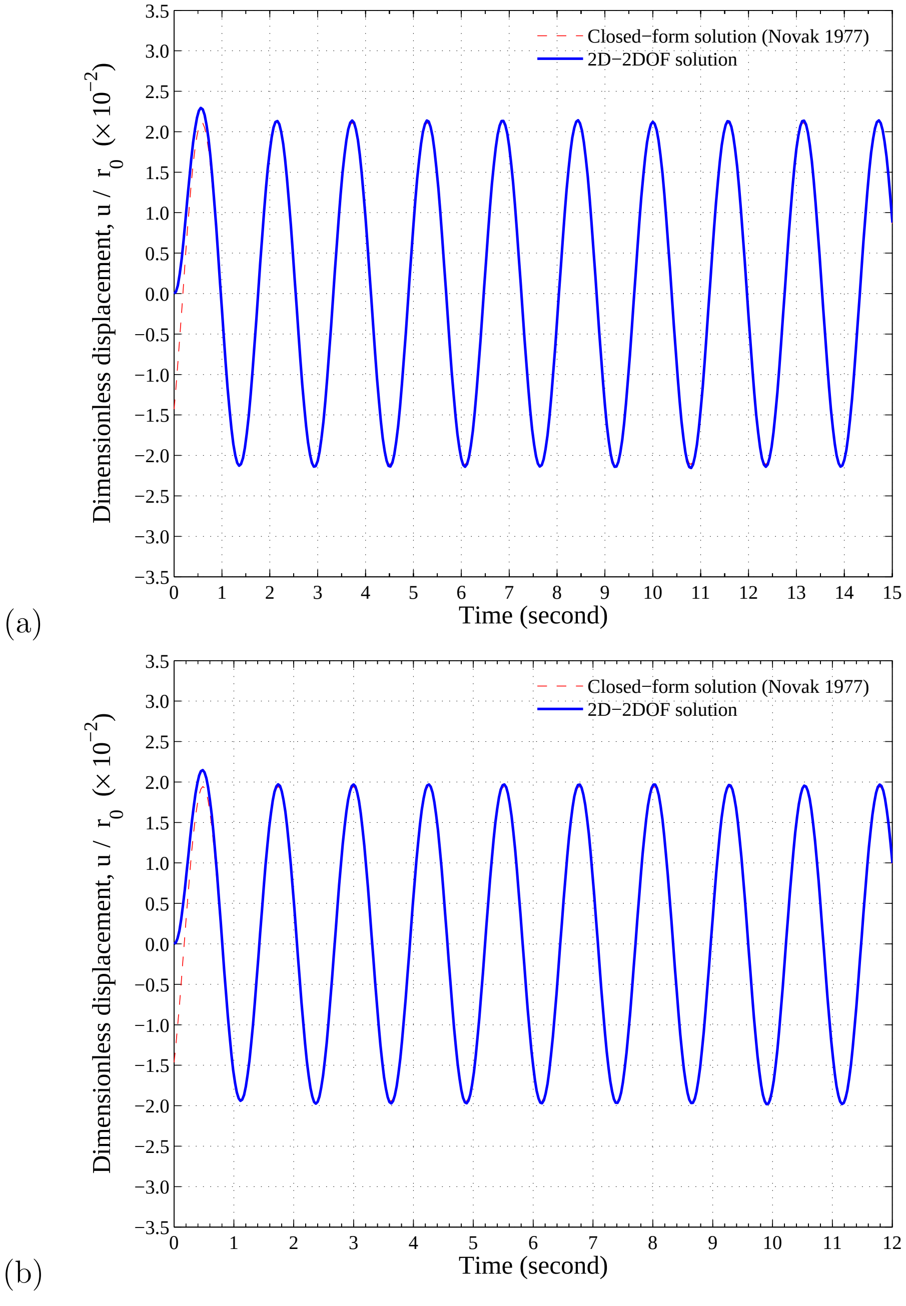

Figure 4.10: Dimensionless displacement versus time: (a) $a_0 = 4.0$ (b) $a_0 = 5.0$. ($a_0 = \omega \cdot r_0/c_s$)

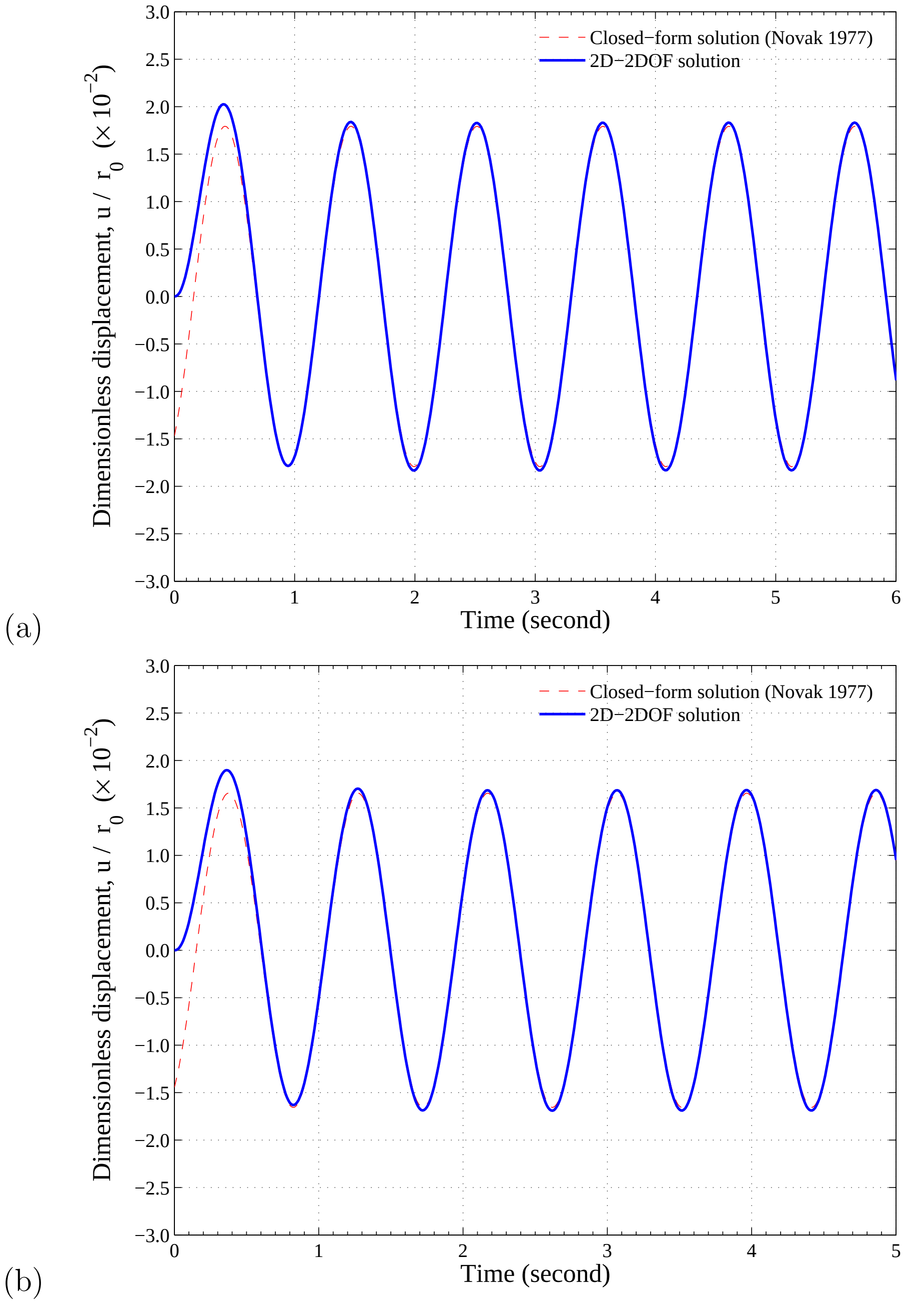

Figure 4.11: Dimensionless displacement versus time: (a) $a_0 = 6.0$ (b) $a_0 = 7.0$. ($a_0 = \omega \cdot r_0/c_s$)

and t, if the assumption of purely-elastic behavior holds, is given by:

$$u(r,\theta,z,t) = U(r,z,t)\cdot\cos(\theta) \tag{4.66}$$

$$v(r,\theta,z,t) = -V(r,z,t)\cdot\sin(\theta) \tag{4.67}$$

$$w(r,\theta,z,t) = W(r,z,t)\cdot\cos(\theta) \tag{4.68}$$

Next, the strain components can be calculated from the displacements in Equations 4.66, 4.67, and 4.68 as follows:

$$\begin{aligned} \varepsilon_r &= \frac{\partial u}{\partial r} \\ &= \frac{\partial U}{\partial r}\cdot\cos(\theta) \end{aligned} \tag{4.69}$$

$$\begin{aligned} \varepsilon_\theta &= \frac{u}{r}+\frac{1}{r}\frac{\partial v}{\partial\theta} \\ &= \frac{U}{r}\cdot\cos(\theta)-\frac{V}{r}\cdot\cos(\theta) \\ &= \frac{U-V}{r}\cdot\cos(\theta) \end{aligned} \tag{4.70}$$

$$\varepsilon_z = \frac{\partial w}{\partial z} = \frac{\partial W}{\partial z}\cdot\cos(\theta) \tag{4.71}$$

$$\begin{aligned} \gamma_{r\theta} &= \frac{\partial v}{\partial r}-\frac{v}{r}+\frac{1}{r}\frac{\partial u}{\partial\theta} \\ &= -\frac{\mathrm{d}V}{r}\cdot\sin(\theta)+\frac{V}{r}\cdot\sin(\theta)-\frac{U}{r}\cdot\sin(\theta) \\ &= -\left(\frac{\mathrm{d}V}{\mathrm{d}r}+\frac{U-V}{r}\right)\cdot\sin(\theta) \end{aligned} \tag{4.72}$$

$$\begin{aligned} \gamma_{rz} &= \frac{\partial w}{\partial r}+\frac{\partial u}{\partial z} \\ &= \left(\frac{\partial W}{\partial r}+\frac{\partial U}{\partial z}\right)\cdot\cos(\theta) \end{aligned} \tag{4.73}$$

$$\begin{aligned} \gamma_{z\theta} &= \frac{1}{r}\cdot\frac{\partial w}{\partial\theta}+\frac{\partial v}{\partial z} \\ &= -\left(\frac{\partial V}{\partial z}+\frac{\partial V}{\partial z}\right)\cdot\sin(\theta) \end{aligned} \tag{4.74}$$

Now, the variations of displacements can be approximated in terms of

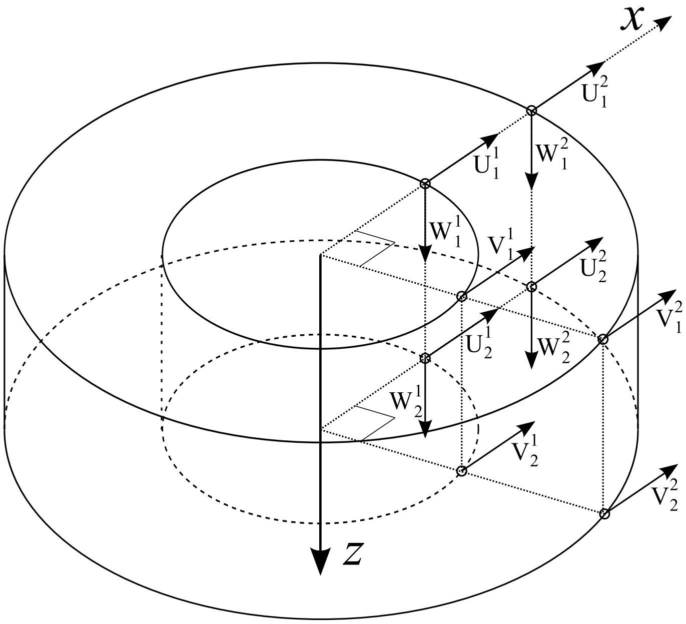

Figure 4.12: 1-D element representation of three-dimensional soil.

nodal values and interpolation functions. With ζ and η as the local coordinates in radial and vertical directions, as shown in Figure 4.12, the displacement approximations can be written as:

$$u(r,\theta,z,t) \approxeq \sum_{m=1}^{2}\sum_{n=1}^{2} U_n^m(t)\cdot\Psi_m(\zeta)\cdot\Phi_n(\eta) \tag{4.75}$$

$$v(r,\theta,z,t) \approxeq \sum_{m=1}^{2}\sum_{n=1}^{2} V_n^m(t)\cdot\Psi_m(\zeta)\cdot\Phi_n(\eta) \tag{4.76}$$

$$w(r,\theta,z,t) \approxeq \sum_{m=1}^{2}\sum_{n=1}^{2} W_n^m(t)\cdot\Psi_m(\zeta)\cdot\Phi_n(\eta) \tag{4.77}$$

The interpolation functions and their derivatives resemble those for the 2D-2DOF ring element formulation and the strain components can be expressed as:

$$\varepsilon_r = \sum_{m=1}^{2}\sum_{n=1}^{2}\left[U_n^m \cdot \frac{\mathrm{d}\Psi_m(\zeta)}{\mathrm{d}r} \cdot \Phi_n(\eta)\right] \cdot \cos(\theta) \tag{4.78}$$

$$\varepsilon_\theta = \sum_{m=1}^{2}\sum_{n=1}^{2}\left[\frac{U_n^m - V_n^m}{r} \cdot \Psi_m(\zeta) \cdot \Phi_n(\eta)\right] \cdot \cos(\theta) \tag{4.79}$$

$$\varepsilon_z = \sum_{m=1}^{2}\sum_{n=1}^{2}\left[W_n^m \Psi_m \frac{\mathrm{d}\Phi_n}{\mathrm{d}z}\right] \cdot \cos(\theta) \tag{4.80}$$

$$\gamma_{r\theta} = \sum_{m=1}^{2}\sum_{n=1}^{2}\left[U_n^m \Phi_n(\eta) \frac{\Psi_m(\zeta)}{r} + V_n^m \cdot \Phi_n(\eta) \cdot \left(\frac{\mathrm{d}\Psi_m(\zeta)}{\mathrm{d}r} - \frac{\Psi_m(\zeta)}{r}\right)\right] \cdot [-\sin(\theta)] \tag{4.81}$$

$$\gamma_{rz} = \sum_{m=1}^{2}\sum_{n=1}^{2}\left[U_n^m \Psi_m(\zeta) \frac{\mathrm{d}\Phi_n(\eta)}{\mathrm{d}z} + W_n^m \Phi_n(\eta) \frac{\mathrm{d}\Psi_m(\zeta)}{\mathrm{d}r}\right] \cdot (\cos(\theta)) \tag{4.82}$$

$$\gamma_{z\theta} = \sum_{m=1}^{2}\sum_{n=1}^{2}\left(V_n^m \Psi_m(\zeta) \frac{\mathrm{d}\Phi_n(\eta)}{\mathrm{d}z} + \frac{W_n^m}{r} \cdot \Psi_m(\zeta)\Phi_n(\eta)\right) \cdot (-\sin(\theta)) \tag{4.83}$$

Since the integration of elastic stress variations in angular direction is carried out and equal to the constant factor, π, the strain column vector can be expressed in matrix form as:

$$\underset{\sim}{\varepsilon} = \underset{\sim}{B}\underset{\sim}{U} \tag{4.84}$$

where

$$\underset{\sim}{U} = \begin{bmatrix} U_1^1 & V_1^1 & W_1^1 & U_1^2 & V_1^2 & W_1^2 & U_2^1 & V_2^1 & W_2^1 & U_2^2 & V_2^2 & W_2^2 \end{bmatrix}^T \tag{4.85}$$

$$\underset{\sim}{B} = \begin{bmatrix} \chi_{11} & 0 & 0 & \chi_{12} & 0 & 0 & \chi_{21} & 0 & 0 & \chi_{22} & 0 & 0 \\ \beta_{11} & -\beta_{11} & 0 & \beta_{12} & -\beta_{12} & 0 & \beta_{21} & -\beta_{21} & 0 & \beta_{22} & -\beta_{22} & 0 \\ 0 & 0 & \psi_{11} & 0 & 0 & \psi_{12} & 0 & 0 & \psi_{21} & 0 & 0 & \psi_{22} \\ \beta_{11} & \alpha_{11} & 0 & \beta_{12} & \alpha_{12} & 0 & \beta_{21} & \alpha_{21} & 0 & \beta_{22} & \alpha_{22} & 0 \\ \psi_{11} & 0 & \kappa_{11} & \psi_{12} & 0 & \kappa_{12} & \psi_{21} & 0 & \kappa_{21} & \psi_{22} & 0 & \kappa_{22} \\ 0 & \psi_{11} & \beta_{11} & 0 & \psi_{12} & \beta_{12} & 0 & \psi_{21} & \beta_{21} & 0 & \psi_{22} & \beta_{22} \end{bmatrix} \tag{4.86}$$

and

$$\begin{aligned}
\chi_{pq} &= \Phi_q(\eta) \cdot \frac{\mathrm{d}\Psi_p(\zeta)}{\mathrm{d}r} \\
&= \Phi_q(\eta) \cdot \frac{\mathrm{d}\Psi_p(\zeta)}{\mathrm{d}\zeta} \cdot \frac{\mathrm{d}\zeta}{\mathrm{d}r} \\
&= \Phi_q(\eta) \cdot \frac{\mathrm{d}\Psi_p(\zeta)}{\mathrm{d}\zeta} \cdot \frac{2}{\Delta r} && (4.87) \\
\beta_{pq} &= \frac{\Psi_p(\zeta) \cdot \Phi_q(\eta)}{r} && (4.88) \\
\alpha_{pq} &= \Phi_q(\eta) \left(\frac{\mathrm{d}\Psi_p(\zeta)}{\mathrm{d}r} - \frac{\Psi_p(\zeta)}{r} \right) \\
&= \Phi_q(\eta) \left(\frac{\mathrm{d}\Psi_p(\zeta)}{\mathrm{d}\zeta} \cdot \frac{\mathrm{d}\zeta}{\mathrm{d}r} - \frac{\Psi_p(\zeta)}{r} \right) \\
&= \Phi_q(\eta) \left(\frac{\mathrm{d}\Psi_p(\zeta)}{\mathrm{d}\zeta} \cdot \frac{2}{\Delta r} - \frac{\Psi_p(\zeta)}{r} \right) && (4.89) \\
\psi_{pq} &= \Psi_p(\zeta) \frac{\mathrm{d}\Phi_q(\eta)}{\mathrm{d}z} \\
&= \Psi_p(\zeta) \frac{\mathrm{d}\Phi_q(\eta)}{\mathrm{d}\eta} \cdot \frac{\mathrm{d}\eta}{\mathrm{d}z} \\
&= -\Psi_p(\zeta) \frac{\mathrm{d}\Phi_q(\eta)}{\mathrm{d}z} \cdot \frac{2}{\Delta z} && (4.90)
\end{aligned}$$

4.2.2 Material Inelasticity

Since the 2D-2DOF formulation take into account all stress components required for complete 2D-3DOF inelastic analysis, identical treatment of material inelasticity will be applied to the 2D-3DOF ring element.

4.2.3 Mass Matrix

The mass matrix is obtained in the same manner as for the 2D-2DOF ring element but there are 4 additional rows and columns corresponding to the displacements in the z direction. The mass matrix for 2D-3DOF element is given by:

$$\begin{bmatrix}
2\mathbb{m}_1 & 0 & 0 & \mathbb{m}_1 & 0 & 0 & 2\mathbb{m}_2 & 0 & 0 & \mathbb{m}_2 & 0 & 0 \\
0 & 2\mathbb{m}_1 & 0 & 0 & \mathbb{m}_1 & 0 & 0 & 2\mathbb{m}_2 & 0 & 0 & \mathbb{m}_2 & 0 \\
0 & 0 & 2\mathbb{m}_1 & 0 & 0 & \mathbb{m}_1 & 0 & 0 & 2\mathbb{m}_2 & 0 & 0 & \mathbb{m}_2 \\
\mathbb{m}_1 & 0 & 0 & 2\mathbb{m}_1 & 0 & 0 & \mathbb{m}_2 & 0 & 0 & 2\mathbb{m}_2 & 0 & 0 \\
0 & \mathbb{m}_1 & 0 & 0 & 2\mathbb{m}_1 & 0 & 0 & \mathbb{m}_2 & 0 & 0 & 2\mathbb{m}_2 & 0 \\
0 & 0 & \mathbb{m}_1 & 0 & 0 & 2\mathbb{m}_1 & 0 & 0 & \mathbb{m}_2 & 0 & 0 & 2\mathbb{m}_2 \\
2\mathbb{m}_2 & 0 & 0 & \mathbb{m}_2 & 0 & 0 & 2\mathbb{m}_3 & 0 & 0 & \mathbb{m}_3 & 0 & 0 \\
0 & 2\mathbb{m}_2 & 0 & 0 & \mathbb{m}_2 & 0 & 0 & 2\mathbb{m}_3 & 0 & 0 & \mathbb{m}_3 & 0 \\
0 & 0 & 2\mathbb{m}_2 & 0 & 0 & \mathbb{m}_2 & 0 & 0 & 2\mathbb{m}_3 & 0 & 0 & \mathbb{m}_3 \\
\mathbb{m}_2 & 0 & 0 & 2\mathbb{m}_2 & 0 & 0 & \mathbb{m}_3 & 0 & 0 & 2\mathbb{m}_3 & 0 & 0 \\
0 & \mathbb{m}_2 & 0 & 0 & 2\mathbb{m}_2 & 0 & 0 & \mathbb{m}_3 & 0 & 0 & 2\mathbb{m}_3 & 0 \\
0 & 0 & \mathbb{m}_2 & 0 & 0 & 2\mathbb{m}_2 & 0 & 0 & \mathbb{m}_3 & 0 & 0 & 2\mathbb{m}_3
\end{bmatrix} \tag{4.91}$$

where

$$\begin{aligned}
\mathbb{m}_1 &= \left(\frac{\pi \cdot \Delta z \cdot \Delta r \cdot \rho}{36}\right) \cdot \left(2r_i + \frac{\Delta r}{2}\right) \\
\mathbb{m}_2 &= \left(\frac{\pi \cdot \Delta z \cdot \Delta r \cdot \rho}{36}\right) \cdot \left(r_i + \frac{\Delta r}{2}\right) \\
\mathbb{m}_3 &= \left(\frac{\pi \cdot \Delta z \cdot \Delta r \cdot \rho}{36}\right) \cdot \left(2r_i + \frac{3\Delta r}{2}\right)
\end{aligned} \tag{4.92}$$

4.2.4 Pile-Soil Element Connectivities

Since the 2D-3DOF element also accounts for the soil vertical displacement, the relationship between the displacement in the z direction and pile rotation will be included assuming that there is no pile-soil slippage. The coupling element for pile-soil displacement is identical to those presented in Chapter 3. A detailed description of pile rotation-soil vertical displacement coupling is provided below:

Referring to Figure 4.13, consider, at a particular depth z, the rotation of the pile, the vertical displacement at the surface of the pile (at $\theta = 0$), the external moment on the pile, and the vertical force on the pile (at $\theta = 0$), denoted by θ, w, M, and Z, respectively. The moment equilibrium equation and rotation-displacement relationship can be expressed as follows:

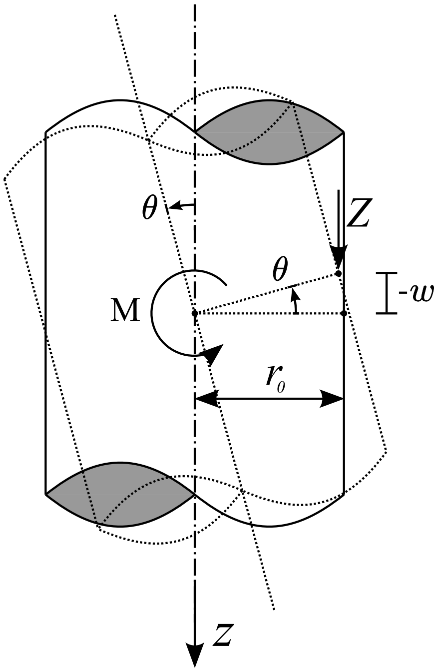

Figure 4.13: Pile rotation-soil vertical displacement and moment-force relationship.

$$\theta \cdot r_0 = -w \tag{4.93}$$

$$M - Z \cdot r_0 = 0 \tag{4.94}$$

The relationship in Equation 4.94 can be cast in matrix form as:

$$\begin{bmatrix} 0 & 0 & -1 & 0 \\ 0 & 0 & 0 & -1 \\ r & 1 & 0 & 0 \\ 0 & 0 & 1 & -r \end{bmatrix} \begin{bmatrix} \theta \\ w \\ M \\ Z \end{bmatrix} = \begin{bmatrix} -M \\ -Z \\ 0 \\ 0 \end{bmatrix} \tag{4.95}$$

The constraints (Equation 4.95) can be introduced to the nonlinear dynamic equations as follows:

$$\begin{aligned} \mathrm{LHS}_{\theta^P} \cdot (\Delta U - \Delta U_0)_{\theta^P} - \mathbb{R} &= \mathrm{RHS}^*_{\theta^P} \\ \mathrm{LHS}_{w^S} \cdot (\Delta U - \Delta U_0)_{w^S} - Z &= \mathrm{RHS}^*_{w^S} \\ \theta \cdot r_0 + w &= 0 \\ M - Z \cdot r_0 &= 0 \end{aligned} \tag{4.96}$$

where the expression for $\mathbf{RHS}^*$ was given in Equation 3.68.

4.2.5 Validation

The results from the laterally-loaded pile analyzed with the 2D-2DOF ring element and the 2D-3DOF ring element will be validated by comparison with the 3-dimensional FE solution (Tassoulas 1981) and the Novak approximate closed-form solution (1977). The pile-soil parameters in the analysis are given as follows:

$$\begin{aligned} \nu_{\text{soil}} &: 0.25 \quad , \quad \nu_{\text{pile}} : 0.25 \\ \rho_{\text{soil}} &: 0.60 \quad , \quad \rho_{\text{pile}} : 1.00 \\ G_{\text{soil}} &: 54 \quad , \quad G_{\text{pile}} : 100,000 \\ \text{Pile radius} &: 1 \end{aligned}$$

4.2.5.1 Validation Problem 1

The pile is 10.0 unit long (slenderness ratio, $l/r_0 = 10.0$) and clamped at the tip. Note that the 3-D FE model (Tassoulas 1981) was constructed exclusively for the problem with underlying rigid bed rock (no displacement allowed at the bottom). Thus, the pile tip is constrained against displacement and rotation as shown in Figure 4.14. The dimensionless stiffness magnitude versus dimensionless frequency plot in Figure 4.15 for the FE solutions based on the 2D-3DOF ring element are in excellent agreement validating the correctness of the model, used as reference solutions in the following validation problems.

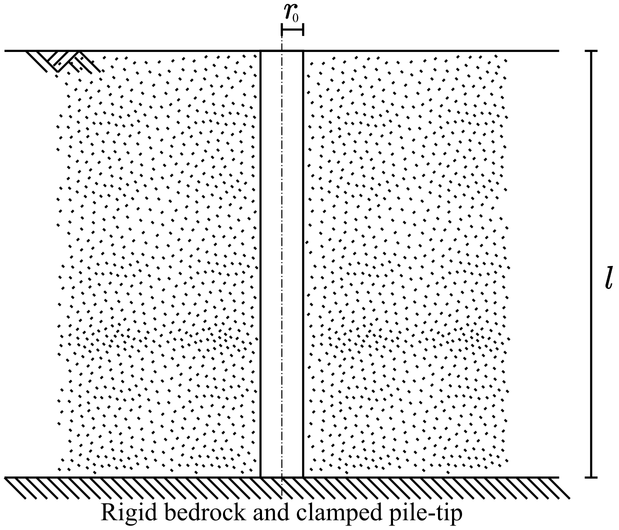

Figure 4.14: Pile configuration for Validation Problem 1.

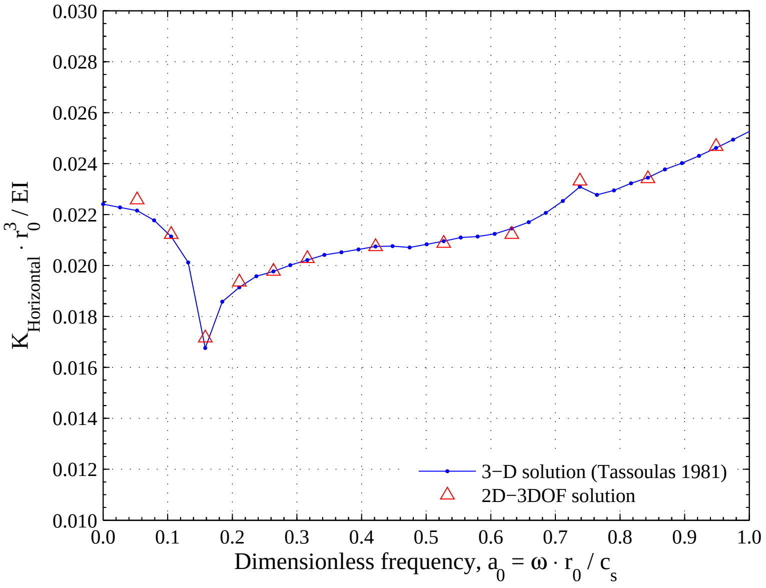

Figure 4.15: Dimensionless pile-head stiffness magnitude versus dimensionless frequency.

4.2.5.2 Validation Problem 2

Next, the pinned-tip pile model with $l/r_0 = 10.0$, illustrated in Figure 4.16, is analyzed by the 2D-2DOF ring model and the 2D-3DOF ring model. The calculated dimensionless pile-head stiffnesses versus dimensionless frequency are presented in Figure 4.17 (a). In order to allow more contribution from soil resistance, the boundary condition at pile tip is set as a pinned-support allowing more resistance contributed by the surrounding soil since the clamped-tip pile behaves like a cantilever beam and the resistance is mainly provided by the pile itself.

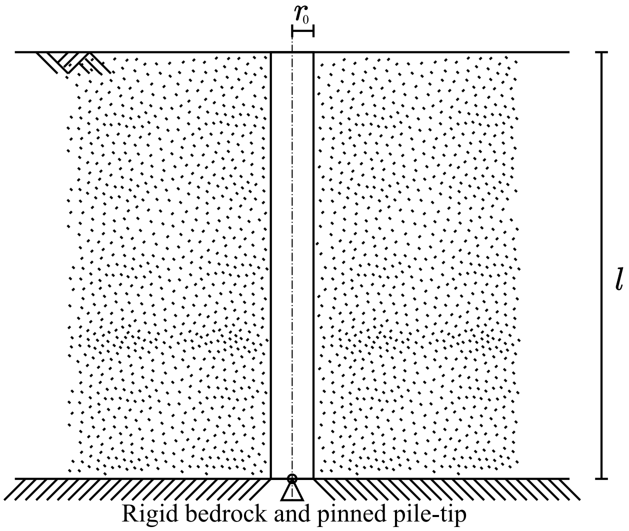

Figure 4.16: Pile configuration for Validation Problem 2 and 3

4.2.5.3 Validation Problem 3

The analysis is performed on a short pile or caisson ($l/r_0 = 4.0$) with the pile-soil configuration described in Figure 4.16 and the results are presented in Figure 4.17 (b).

Referring to Figure 4.17 (a) and (b), the calculated dimensionless pile-head stiffness from the 2D-2DOF model and the 2D-3DOF model are almost identical for the slender pile, $l/r_0 = 10.0$, while a slight difference between the dimensionless stiffness from two models is visible when the pile is less slender, corresponding to $l/r_0 = 4.0$. However, the difference in the dimensionless stiffness magnitude is approximately 5 % of the value calculated from the 2D-3DOF model. Such a small discrepancy appears acceptable in view of the associated lower computational cost of the 2D-2DOF ring element. The conclusion can be made that the rotational coupling does not affect the pile

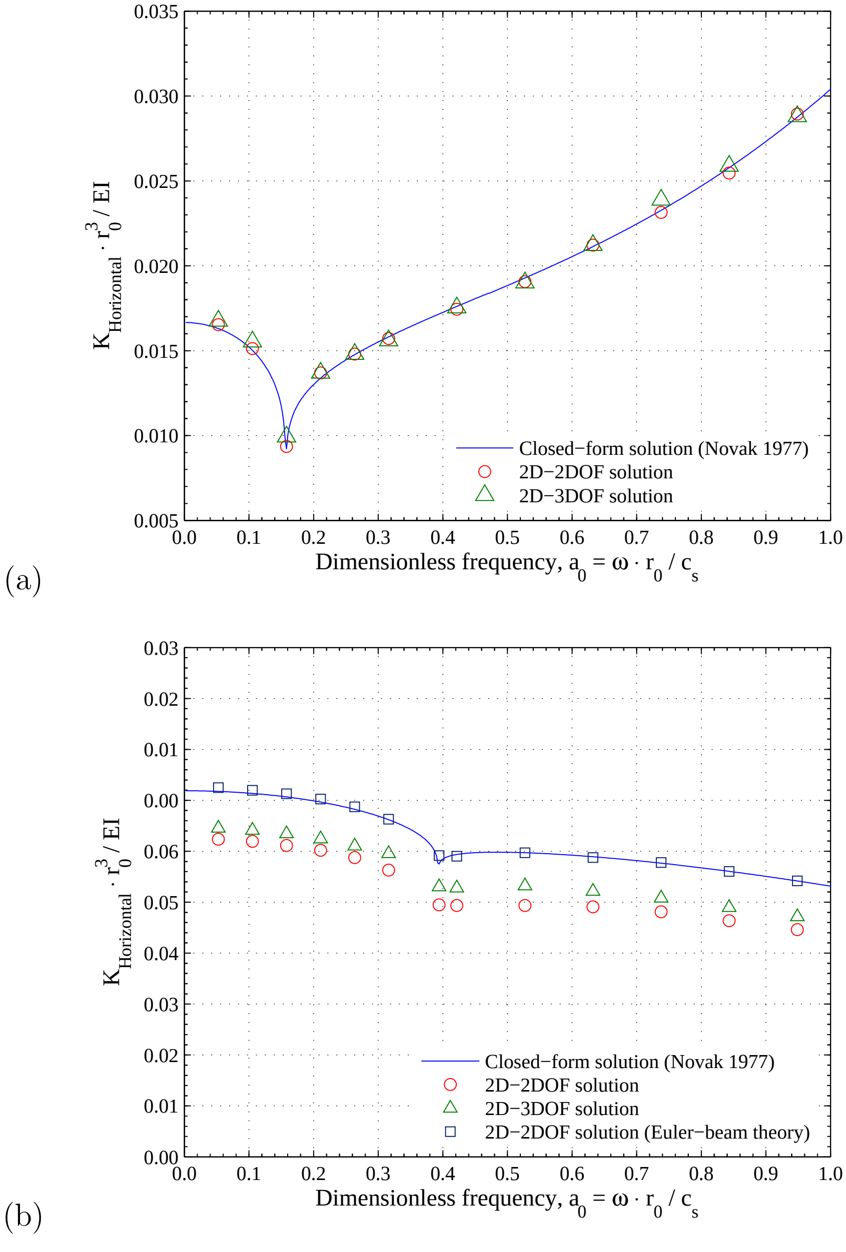

Figure 4.17: Dimensionless pile-head stiffness magnitude versus dimensionless frequency: (a) $l/r_0 = 10.0$ (b) $l/r_0 = 4.0$.

system significantly in any case.

The Novak closed-form solution (1977) is also included in the plot, denoted by the solid line, for the justification with the solution based on the 2D-2DOF ring element. It is observed from Figure 4.17 (b) that the dimensionless stiffness calculated from Novak (1977) differs from the finite-element solution. The investigation was conducted by applying the Euler-beam theory to the 2D-2DOF ring pile-soil model and the calculated dimensionless stiffness, represented by the hollow square boxes, agrees with Novak (1977) perfectly. It is reasonable to conclude that the Novak closed-form solution overestimates the dimensionless stiffness since Euler-beam theory takes into account only bending, not shear deformation.

4.2.5.4 Validation Problem 4

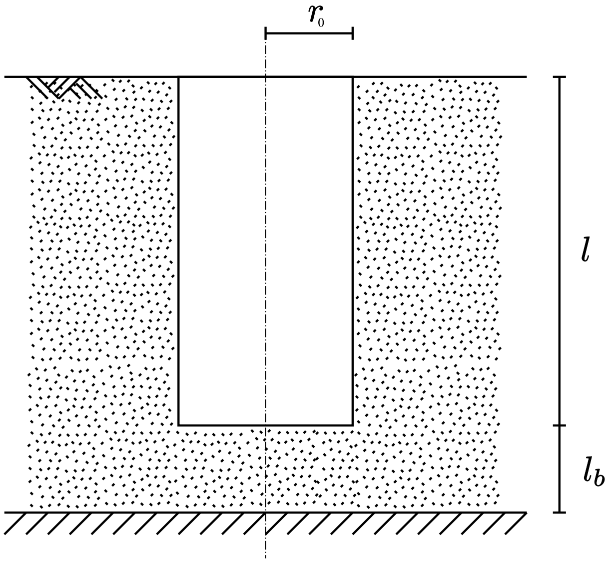

Figure 4.18: Caisson configuration for Validation Problem 4 and 5

Next, the dynamic finite-element analysis of caisson with underlying soil layer is carried out by linear pile element in Subsection 4.1.4 with 2D-2DOF and 2D-3DOF soil element. By such model configuration in Figure 4.18, the investigation of the effect of end-bearing rotational stiffness is possible. The caisson slenderness ratio, l/r_0, and the ratio of the thickness of soil layer under caisson bottom to pile radius, l_b/r_0, are 4.0 and 1.0, respectively. Slight modification is made to the pile model used previously by specifying the soil material properties to beam elements under the bottom of the caisson. The plot of pile-head dimensionless stiffness versus dimensionless excitation frequency is given in Figure 4.19.

4.2.5.5 Validation Problem 5

The caisson-soil configuration shown in Figure 4.18 with the thicker underlying soil layer, $l_b = 2.0$, is analyzed in order to examined the effect due to varying underlying layer thickness to a caisson (short pile) stiffness. Finite-element calculations are carried out with the 2D-2DOF ring and 2D-3DOF ring elements.

According to Figure 4.19, no significant difference can be seen between the two soil ring elements. The FE solutions based on both ring elements also agree very well with the 3-D finite-element solution (Tassoulas 1981). It can be noticed that the solution from the pile model without bottom rotational resistance in Figure 4.17 (b) produced considerably lower dimensionless stiffness than the solution if Figure 4.19. Thus, it can be concluded that the mechanism with a major role in the laterally loaded caisson or short pile is the rotational-bearing resistance.

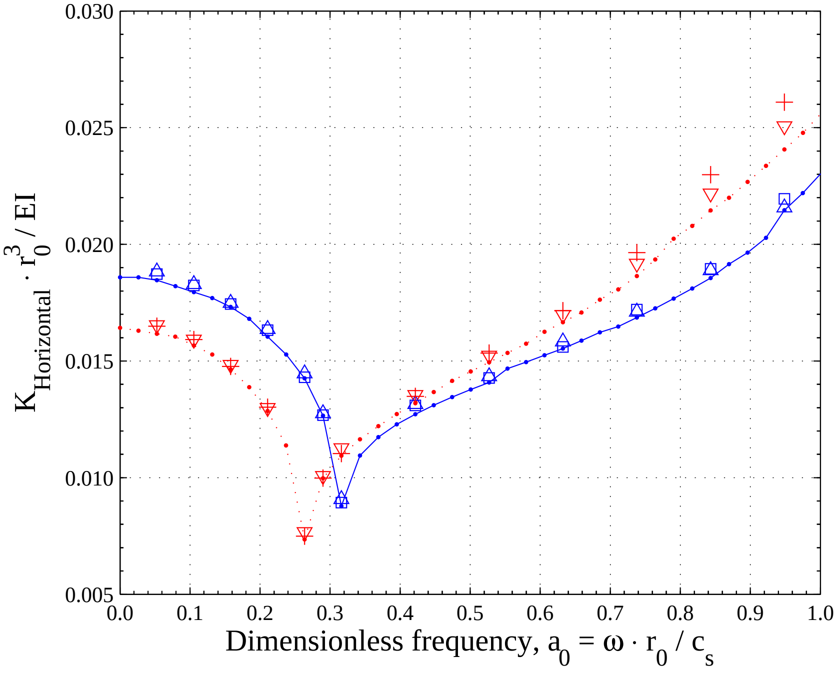

Figure 4.19: Dimensionless pile-head stiffness magnitude versus dimensionless frequency from the pile model with $l/r_0 = 4.0$ and $l_b/r_0 = 1.0$ and 2.0

4.3 Comparison of FE Simulation and Available Experimental Data

This section presents results of finite-element simulation of the field experiment conducted by El-Marsafawi et al. (1992). Referring to the previous section on the comparison between two soil models, the 2D-2DOF soil element is selected for the following investigation due to its computational efficiency.

The analysis is performed on the basis of a model constructed from the information available in El-Marsafawi et al. (1992) as mentioned in Chapter 3. The concrete pile model with the 740 kg cap-mass, M, is harmonically excited by the 120 kg exciter (total pile-cap mass, M, is 860 kg) until steady state response is achieved. The exciting force amplitude can be determined from Equation 3.80. The dimensionless displacement amplitude, $M \cdot u/m_e e$, versus excitation frequency is presented in Figure 4.20 where the solid-line with triangular markers and the dashed-line with hollow circular markers denote experimental data and finite-element solution, respectively.

The solution from the pile model with the 2D-2DOF ring elements

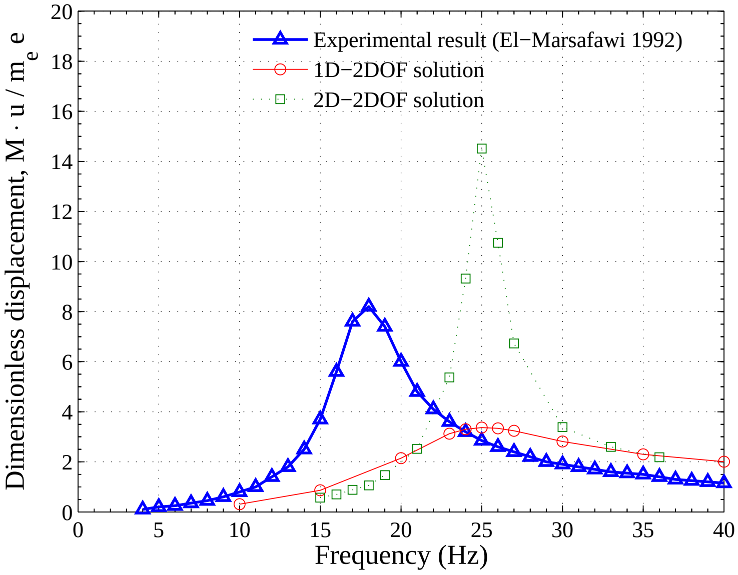

Figure 4.20: Dimensionless displacement amplitude versus excitation frequency.

overestimates the natural frequency and the peak of displacement amplitude indicating an overestimated soil real stiffness or underestimated soil imaginary stiffness. To reduce both peak displacement amplitude and pile-soil characteristic frequency, the actual system must be softer than the documented test description and more damping is required in the finite-element model to match the experimental result.

Hence, there are three possible scenaria: material inelasticity, weak soil at the top surface, and discrepancy in soil modulus measurement, as discussed below;

4.3.1 Effects from Soil Inelasticity

Soil inelasticity reduces the stiffness and provides material damping to the pile-soil system. However, at the same time, the surrounding soil will not be able to transmit as much energy as in the case of purely-elastic soil behavior. Thus, the total energy dissipation will not increase significantly. Moreover, it can be observed from the experimental displacement response that, at the lowest excitation force, there was no sign of inelastic effect.

First, the test was performed at the lowest harmonic force (corresponding to an excitation intensity, $m_e \cdot e$, of 96 kg.mm). Then, elevating $m_e \cdot e$ up to 171 kg.mm., the pile reproduced the same response as that for $m_e \cdot e$ equal to 96 kg.mm in the frequency range lower than the characteristic frequency. For the higher value of $m_e \cdot e$ (259 kg.mm.), the response curve shifted to the left (lower frequency) of two curves, corresponding to lower excitation force indicating that the pile-soil system became softer due to soil inelasticity. In conclusion, there is evidence that the result from the lowest excitation intensity is associated with the elastic system. Therefore, it was selected in the comparison with the developed finite-element models.

4.3.2 Effects from Weak Near-Surface Soil

Now, the focus will be directed to the weak top soil. Since the soil shear-wave velocities were measured at discrete locations providing a piecewise linear shear-wave velocity profile as shown in Figure 3.23, the information over the top-0.5-meter soil, loose and unconfined, may not be accurately represented by the uniform shear-wave velocity with the value obtained from the depth of 0.5 meter. Therefore, a series of laterally-loaded pile calculations were conducted on the basis of pile models with different top-0.5-meter variations of soil shear moduli. The transition of soil moduli is described by constant, linear, and parabolic variations corresponding to the transition exponents of 0, 1, and 2, respectively, as follows:

$$\begin{aligned} \text{constant} &: \quad E(z) = E_{0.5\text{ m.}} \cdot \left(\frac{z}{0.50}\right)^0 \\ \text{Linear} &: \quad E(z) = E_{0.5\text{ m.}} \cdot \left(\frac{z}{0.50}\right)^1 \\ \text{Parabolic} &: \quad E(z) = E_{0.5\text{ m.}} \cdot \left(\frac{z}{0.50}\right)^2 \end{aligned} \tag{4.97}$$

Referring to Figure 4.22, the displacement responses from the model corresponding to the transition exponents 0.0, 1.0, and 2.0 are identified by solid circles, hollow circles, and hollow boxes, respectively. It can be observed from the plot that as the transition exponent increases (weaker top soil), the

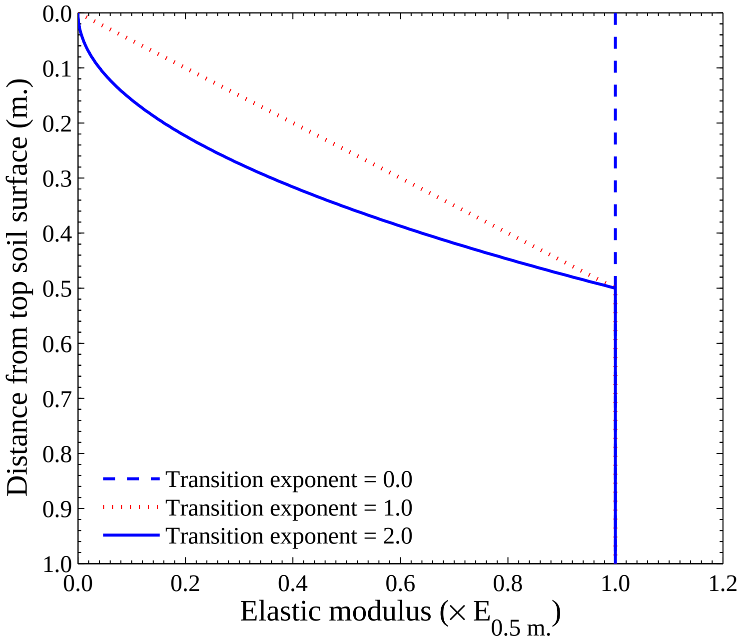

Figure 4.21: The soil elastic modulus distributions described by transition exponents equal to 0.0, 1.0, and 2.0

pile-soil system resonant frequency decreases noticeably while no significant change in the peak dimensionless displacement is observed.

The decrease in the characteristic frequency was caused by the softer top soil layer due to the introduction of soil modulus transition. However, the peak amplitude did not increase significantly since the radiation damping also increased due to the lower top layer's cut-off frequency.

4.3.3 Effects from Inaccuracy of Soil Stiffness Measurement

Now, the effects from the error in shear-wave velocity measurement are shown in Figure 4.23. The uncertainty is represented by a factor applied to the

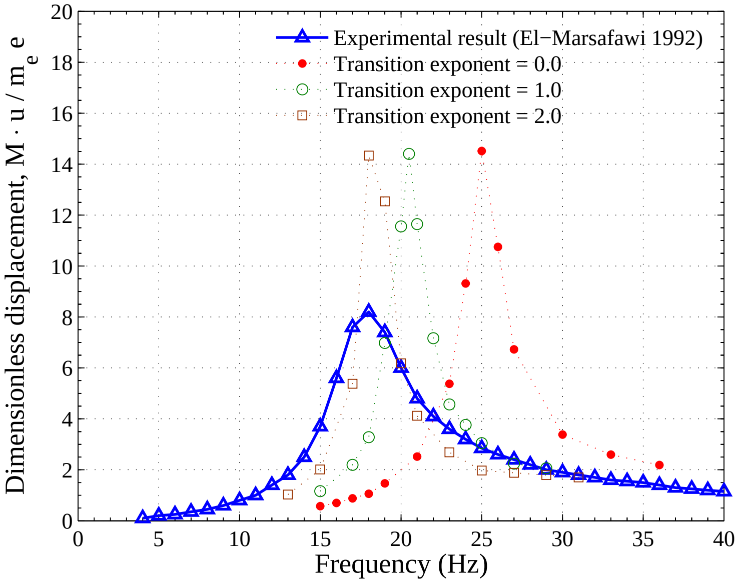

Figure 4.22: Dimensionless displacement amplitude versus excitation frequency from transition exponents equal to 0.0, 1.0, and 2.0.

soil moduli. As the modulus is reduced, decreases in both resonant frequency and peak dimensionless displacement amplitude can be clearly seen.

The inaccuracy of soil modulus measurement affects the behavior of laterally-loaded piles in two ways, reduction of the characteristic frequency and the peak displacement amplitude. As the soil moduli decrease, it can be expected that the stiffness of the pile-soil system will be reduced resulting in pile resonance at lower frequency. In the meantime, the displacement amplitude is expected to be larger due to the lower soil resistance.

However, radiation damping also affects lateral pile response. Considering a homogeneous soil layer, the cut-off frequency can be calculated a $c_s/4H$, where c_s is the layer's shear wave velocity: H is the thickness of the

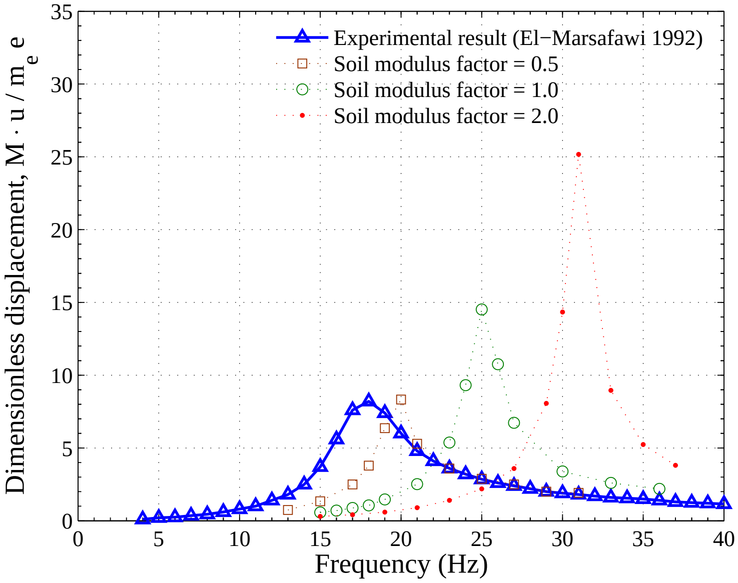

Figure 4.23: Dimensionless displacement amplitude versus excitation frequency from moduli factors equal to 0.5, 1.0, and 2.0.

layer. Because c_s varies with the square root of the soil modulus, the lower soil modulus leads to lower shear wave velocity and cut-off frequency. As a result, the layer starts transmitting the energy at lower frequencies as soil modulus decreases and, therefore, more radiation damping is expected.

Subsequently, the analysis was performed under a combination of two possible scenaria. The modulus transition exponent is set to 0.5 and the soil modulus factor at 0.45 with the result shown in Figure 4.24. The unmatched portion is found at the high frequency and this can be the result from other nonlinear phenomena.

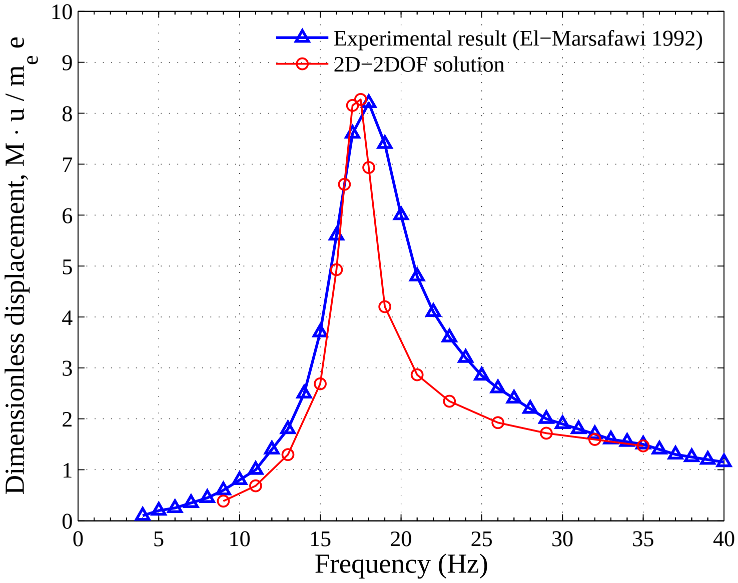

Figure 4.24: Dimensionless displacement amplitude versus excitation frequency from moduli factor and transition exponent equal to 0.45 and 0.5 respectively

4.3.4 Discussion and Future Development

There are other possibilities that may affect the lateral pile response, e.g., softening of the soil with increasing strain, soil material damping, gapping, etc. However, it is not possible to simulate these effects due to insufficient information from the experiment. Better-documented soil information is required in order to construct the more sophisticated model for greater accuracy.

To improve the accuracy of lateral pile response from the reduced-dimension element, appropriate constitutive models for the soil at hand must be used in order to properly describe the loss in stiffness. For the case that a pile is subjected to large displacements, there would be other nonlinear effects involved. Gap opening may occur between the soil and the pile near the surface causing reduction of the pile-head stiffness. Also, slippage at the pile-soil interface, especially for the case of cohesionless soil and steel pile, with a weak bond at the interface, will reduce the lateral pile stiffness and produce additional damping. Finally, to extend the capability of the pile model in general engineering applications, the analysis of pile groups should be considered in future development of the models presented in this dissertation.

Chapter 5

Summary and Conclusions

Continuum-based, computationally-efficient finite-element models for soil representation in laterally-loaded pile-soil were developed by adopting the elastic-displacement field in the azimuthal direction for both elastic and inelastic material behavior. Three elements were constructed based on different soil-domain idealizations, starting from a formulation in one-dimension with independent soil slices that was refined into formulations in two dimensions with increasing detail.

Since the 1D-2DOF, 2D-2DOF, and 2D-3DOF elements represent the actual continua, the energy from the vibrating disk (for 1D-2DOF) or pile (for 2D-2DOF and 2D-3DOF), is carried away realistically. These models are frequency independent and the solutions for transient analysis are more accurate than the solutions by spring and dashpot models. The transient response comparisons between 1D-2DOF and 2-D plane-strain solutions were exhibited and the agreement between two solutions can be clearly observed.

For inelastic soil behavior, since the displacement in reduced-dimension models is assumed to vary elastically, a relatively small discrepancy was observed (slight underestimation of the stiffness). Nevertheless, in the reduced-dimension models presented in this dissertation, the two mechanisms of energy dissipation, material and radiation damping, interact naturally with each other. This constitutes an improvement over spring-and-dashpot Winkler models that require adjustment of the amount of system damping and problem-dependent fine-tuning of the parameters involved.

First, the computationally inexpensive 1D-2DOF model, based on soil-slice idealization, was explored and it was found that the lack of interaction between soil-slices leads to unrealistically low lateral pile stiffness at low frequencies. Hence, the shear interactions between soil slices were taken into account systematically by means of a 2D-2DOF ring element at a higher computational cost than that of the 1D-2DOF soil model. The lateral pile behavior becomes more realistic but, still, the validation of the assumption that the vertical displacement is negligible in lateral pile analysis is mandatory. As a result, the 2D-3DOF ring element is constructed for response comparison.

5.1 Soil Displacement and Stress Approximations

In nonlinear analysis, the stress distributions was assumed to be identical to the one in linear analysis. The same approximation was applied to displacements. The simplifications permit the development of the reduced-dimension model presented in this dissertation.

To validate the simplifications, harmonic disk vibrations in a soil slice were analyzed under plane-strain conditions and compared, assuming elastic soil behavior, with a closed-form solution (Novak 1978). Excellent agreement was found over a range of frequencies in both force amplitude response and the time lag between force and displacement.

The behavior of the 1D-2DOF model was also examined in the case of transient analysis. A Ricker wavelet pulse was applied to the 1D-2DOF disk model and excellent agreement with the results from 2-D plane-strain model was observed. Evidently, the 1D-2DOF disk model works perfectly for purely-elastic soil behavior.

Finally, the 1D-2DOF FE was evaluated in the presence of inelasticity considering both harmonic excitation and a Ricker wavelet pulse. The results show only a small discrepancy in comparison with the 2-D FE model with the maximum error observed is less than 15 % of the actual response.

5.2 Laterally-Loaded Pile Model with Soil-Slice Idealization

The soil domain surrounding a laterally-loaded pile was modeled by a series of plane-strain soil-slices in the vertical direction. The finite-element model was validated with the exact solution of a Winkler beam on elastic spring and dashpot foundation. The foundation complex stiffness was determined by the closed-form solution of Novak (1978). It should be kept in mind that the beam on elastic spring and dashpot foundation does not represent the actual laterally-loaded pile. This solution will be used for validation purposes.

The plane-strain soil domain idealization is not computationally demanding, yet, the simplification, zero shear interaction between slices, leads to lack of lateral pile stiffness at low frequencies. As a consequence, the pile real stiffness is underestimated resulting in overestimation of overall system damping. Thus, the peak displacement amplitude from finite-element simulation using a soil-slice model is smaller than in the actual system. Furthermore, the resonant frequency of the system will be overestimated.

Treatments of the lack of soil stiffness at low frequencies were explored but realistic solutions were not identified, especially when considering inelastic soil behavior.

5.3 2D-2DOF Ring and 2D-3DOF Finite Element

To improve the behavior of the soil-slice model at low frequencies, the shear stress components between slices are introduced to the soil model. Thus, the derivative of the displacement along the length of the pile is included in the computation resulting in the coupled effect over the soil displacement at the adjacent slices. Consequently, the bandwidth of the matrix system of equation becomes wider. This will result in a small increase computational effort. However, the number of degree-of-freedom in the system of equations remains the same as the pile model with soil-slice idealization.

In the 2D-2DOF model for the laterally-loaded pile, the soil vertical displacement was neglected, and, therefore, the stiffness of the pile-soil system was affected by two separate mechanisms. First, the 2D-2DOF ring element can be stiffer than the 2D-3DOF ring because of the constraint on the vertical displacement. However, there is no perceptible difference in the stiffness obtained from two models. Even in the high frequency range beyond the cut-off frequency for longitudinal-waves which is affected by the vertical-displacement constraint, the responses from the two model are practically identical.

Next, the effect of pile rotation and soil vertical-displacement coupling was considered and the 2D-2DOF model and 2D-3DOF models produced identical results for slender piles. A difference in pile-head stiffness can be observed in pile analysis with low slenderness ratio indicating the contribution from rotational stiffness. However, from the results in the case of $l/r = 4.0$ (a short stubby pile), the 2D-2DOF ring element produced approximately 5% underestimation of the pile-head stiffness. From a practical point of view, such small inaccuracy can be accepted in return for significant decrease in computational effort.

The pile models with 2D-2DOF and 2D-3DOF ring elements were analyzed in the case of very short pile or caisson with the inclusion of bottom rotational bearing resistance. The solution comparison leads to the conclusion that the rotational stiffness affects the system pile-head stiffness significantly. Another contribution to pile-head stiffness, is due to the rotational resistance along the pile, leading to a small difference in short pile dimensionless stiffness.

5.4 Simulation of Actual Lateral Pile Vibration

The simulation of an available well-documented experimental result was performed by 2D-2DOF element. The dimensionless displacement response with frequency, simulated from the test description as available, overestimated the experimental result in terms of system characteristic frequency and peak displacement amplitude. There can be many factors, causing such discrepancies, as will be discussed in the following.

5.4.1 Effect of Soil Parameter Measurements

Regarding soil investigation, there are two possibilities affecting significantly the lateral pile response. First, considering the pile deflected shapes (Figures 3.20 and 3.21), it can be clearly seen that the top portion of the pile undergoes considerably large displacement compared to the deeper portion since the soil resisting force is concentrated over the top soil. As far as the soil confining pressure in the vicinity around the top surface is insignificant, the soil elastic moduli should be small. Then, the pile-soil system is less stiff leading to a decrease of the characteristic frequency. However, this weak top soil layer does not affect significantly to the peak displacement amplitude because such a layer will start radiating energy at lower frequencies causing more damping in the pile-soil system.

Error in soil modulus measurement affects significantly the simulated pile response because the cut-off frequency of a soil layer is determined by soil stiffness. The underestimated soil stiffness results in reducing the characteristic frequency and peak displacement amplitude and vice versa for overestimated soil stiffness.

5.4.2 Material Model

Another source of discrepancy can be the material model in the analysis since it may not represent actual soil behavior accurately. The bilinear stress-strain relationship with Von-Mises isotropic hardening is not capable of accommodating the nonlinear decrease in soil modulus as strain increases. However, there was not adequate information to construct a more rigorous material model from the available experimental data.

Bibliography

[1] Badoni, D. and Makris, N. (1996) Nonlinear response of single piles under lateral inertial and seismic loads. *Soil Dynamics and Earthquake Engineering*, 15:29–43.

[2] Baguelin, F.,Frank, R. and Said, Y.H. (1977) Theoretical study of lateral reaction mechanism of piles. *Geotechnique*, 27(3):405–434.

[3] Banerjee, P.K. and Davies, T.G. (1980) Analysis of some reported case histories of laterally loaded pile groups. In *Proceedings of the International Conference on Numerical Methods in Offshore Piling, London, U.K.*, pages 101–108. I.C.E.

[4] Baranov, V.A. (1967) On the calculation of excited vibrations of an embedded foundation. (in russian). *Voprosy Dynamiki i Prochnocti*, 14:195–209. Polytechnical institute of Riga.

[5] Beredugo, Y. (1971) *Vibration of Embedded Symmetric Footings*. PhD thesis, Faculty of Engineering Science.

[6] Beredugo, Y.O. and Novak, M. (1972) Coupled horizontal and rocking vibration of embedded footings. *Canadian Geotechnical Journal*, 9:477–497.

[7] Butterfield, R. and Banerjee, P.K. (1971) The elastic analysis of compressible piles and pile groups. *Geotechnique*, 21(1):43–60.

[8] Dobry, R., Vicente, E., O'Rourke, M.J. and Roesset, J.M. (1982) Horizontal stiffness and damping of single piles. *Journal of Geotechnical Engineering Division*, 108(GT3):439–459.

[9] Dotson, K.W. and Veletsos, A.S. (1990) Vertical and torsional impedances for radially inhomogeneous viscoelastic soil layers. *Soil Dynamics and Earthquake Engineering*, 9(3):110–119.

[10] Douglas, D.J. and Davis, E.H. (1964) The movement of buried footings due to moment and horizontal load and the movement of anchor plates. *Geotechnique*, 14:115–132.

[11] El-Marsafawi, H., Han, Y.C. and Novak, M. (1992) Dynamic experiments on two pile groups. *ASCE Journal of Geotechnical Engineering*, 118(4):576–592.

[12] El-Naggar, M.H. and Bentley, K.J. (2000) Dynamic analysis of laterally loaded piles and dynamic p-y curves. *Canadian Geotechnical Journal*, 37:1166–1183.

[13] El-Naggar, M.H. and Novak, M. (1995) Nonlinear lateral interaction in pile dynamics. *Soil Dynamics and Earthquake Engineering*, 14:141–157.

[14] Gazetas, G. and Dobry, R. (1984) Horizontal response of piles in layered soils. *ASCE Journal of Geotechnical Engineering*, 110(1):20–40.

[15] Gazetas, G. and Dobry, R. (1984) Simple radiation damping model for piles and footings. *ASCE Journal of Engineering Mechanics*, 1984(6):937–955.

[16] Gazetas, G. and Gerolymos, N. (2007) Inelastic lateral response of rigid caisson foundation. In *Proceedings of the 4th U.S.-Japan Workshop on Soil-Structure-Interaction, Tsukuba, Japan*, pages 310–339.

[17] Guddati, M.N. (2006) Arbitrary wide-angle wave equations for complex media. *Computer Methods in Applied Mechanics and Engineering*, 195:65–93.

[18] Guddati, M.N. and Lim, K.-W. (2006) Continued fraction absorbing boundary conditions for convex polygonal domains. *International Journal of Numerical Methods in Engineering*, 66(6):949–977.

[19] Han, Y. and Novak, M. (1988) Dynamic behavior of single piles under strong harmonic excitation. *Canadian Geotechnical Journal*, 25:523–534.

[20] Hetenyi, M. (1946) *Beams on Elastic Foundation.* University of Michigan Press, Ann. Arbor, Michigan.

[21] Kagawa, T. and Kraft, L.M. (1981) Dynamic characteristics of lateral load-deflection relationships of flexible piles. *Earthquake Engineering and Structural Dynamics*, 9(1):53–68.

[22] Kagawa, T. and Kraft, L.M. (1980) Lateral load-deflection relationship of piles subjected to dynamic loadings. *Soils and Foundations, Japanese Society of Soil Mechanics and Foundation Engineering*, 20(4):19–36.

[23] Kagawa, T. and Kraft, L.M. (1980) Seismic p y responses of flexible piles. *Journal of Geotechnical Engineering*, 106(GT8):899–918.

[24] Kuhlemeyer, R.L. (1979) Static and dynamic laterally loaded floating piles. *ASCE Journal of the Geotechnical Engineering*, 105(GT2):289–304.

[25] Makris, N. and Gazetas, G. (1992) Dynamic pile-soil-pile interaction. part ii: Lateral and seismic response. *Earthquake Engineering and Structural Dynamics*, 21:145–162.

[26] Matlock, H. (1970) Correlations for design of laterally loaded piles in soft clay. In *Proceedings of the Offshore Technology Conference, Houston, Texas, OTC 1204*, pages 577–594.

[27] Matlock, H. and Ripperger, E.A. (1956) Procedures and instrumentation for tests on a laterally loaded pile. In *Proceedings of the 8th Texas Conference on Soil Mechanics and Foundation Engineering*, pages 1–39. Bureau of Engineering Research, University of Texas.

[28] Matlock, H. and Ripperger, E.A. (1958) Measurement of soil pressure on a laterally loaded pile. In *Proceedings of American Society of Testing Materials*, pages 1245–1260.

[29] Mindlin, R.D. (1936) Force at a point in the interior of a semi-infinite solid. *Physics*, 7:195–202.

[30] Mylonakis, G. (2001) Elastodynamic model for large-diameter end-bearing shafts. *Soils and Foundations*, 41(3):31–44.

[31] Nogami, T. and Chen, H.-L. (1987) Prediction of dynamic lateral response of nonlinear single-pile by using winkler soil model. *ASCE Journal of Geotechnical Engineering*, 114:39–52.

[32] Nogami, T. and Novak, M. (1977) Resistance of soil to a horizontally vibrating pile. *International Journal of Earthquake Engineering and Structural Dynamics*, 5:249–261.

[33] Nogami, T. and Novak, M. (1980) Coefficient of soil reaction to pile vibration. *ASCE Journal of Geotechnical Engineering*, 106(GT5):565–570.

[34] Nogami, T., Otani, J., Konagai, K. and Chen, H.-L. (1992) Nonlinear soil-pile interaction model for dynamic lateral motion. *Journal of Geotechnical Engineering*, 118(1).

[35] Novak, M. (1974) Dynamic stiffness and damping of piles. *Canadian Geotechnical Journal*, 11:574–598.

[36] Novak, M. and Grigg, R.F. (1976) Dynamic experiments with small pile foundations. *Canadian Geotechnical Journal*, 13:372–385.

[37] Novak, M. and Nogami, T. (1977) Soil-pile interaction in horizontal vibration. *International Journal of Earthquake Engineering and Structural Dynamics*, 5:263–281.

[38] Novak, M. and Sachs, K. (1973) Torsional and coupled vibrations of embedded footings. *International Journal of Earthquake Engineering and Structural Dynamics*, 2:11–33.

[39] Novak, M. and Sheta, M. (1980) Approximate approach to contact problems of piles. In *Proceedings of Geotechnical Engineering Division*, pages 53–79. ASCE.

[40] Novak, M. and Sheta, M. (1982) Dynamic response of piles and pile groups. In *2nd International Conference on Numerical Method in Offshore Piling, Austin, TX*. I.C.E.

[41] Novak, M., Nogami, T. and Aboul-Ella, F. (1978) Dynamic soil reactions for plane strain case. *Journal of the Engineering Mechanics Division*, 104(EM4):953–959.

[42] Poulos, H.G. (1971) Behavior of laterally loaded piles : I-single piles. *Journal of the Soil Mechanics and Foundations Division*, 97(SM5):711–731.

[43] Poulos, H.G. (1971) Behavior of laterally loaded piles: II-pile groups. *Journal of Soil Mechanics and Foundation Division*, SM5(97):733–751.

[44] Poulos, H.G. (1972) Behavior of laterally loaded piles: III-socketed piles. *Journal of the Soil Mechanics and Foundations Division*, 98(SM4):341–360.

[45] Poulos, H.G. (1979) Group factor for pile-deflection estimation. *ASCE Journal of the Geotechnical Engineering*, 105(GT12):1489–1509.

[46] Poulos, H.G. (1980) An Approach for the Analysis of Offshore Pile Groups. In *Proceedings of the International Conference on Numerical Methods in Offshore Piling*, I.C.E.

[47] Reese, L.C., Cox, W.R., and Koop, F.D. (1974) Analysis of laterally loaded piles in sand. In *Proceedings of the 6th Offshore Technology Conference, Houston, Texas, OTC 2080*, pages 473–483.

[48] Tassoulas, J.L. (1981) Elements for the Numerical Analysis of Wave Motion in Layered Strata, *Research Report R81-2*, Massachusetts Institute of Technology, Cambridge, Massachusetts.

[49] Trochanis, A.M., Bielak, J. and Christiano, P. (1991) Simplified model for analysis of one or two piles. *ASCE Journal of Geotechnical Engineering*, 117(3):448–466.

[50] Wolf, J.P., Meek, J.W. and Song, C. (1992) Cone models for a pile foundation. In *Piles under Dynamic Loads, Geotechnical Special Publication, 34*, pages 94–113. ASCE.

Vita

Punchet Thammarak was born in Bangkok, Thailand on May 9, 1982. He is the first son of Pratueng and Salinee Thammarak. In May 2004, he graduated bachelor degree in engineering from Chulalongkorn University, Thailand. He worked as an engineering analyst for a consultant company for a half year. In 2005, he enrolled the doctoral program at the department of civil, architectural, and environmental engineering at the University of Texas at Austin.

Permanent address: 99/2 M.1, Bang-Ku-Weang, Bang-Kruy
Nonthaburi, Thailand 11130

This dissertation was typeset with LaTeX[†] by the author.

[†] LaTeX is a document preparation system developed by Leslie Lamport as a special version of Donald Knuth's TeX Program.